LUND UNIVERSITY

High-spin states in ^{60}Cu and implications for states in the mirror nucleus ^{60}Ga

Rudolph, D.; Ragnarsson, I.; Chiara, C. J.; Reviol, W.; Andreoiu, C.; Carpenter, M. P.; Charity, R. J.; Ekman, J.; Fahlander, C.; du Rietz, R.; Seweryniak, D.; Sobotka, L. G.

Published in:
Physical Review C

DOI:
10.1103/mfz2-qldg

2026

Document Version:
Publisher's PDF, also known as Version of record

High-spin states in ^{60}Cu and implications for states in the mirror nucleus ^{60}Ga

D. Rudolph [1,*] I. Ragnarsson [1] C. J. Chiara [2,†] W. Reviol [2,3] C. Andreoiu [1,4] M. P. Carpenter,[3] R. J. Charity [2]
J. Ekman [1,5] C. Fahlander [1] R. du Rietz [1,5] D. Seweryniak [3] and L. G. Sobotka [2]
[1]*Department of Physics, Lund University, 22100 Lund, Sweden*
[2]*Chemistry Department, Washington University, St. Louis, Missouri 63130, USA*
[3]*Physics Division, Argonne National Laboratory, Lemont, Illinois 60439, USA*
[4]*Chemistry Department, Simon Fraser University, Burnaby, British Columbia, V5A 1S6, Canada*
[5]*Department of Materials Science and Applied Mathematics, Malmö University, SE-20506 Malmö, Sweden*

(Received 27 March 2026; accepted 8 July 2026; published 3 August 2026)

High-spin states in ^{60}Cu are investigated on the basis of reaction-channel-selected γ-ray spectroscopy. Data stem from three experiments that used the same fusion-evaporation reaction at similar beam energies. The Gammasphere γ-ray spectrometer was combined with the Microball CsI(Tl) detector array and sets of liquid-scintillator neutron detectors which allowed us to identify and tag on evaporated light charged particles and neutrons, respectively. A level scheme is proposed which comprises more than 300 γ-ray transitions connecting more than 100 excited states. Predictions from cranked Nilsson-Strutinsky calculations describe the observed high-spin collective structures in ^{60}Cu. Predictions of shell-model calculations are probed with a suite of low- to medium-spin states of both parities. Taking into account isospin-symmetry-breaking terms in these calculations, a case study of the yrast line of the weakly bound mirror nucleus ^{60}Ga is presented.

DOI: 10.1103/mfz2-qldg

I. INTRODUCTION

High-spin nuclear structure of nuclei near doubly magic ^{56}Ni is governed by particle-hole excitations across the shell gaps at neutron and proton number $N, Z = 28$. Depending on the number of holes in the high-j $f_{7/2}$ orbital below these gaps, and the number of particles in the high-j $g_{9/2}$ orbital above them, collective magnetic-dipole structures, dubbed shears bands, and well- to superdeformed rotational bands arise as a function of excitation energy and angular momentum [1–3]. Because of increased residual interactions between aligned high-j angular momenta of similar proton and neutron states, these collective effects are found to be enhanced at the $N = Z$ line [4–6]. Furthermore, the close proximity of the $N = Z$ line with the proton dripline for proton numbers $Z \geqslant 28$ led to the discovery of discrete-energy proton emission from high-spin rotational states [4,5]. Embarking on this proximity situation, it has been recently shown that well-tuned shell-model calculations are capable of describing mirror energy differences as a function of spin when quasibound states at the proton dripline are involved. This has been exemplified by the data of the isospin $T_z = \pm 1/2$ pair ^{61}Ga - ^{61}Zn [7].

The present study on ^{60}Cu complements previous high-spin nuclear-structure studies of neutron-deficient mass $N \approx Z$ nuclei with $Z \geqslant 28$. Comprehensive decay schemes have been derived for, e.g., $N \approx Z$ nuclei such as ^{56}Ni [8], ^{57}Ni [9], ^{58}Ni [10], ^{59}Ni [11], ^{60}Ni [12], ^{58}Cu [13], ^{59}Cu [3], ^{61}Cu [14], ^{60}Zn [6], ^{61}Zn [15], ^{62}Zn [16,17], ^{62}Ga [18], and ^{63}Ga [19]. Information on ^{60}Cu, however, remains comparatively scarce [20], although a dedicated study was able to delineate the yrast line of the nucleus up to a $I^{\pi} = 13^{+}$ state at 8.1-MeV excitation energy [21]. That study engaged angular-correlation and polarization measurements to unambiguously determine spins and parities of a considerable number of low-lying excited states of ^{60}Cu. It provided an excellent starting point for the present work.

Following a brief synopsis of the experiments in Sec. II, analysis methods are outlined in Sec. III. More than 300 γ-ray transitions are placed in an extended ^{60}Cu level scheme comprising more than 100 excited states. Because of the inherent complexity, the description of the experimental results is split into four parts in Sec. IV, focusing on the irregular low-spin part of the level scheme as well as the various, newly observed collective structures. Accordingly, the interpretation in Sec. V contains two main parts: cranked Nilsson-Strutinsky predictions for comparisons with the collective band structures, as well as shell-model calculations performed within two different model spaces and thus several shell-model interactions. For these, with both proton and neutron number exceeding particle number 28, low-lying states in ^{60}Cu provide a relevant test case for the transition from the pure $\mathcal{N} = 3$ fp space

*Contact author: Dirk.Rudolph@fysik.lu.se
†Present address: U.S. Army Combat Capabilities Development Command Army Research Laboratory, Adelphi, Maryland 20783, USA.

toward the $f_{5/2}pg_{9/2}$ space and the quality and stability of the respective predictions [19]. Given the increasing experimental interest and access to low-lying states in nuclei with $N < Z$ in the region, whether by fusion-evaporation reactions [7] or relativistic radioactive beams (see, e.g., Refs. [22–25]), shell-model predictions for the weakly bound mirror nucleus ^{60}Ga are included in Sec. V. The paper concludes with a brief summary.

II. EXPERIMENTS

This work is based on γ-ray spectroscopy data from three experiments which used ^{36}Ar + ^{28}Si fusion-evaporation reactions and conceptually similar experimental setups. Details of these experiments can be found in, e.g., Refs. [8,10,12–15,26,27]. In brief, beams of ^{36}Ar were provided by either the 88" Cyclotron at Lawrence Berkeley National Laboratory (LBNL) or the ATLAS accelerator at Argonne National Laboratory (ANL). These impinged on targets consisting of thin (0.20–0.42 mg/cm^2) layers of isotopically enriched (>99%) ^{28}Si supported by Ta foils of 1-mg/cm^2 thickness, which faced the beam. The midtarget beam energies were in the range of 130–135 MeV. The residual nucleus of interest, here ^{60}Cu, was obtained by evaporation of three protons and one neutron from the ^{64}Ge compound nucleus. The yield of ^{60}Cu corresponds to about 10%–15% of the total fusion cross section and this is the strongest channel associated with neutron evaporation for the chosen beam energies. Following the particle evaporation process, discrete states in ^{60}Cu were observed up to excitation energies $E_x \lesssim 20$ MeV and angular momenta $I \gtrsim 20\hbar$ (see Sec. IV).

The target was surrounded by the Gammasphere array comprising 77 or 86 modules of HPGe detectors with bismuth-germanate (BGO) Compton suppressors [28]. Fifteen or thirty liquid-scintillator neutron detectors [29,30] filled the respective number of slots in the Gammasphere support frame at the most forward angles with respect to the beam direction. Evaporated light charged particles were detected at the target position with the Microball, a 95-element CsI(Tl) detector [31]. For the two experiments at ANL, certain forward rings of the Microball were replaced by Si strip detectors, to allow for particle-γ spectroscopy in the fashion of Ref. [13]. For the same experiments, the BGO hevimet absorbers were removed, to enable accurate measurements of γ-ray multiplicity and sum energy [32]. Two conditions were required for collecting events in prompt-coincidence mode: Either four or more HPGe detectors or three or more HPGe detectors, and at least one neutron detector had to fire.

Calibration data for Gammasphere were taken with standard ^{56}Co, ^{133}Ba, and ^{152}Eu sources. A useful by-product of each experiment was the population of ^{54m}Fe via evaporation of two alpha particles and two protons; the properties of this isomer are $T_{1/2} = 363(4)$ ns and $I^{\pi} = 10^{+}$ [33]. Acting as isomer catchers, the respective absorber foils of the CsI(Tl) and Si detectors near the target collected significant amounts of ^{54m}Fe activity. The decay of this isomer via a cascade of five $E2$ γ rays was used to monitor potential HPGe signal drifts throughout each experiment and across the energy range of interest ($E_{\gamma} \approx 0.1$–4.0 MeV). Energy calibrations of the charged-particle detectors were based on ^{12}C(p, p') and ^{197}Au(α, α') scattering data.

III. ANALYSIS METHODS

Pulse-shape-discrimination and time-of-flight methods were employed to achieve clean proton-α and neutron-γ separation, respectively. Details of the procedures were described in numerous publications (see, e.g., references at the beginning of the previous section and related student theses [26,27]). Here, the ancillary detection systems for evaporated particles were used to select only those γ rays detected in Gammasphere which were in prompt coincidence with three protons and one neutron, i.e., belonging to the $3p1n$ reaction channel ^{60}Cu. Requiring also correlations between the γ-ray sum energy, γ-ray multiplicity, and sum energy of all evaporated particles further suppresses entries from competing or contaminating reaction channels [32]. Besides γ rays from the $3p1n$ reaction channel of interest, there remained only a marginal number of events from the $4p1n$ channel ^{59}Ni, i.e., when one proton escaped detection. If present in a γ-ray spectrum, contaminations from ^{59}Ni could be easily identified by observing its 339-keV ground-state transition. This transition is coincident with almost all other γ rays associated with medium- to high-spin states in ^{59}Ni [11].

The energies and angles of emission for all evaporated particles, as well as the particle types, were known for each event. This allowed for determination of the recoil vector of residual nuclei on an event-by-event basis and thus enabled an event-by-event Doppler-shift correction for the γ-ray energies [31], which improved the γ-ray energy resolution to about 7.5 keV full width at half maximum (FWHM) for $E_{\gamma} = 1.4$ MeV and recoil velocities of nearly 5% of the speed of light. Some of the γ rays from highly excited states might be emitted while the recoil is still moving across the target. Uncorrected, this "$F(\tau)$ effect" led to a slight increase of FWHM. On one hand, correcting for the slowing-down process inside the target layer improves the FWHM value of these fast decays. On the other hand, this correction worsens the FWHM of the bulk of γ-ray transitions arising from decays occurring after the recoiling nuclei left the target. In fact, analyzing γ-ray spectra with and without the slowing-down correction made possible the association of γ rays with either the low- or high-spin part of the decay scheme. For ^{60}Cu, this method was applied to states with $E_x \gtrsim 10$ MeV (see Secs. IV C and IV D).

The reaction-channel-selected γ-ray events were sorted offline into various projections of γ-ray energy, E_{γ}, E_{γ}-E_{γ} matrices ($\gamma\gamma$), an E_{γ}-E_{γ}-E_{γ} cube ($\gamma\gamma\gamma$), as well as several $\gamma\gamma$ matrices preselected by γ rays found to cleanly define certain parts or structures of the complex level scheme of ^{60}Cu (see Sec. IV). The γ-ray analysis employed the RADWARE software package [34] and the spectrum analysis code Tv [35]. The experimental results are summarized in Table I. The proposed high-spin decay scheme of ^{60}Cu turned out to be very complex with more than 300 γ-ray transitions connecting more than 100 excited states. Therefore, the detailed presentation of the γ-ray analysis and results is the subject of dedicated Secs. IV A–IV D.

TABLE I. The ^{60}Cu energy levels, γ-ray transition energies, relative intensities of the γ rays placed in the level scheme, types of gating transitions used in the directional-correlation analysis, DCO ratios, multipole assignments, multipole mixing ratios (in selected cases), and assigned spins and parities of the initial and final states of the γ rays.

E_x (keV)	E_γ (keV)	$I_{\gamma,\mathrm{rel}}$ (%)	Gate[a]	R_{DCO} 150°-97°	R_{DCO} 150°-127°	R_{DCO} 127°-97°	Mult. Ass't.	$\delta(E2/M1)$	I_i^π ($\hbar$)	I_f^π ($\hbar$)
62.3(1)	62.4(2)	220(10)					$E2/M1$[b]		1_1^{+}[c]	2_1^{+}
287.1(1)	224.9(1)	252(8)	D	0.80(6)	0.92(8)	0.86(6)	$E2/M1$[b]	$+0.16(^{5}_{6})$	2_2^{+}[c]	1_1^{+}
	287.1(2)	84(6)	D	0.94(12)			$\Delta I = 0$[b]		2_2^{+}	2_1^{+}
453.6(1)	166.7(2)	26(2)					$E2/M1$[b]		3_1^{+}[c]	2_2^{+}
	391.2(2)	3(1)					$E2$		3_1^{+}	1_1^{+}
	453.6(1)	1100(32)	D	0.63(3)	0.83(5)	0.78(4)	$E2/M1$[b]	$+0.03(^{4}_{5})$	3_1^{+}	2_1^{+}
557.4(1)	103.9(1)	789(32)					$E2/M1$[b]		4_1^{+}[c]	3_1^{+}
	270.3(1)	223(10)	D	1.00(7)	1.00(8)	0.94(7)	$E2$		4_1^{+}	2_2^{+}
	557.3(1)	1102(35)	D	1.00(6)	1.00(6)	1.02(6)	$E2$[b]		4_1^{+}	2_1^{+}
780.9(1)	223.6(3)	12(3)					$E2/M1$		3_2^{+}[c]	4_1^{+}
	327.3(2)	18(2)	B	0.98(14)			$\Delta I = 0$		3_2^{+}	3_1^{+}
	781.0(2)	51(4)	B	0.38(5)	0.42(7)	0.61(6)	$E2/M1$[b]	$-1.2 < \delta < -0.4$	3_2^{+}	2_1^{+}
1421.0(1)	863.4(3)	29(4)					$\Delta I = 0$		4_2^{+}[d]	4_1^{+}
	967.4(2)	44(4)					$E2/M1$		4_2^{+}	3_1^{+}
	1134.2(3)	51(5)					$E2$		4_2^{+}	2_2^{+}
	1421.0(4)	36(5)					$E2$		4_2^{+}	2_1^{+}
1505.4(2)	724.4(3)	13(2)					$E2/M1$		4_3^{+}	3_2^{+}
	1051.8(4)	38(3)	E	0.37(8)	0.61(12)	0.74(11)	$E2/M1$	$-1.8 < \delta < -0.3$	4_3^{+}	3_1^{+}
	1505.6(4)	53(4)	E	1.11(16)	0.96(14)	1.00(13)	$E2$		4_3^{+}	2_1^{+}
1603.6(1)	822.8(2)	67(4)					$E2$		5_1^{+}[c]	3_2^{+}
	1046.1(2)	804(28)	A	0.34(2)	0.55(3)	0.63(3)	$E2/M1$[b]	$-0.8(^{3}_{5})$	5_1^{+}	4_1^{+}
	1150.1(4)	22(5)					$E2$		5_1^{+}	3_1^{+}
1778.8(1)	357.9(2)	25(3)					$E2/M1$		5_2^{+}[c]	4_2^{+}
	1221.1(3)	81(3)	A	0.75(12)	0.85(16)	0.77(12)	$E2/M1$[b]	$+0.11(^{11}_{13})$	5_2^{+}	4_1^{+}
	1325.4(3)	125(5)	F	1.02(17)	1.00(21)	1.02(28)	$E2$[b]		5_2^{+}	3_1^{+}
1862.9(2)	357.7(3)	11(2)					$(\Delta I = 0)$		(4_4^{+})[e]	4_3^{+}
	1305.4(6)	7(2)					$(\Delta I = 0)$		(4_4^{+})	4_1^{+}
	1409.4(5)	18(3)					$(E2/M1)$		(4_4^{+})	3_1^{+}
2026.6(1)	247.6(3)	6(1)					$\Delta I = 0$		5_3^{+}[c]	5_2^{+}
	423.0(4)	2(1)					$\Delta I = 0$		5_3^{+}	5_1^{+}
	605.4(4)	23(2)					$E2/M1$		5_3^{+}	4_2^{+}
	1469.3(3)	205(8)	A	0.51(7)	0.70(13)	0.74(9)	$E2/M1$[b]	$-0.14(^{10}_{17})$	5_3^{+}	4_1^{+}
	1572.9(4)	22(3)					$E2$[b]		5_3^{+}	3_1^{+}
2197.0(1)	593.6(3)	29(3)					$E2/M1$		6_1^{+}[c]	5_1^{+}
	1639.7(3)	916(46)	A	1.03(6)	0.96(6)	1.03(5)	$E2$[b]		6_1^{+}	4_1^{+}
2287.6(2)	866.2(6)	9(3)					$E2/M1$		5_4^{+}	4_2^{+}
	1730.6(5)	49(4)	A	0.80(26)	0.84(16)	0.67(13)	$E2/M1$	$\approx +0.1$	5_4^{+}	4_1^{+}
2351.0(2)	488.2(3)	26(3)					$(E2/M1)$		5_5^{+}	(4_4^{+})
	1793.8(4)	77(4)	A	0.33(8)	0.70(14)	0.69(11)	$E2/M1$	$-2.4 < \delta < -0.2$	5_5^{+}	4_1^{+}
2691.7(2)	665.1(6)	6(2)					$E2/M1$		6_2^{+}[c]	5_3^{+}
	1088.1(2)	148(4)	A,G	0.23(3)	0.44(7)	0.51(4)	$E2/M1$[b]	$-0.9(2)$	6_2^{+}	5_1^{+}
	1186.2(3)	98(4)	G	1.26(16)	0.96(12)	0.99(13)	$E2$		6_2^{+}	4_3^{+}
	1270.6(3)	55(3)	G	1.07(19)	1.04(19)	0.95(16)	$E2$		6_2^{+}	4_2^{+}
2817.0(1)	466.0(3)	8(2)					$E2/M1$		6_3^{+}[c]	5_5^{+}
	529.2(4)	4(2)					$E2/M1$		6_3^{+}	5_4^{+}
	619.8(3)	10(2)					$\Delta I = 0$		6_3^{+}	6_1^{+}
	790.3(2)	147(7)	A,H	0.77(7)	0.95(10)	0.89(7)	$E2/M1$[b]	$+0.14(^{6}_{7})$	6_3^{+}	5_3^{+}
			b	0.84(9)	0.90(11)	0.88(9)				
	1038.4(3)	34(3)	C	$\gg 1$			$E2/M1$		6_3^{+}	5_2^{+}
	1213.4(3)	21(3)					$E2/M1$		6_3^{+}	5_1^{+}
	1396.2(4)	22(3)					$E2$		6_3^{+}	4_2^{+}

TABLE I. (*Continued.*)

E_x (keV)	E_γ (keV)	$I_{\gamma,\mathrm{rel}}$ (%)	Gate[a]	R_DCO 150°-97°	R_DCO 150°-127°	R_DCO 127°-97°	Mult. Ass't.	$\delta(E2/M1)$	I_i^π ($\hbar$)	I_f^π ($\hbar$)
2939.1(2)	588.0(4)	6(2)					$(E2/M1)$		(6_4^+)[e]	5_5^+
	1160.4(5)[f]	16(5)					$(E2/M1)$		(6_4^+)	5_2^+
	1335.3(3)	11(2)					$(E2/M1)$		(6_4^+)	5_1^+
	1517.9(5)	26(4)					$(E2)$		(6_4^+)	4_2^+
	2381.8(7)	13(3)					$(E2)$		(6_4^+)	4_1^+
3064.8(2)	777.4(5)	6(2)					$\Delta I=0$		5_1^-[d]	5_4^+
	867.8(3)	10(2)					$E1$		5_1^-	6_1^+
	2506.6(6)	41(3)	A	0.62(22)	0.66(21)	0.57(14)	$E1$	$0.0(^2_4)$	5_1^-	4_1^+
3155.7(2)	868.3(4)	35(4)					$E1$		6_1^-[c]	5_4^+
	1128.7(4)	40(3)					$E1$		6_1^-	5_3^+
	1377.2(4)	34(3)					$E1$		6_1^-	5_2^+
	1552.0(3)	408(19)	J	0.57(5)	0.74(6)	0.71(5)	$E1$[b]	$-0.04(^6_8)$	6_1^-	5_1^+
3190.9(2)	499.1(3)	20(3)					$E2/M1$		7_1^+[c]	6_2^+
	993.8(3)	53(4)	D	0.33(7)	0.38(19)	0.59(8)	$E2/M1$	$-0.9(^4_6)$	7_1^+	6_1^+
	1412.4(5)	63(4)	C	1.11(17)	1.10(16)	0.98(12)	$E2$		7_1^+	5_2^+
	1587.2(3)	272(7)	B	1.08(28)	1.00(23)	0.90(19)	$E2$[b]		7_1^+	5_1^+
3210.6(3)	859.9(4)	32(3)					$(E2/M1)$		(6_5^+)[e]	5_5^+
3318.3(2)	253.4(2)	13(1)	A	0.50(24)			$E2/M1$		6_2^-[d]	5_1^-
	1121.3(3)	34(3)					$\Delta I=0$		6_2^-	6_1^+
3354.3(2)	1157.3(2)	674(27)	D,L	0.52(3)	0.70(4)	0.73(4)	$M2/E1$[b]	$-0.11(^5_7)$	7_1^-[c]	6_1^+
3371.8(2)	1174.6(4)	28(3)					$E2/M1$		7_2^+[d]	6_1^+
	1593.4(4)	58(4)	C	1.06(13)	1.10(13)	1.27(13)	$E2$		7_2^+	5_2^+
	1768.1(4)	33(3)					$E2$		7_2^+	5_1^+
3745.0(2)	805.7(4)	14(2)					$(E2/M1)$		7_3^+	(6_4^+)
	927.9(2)	103(5)	a	1.21(12)	0.97(10)	1.01(10)	$E2/M1$	$+0.22(^7_8)$	7_3^+	6_3^+
	1394.5(6)	11(2)					$E2$		7_3^+	5_5^+
	1548.0(5)	37(4)	D	0.42(13)	0.78(18)	0.63(13)	$E2/M1$	$-0.40<\delta<-0.03$	7_3^+	6_1^+
	1718.4(6)	33(3)					$E2$		7_3^+	5_3^+
3771.9(2)	417.4(2)	109(4)	K	1.17(9)	1.12(9)	1.01(8)	$\Delta I=0$	$\lvert\delta\rvert>1$	7_2^-[c]	7_1^-
	616.4(2)	108(4)	K	0.51(5)	0.75(7)	0.70(6)	$E2/M1$	$-0.09(^7_9)$	7_2^-	6_1^-
	1080.0(4)	33(3)	E,K	0.48(11)	0.61(12)	0.61(11)	$M2/E1$	$-0.16(^8_9)$	7_2^-	6_2^+
	1574.9(4)	11(3)					$E1$		7_2^-	6_1^+
3846.6(2)	636.1(5)	6(2)					$(E2/M1)$		7_4^+[d]	(6_5^+)
	1495.9(5)	26(3)					$E2$		7_4^+	5_5^+
	1650.0(6)	40(6)					$E2/M1$		7_4^+	6_1^+
	1820.1(6)	8(3)					$E2$		7_4^+	5_3^+
4004.0(2)[g]	847.9(4)	9(2)					$\Delta I=0$		6_3^-[d]	6_1^-
	939.4(4)	4(1)					$E2/M1$		6_3^-	5_1^-
	1064.6(4)	9(2)					$(\Delta I=0)$		6_3^-	(6_4^+)
	1186.5(4)	7(2)					$\Delta I=0$		6_3^-	6_3^+
	1653.4(5)	7(2)					$E1$		6_3^-	5_5^+
	1977.2(4)	21(2)					$E1$		6_3^-	5_3^+
	2224.8(8)	5(2)					$E1$		6_3^-	5_1^+
4074.2(2)	703.2(3)	25(3)	F	0.43(11)	0.77(19)	0.79(15)	$E2/M1$	≈ -0.3	8_1^+	7_2^+
	1382.3(3)	141(6)	E	0.97(13)	1.06(13)	1.24(15)	$E2$		8_1^+	6_2^+
4290.2(2)[h]	215.7(4)	4(1)					$E1$		7_3^-	8_1^+
	286.3(2)	64(5)	d	1.01(8)	1.11(10)	1.06(8)	$E2/M1$	$+0.27(^7_6)$	7_3^-	6_3^-
	518.0(4)	11(3)					$\Delta I=0$		7_3^-	7_2^-
	544.7(5)	4(1)					$\Delta I=0$		7_3^-	7_3^+
	936.2(5)	8(2)					$\Delta I=0$		7_3^-	7_1^-
	971.8(5)	13(2)	e,g,h	0.91(44)			$E2/M1$		7_3^-	6_2^-
	1079.4(6)	4(1)					$(E1)$		7_3^-	(6_5^+)
	1134.3(3)	86(4)	d	1.16(11)	0.94(10)	0.96(8)	$E2/M1$	$+0.26(10)$	7_3^-	6_1^-
	1225.1(4)	19(3)					$E2$		7_3^-	5_1^-
	1350.9(4)	12(2)					$(E1)$		7_3^-	(6_4^+)

TABLE I. (*Continued.*)

E_x (keV)	E_γ (keV)	$I_{\gamma,\mathrm{rel}}$ (%)	Gate[a]	R_{DCO} 150°-97°	R_{DCO} 150°-127°	R_{DCO} 127°-97°	Mult. Ass't.	$\delta(E2/M1)$	I_i^π ($\hbar$)	I_f^π ($\hbar$)
	1473.7(5)	28(3)	[i]				$E1$		7_3^-	6_3^+
	1598.4(5)	33(3)	e,g,h	0.78(14)	0.87(12)	0.96(13)	$E1$	$0.08(^{9}_{11})$	7_3^-	6_2^+
	2093.4(6)	7(2)					$E1$		7_3^-	6_1^+
4417.8(2)[j]	413.6(3)	12(2)	e,g,h	0.88(17)	1.00(21)	0.95(18)	$E2/M1$	$0.13(^{12}_{13})$	7_4^-	6_3^-
	1099.6(5)	12(2)					$E2/M1$		7_4^-	6_2^-
	1352.7(6)	6(2)					$E2$		7_4^-	5_1^-
4520.8(2)	748.8(2)	27(3)	M	0.93(17)	1.23(24)	1.15(16)	$E2/M1$	+0.3(2)	8_1^-[c]	7_2^-
	1166.6(3)	114(5)	D,M	0.48(5)	0.62(6)	0.68(6)	$E2/M1$[b]	$-0.17(^{7}_{11})$	8_1^-	7_1^-
	1330.0(3)	78(6)	F,M	0.64(6)	0.66(7)	0.71(7)	$E1$[b]	−0.01(10)	8_1^-	7_1^+
	1365.1(3)	176(6)	M	1.04(8)	0.99(7)	1.14(8)	$E2$[b]		8_1^-	6_1^-
4580.3(2)	506.3(4)	10(2)	G	0.76(20)			$\Delta I = 0$		8_2^+	8_1^+
	835.4(3)	52(3)	[i]				$E2/M1$		8_2^+	7_3^+
	1389.2(5)	18(4)					$E2/M1$		8_2^+	7_1^+
	1763.4(4)	104(6)	A	1.16(23)	1.15(24)	1.19(25)	$E2$		8_2^+[d]	6_3^+
4739.7(3)	892.9(3)	17(2)					$E2/M1$		(8_3^+)[e,k]	7_4^+
	1529.4(5)	15(3)					$(E2)$		(8_3^+)	(6_5^+)
	1800.7(5)	15(3)					$(E2)$		(8_3^+)	(6_4^+)
4815.4(2)	294.7(2)	8(2)					$\Delta I = 0$		8_2^-	8_1^-
	397.4(2)	8(2)					$E2/M1$		8_2^-	7_4^-
	525.0(2)	61(3)	f	1.00(9)	0.94(11)	1.14(13)	$E2/M1$		8_2^-	7_3^-
	811.4(3)	5(2)					$E2$		8_2^-	6_3^-
	969.8(4)	14(2)					$E1$		8_2^-	7_4^+
	1461.9(3)	76(4)	D	0.38(5)	0.65(9)	0.56(6)	$E2/M1$	$-0.28(^{10}_{17})$	8_2^-	7_1^-
	1497.6(6)	15(2)					$E2$		8_2^-	6_2^-
	1624.9(4)	35(4)	F	0.74(15)			$E1$		8_2^-	7_1^+
	1659.6(5)	5(1)					$E2$		8_2^-	6_1^-
4842.8(2)	425.1(3)	35(3)	e	1.04(15)	0.95(14)	1.20(14)	$E2/M1$	+0.23(10)	8_3^-	7_4^-
	552.5(2)	244(11)	e	1.04(8)	1.05(9)	1.02(7)	$E2/M1$	$+0.24(^{6}_{5})$	8_3^-	7_3^-
	838.7(5)	14(3)					$E2$		8_3^-	6_3^-
	996.0(5)	5(2)					$E1$		8_3^-	7_4^+
	1071.2(3)	16(3)					$E2/M1$		8_3^-	7_2^-
	1097.6(5)	9(2)					$E1$		8_3^-	7_3^+
	1488.4(3)	118(7)	D	0.28(4)	0.47(7)	0.57(6)	$E2/M1$	$-1.0(^{4}_{6})$	8_3^-	7_1^-
	1523.8(7)	15(2)	e,g,h	$\gg 1$			$E2$		8_3^-	6_2^-
	1652.0(6)	20(2)					$E1$		8_3^-	7_1^+
4996.4(2)	922.4(4)[f]	17(2)					$E1$		9_1^-	8_1^+
	1223.8(5)	12(2)					$E2$		9_1^-	7_2^-
	1642.8(6)	109(9)	D	0.97(6)	0.98(6)	0.96(6)	$E2$		9_1^-	7_1^-
5025.2(4)[l]	2208.1(8)	11(2)					$(E2)$		(8_4^+)[e]	6_3^+
5187.8(2)	667.0(3)	17(2)	N	$\ll 1$			$E2/M1$		9_2^-[c]	8_1^-
	1113.6(3)[f]	10(2)					$E1$		9_2^-	8_1^+
	1415.9(3)	181(6)	c	1.54(13)	1.34(13)	1.33(14)	$E2$[b]		9_2^-	7_2^-
	1833.4(4)	131(4)	N	1.00(11)	0.92(9)	1.10(10)	$E2$[b]		9_2^-	7_1^-
5246.3(2)	666.1(3)	31(2)	H	0.71(19)			$E2/M1$		9_1^+	8_2^+
	1172.5(5)	16(3)	G	0.56(12)			$E2/M1$		9_1^+	8_1^+
	1399.6(5)	18(2)					$E2$		9_1^+	7_4^+
	1501.2(5)	33(3)	a,b	1.34(23)	1.12(17)	1.16(17)	$E2$		9_1^+	7_3^+
	1874.6(6)	26(3)					$E2$		9_1^+	7_2^+
	2054.6(6)	62(4)	F	0.99(14)	1.02(14)	1.03(13)	$E2$		9_1^+	7_1^+
5349.0(4)	3151.6(13)	15(3)					$(E2)$		(8_5^+)[e]	6_1^+
5433.7(2)	590.8(2)	343(12)	L	0.78(10)	0.90(12)	0.85(9)	$E2/M1$	+0.20(4)	9_3^-	8_3^-
			d,g	1.03(5)	1.00(7)	1.00(6)				
	618.3(2)	162(7)	g	1.09(8)	1.03(9)	1.01(7)	$E2/M1$	+0.27(6)	9_3^-	8_2^-
	1016.0(4)	11(2)					$E2$		9_3^-	7_4^-
	1143.4(3)	86(4)	[i]				$E2$		9_3^-	7_3^-
	1359.3(5)	10(2)					$E1$		9_3^-	8_1^+

TABLE I. (*Continued.*)

E_x (keV)	E_γ (keV)	$I_{\gamma,\mathrm{rel}}$ (%)	Gate[a]	R_{DCO} 150°-97°	R_{DCO} 150°-127°	R_{DCO} 127°-97°	Mult. Ass't.	$\delta(E2/M1)$	I_i^π ($\hbar$)	I_f^π ($\hbar$)
5466.6(3)	726.8(5)	2(1)					$(E2/M1)$		(9_2^+)[e,k]	(8_3^+)
	886.3(3)	20(3)					$(E2/M1)$		(9_2^+)	8_2^+
	1620.0(6)	21(3)					$(E2)$		(9_2^+)	7_4^+
	1721.7(5)	16(2)					$(E2)$		(9_2^+)	7_3^+
	2095.0(8)	15(2)					$(E2)$		(9_2^+)	7_2^+
5648.5(2)	460.7(2)	118(5)	K,L	0.71(5)	0.82(6)	0.79(7)	$E2/M1$[b]	$+0.10(^{5}_{6})$	10_1^-[c]	9_2^-
	652.0(5)	15(3)	D,Q	0.57(7)	0.66(9)	0.73(7)	$E2/M1$	$-0.06(^{8}_{11})$	10_1^-	9_1^-
	1127.9(3)	298(11)	J	0.99(8)	0.98(7)	0.95(7)	$E2$[b]		10_1^-	8_1^-
5862.4(2)[m]	513.4(4)	5(1)	O	0.69(18)			$(E2/M1)$		9_3^+[d]	(8_5^+)
	616.0(4)	11(3)					$\Delta I=0$		9_3^+	9_1^+
	837.3(5)	13(2)	O[i]	0.59(15)	0.97(33)	0.89(18)	$(E2/M1)$	$\gtrsim 0$	9_3^+	(8_4^+)
	1282.2(3)	11(2)					$E2/M1$		9_3^+	8_2^+
	1341.7(3)	43(3)	O	0.53(9)	0.72(13)	0.62(9)	$E1$	$-0.06(^{10}_{13})$	9_3^+	8_1^-
	2490.9(8)	5(1)					$E2$		9_3^+	7_2^+
	2671.8(9)	12(2)	F,O,P	1.11(33)			$E2$		9_3^+	7_1^+
6008.7(4)[n]	983.4(5)	8(2)					$(E2/M1)$		9_4^+[d]	(8_4^+)
	2818.1(9)	11(2)	F,G,P	1.01(35)			$E2$		9_4^+	7_1^+
6076.4(2)	642.8(2)	425(13)	Q	0.73(5)	0.92(7)	0.86(6)	$E2/M1$	$+0.21(4)$	10_2^-	9_3^-
			e,h	1.06(5)	1.00(5)	1.01(5)				
	888.4(3)	7(2)					$E2/M1$		10_2^-	9_2^-
	1080.0(5)	4(1)					$E2/M1$		10_2^-	9_1^-
	1233.4(3)	70(4)	Q	1.22(41)	1.11(27)	1.04(32)	$E2$		10_2^-	8_3^-
			d,h	1.68(19)	1.20(14)	1.23(12)				
	1260.8(4)	36(3)	d	1.62(32)	1.16(21)	1.61(26)	$E2$		10_2^-	8_2^-
6094.1(2)	445.6(2)	82(3)	M	0.52(5)	0.82(9)	0.69(5)	$E2/M1$[b]	$-0.06(^{7}_{8})$	11_1^-[c]	10_1^-
	906.3(2)	150(10)	L	1.02(13)	1.03(12)	1.10(12)	$E2$[b]		11_1^-	9_2^-
	1097.7(6)	14(3)					$E2$		11_1^-	9_1^-
6279.6(3)	1033.4(4)[f]	11(2)					$E1$		10_3^-	9_1^+
	1283.3(6)	22(3)	D,Q	0.31(7)	0.70(12)	0.50(8)	$E2/M1$	$-0.4(3)$	10_3^-	9_1^-
	1758.6(6)	13(2)					$E2$		10_3^-	8_1^-
6391.6(3)	925.0(4)	17(3)					$E2/M1$		10_1^+[d]	(9_2^+)
	1145.2(4)	16(3)					$E2/M1$		10_1^+	9_1^+
	1811.6(6)	21(3)	H	0.94(25)	0.97(31)	0.86(25)	$E2$		10_1^+	8_2^+
	2317.6(11)	8(3)					$E2$		10_1^+	8_1^+
6442.0(4)	1195.8(4)	14(2)					$E2/M1$		10_2^+[d]	9_1^+
	1861.9(6)	12(2)					$E2$		10_2^+	8_2^+
6634.0(7)	1894.3(6)	11(3)					$(E2)$		(10_3^+)[e]	(8_3^+)
6851.8(2)	775.4(2)	374(14)	R	0.76(8)	0.84(9)	0.72(6)	$E2/M1$	$+0.18(7)$	11_2^-	10_2^-
			g	0.97(6)	1.05(7)	0.97(6)				
	1418.1(3)	103(6)	R	1.11(19)	1.14(19)	1.16(22)	$E2$		11_2^-	9_3^-
			e	1.38(17)	1.18(14)	1.32(13)				
6866.6(4)	1870.3(6)	24(2)	D,Q	0.42(13)			$E2/M1$		10_4^-	9_1^-
7137.0(5)	1890.6(6)	63(5)	a,b	1.67(50)	1.21(47)	1.73(56)	$E2$[d]		11_1^+[d]	9_1^+
7240.4(10)	2244.0(10)	15(2)								9_1^-
7394.4(2)[o]	527.1(6)	2(1)					$E1$		11_2^+[c]	10_4^-
	1114.9(3)	26(3)	P	0.59(11)	0.62(12)	0.92(14)	$E1$	$+0.01(12)$	11_2^+	10_3^-
	1385.6(4)	48(4)	P	1.07(13)	0.95(12)	1.09(16)	$E2$		11_2^+	9_4^+
	1531.9(4)	113(6)	P	1.00(8)	0.97(8)	0.98(8)	$E2$		11_2^+	9_3^+
	1745.8(3)	222(7)	M,P	0.55(4)	0.68(5)	0.74(5)	$E1$[b]	$-0.05(^{5}_{6})$	11_2^+	10_1^-
7457.0(4)[p]	1065.4(5)	6(2)					$(\Delta I=1)$		(11_3^+)[e]	10_1^+
	2211.3(14)	5(2)					$(E2)$		(11_3^+)	9_1^+
7563.2(4)	696.6(3)	5(1)					$(E2/M1)$		(11_3^-)[e]	10_4^-
	1469.2(6)	15(2)					$(\Delta I=0)$		(11_3^-)	11_1^-
7721.8(3)	869.9(2)	225(8)	L,S	0.67(6)	0.83(7)	0.81(7)	$E2/M1$	$+0.15(7)$	12_1^-	11_2^-
			h	1.05(7)	0.92(6)	1.00(6)				
	1645.3(7)	97(7)	g[i]	1.38(35)	1.16(27)	1.21(2)	$E2$		12_1^-	10_2^-

TABLE I. (*Continued.*)

E_x (keV)	E_γ (keV)	$I_{\gamma,\mathrm{rel}}$ (%)	Gate[a]	R_{DCO} 150°-97°	R_{DCO} 150°-127°	R_{DCO} 127°-97°	Mult. Ass't.	$\delta(E2/M1)$	I_i^π ($\hbar$)	I_f^π ($\hbar$)
8006.8(22)	3010.4(22)	5(2)								9_1^-
8016.0(6)	2366.7(8)	20(3)					$(E2/M1)$[k]		(11_4^-)	10_1^-
8132.6(2)	410.6(4)[f]	2(1)					$E1$		13_1^+[c]	12_1^-
	738.2(2)	455(18)	M,O	1.06(7)	1.07(6)	1.05(6)	$E2$[b]		13_1^+	11_2^+
	995.6(5)	7(2)					$E2$		13_1^+	11_1^+
	2038.2(7)	31(2)	N	1.18(20)	1.24(19)	1.24(21)	$E3/M2$[b]	$0.1 < \delta < 1.8$	13_1^+	11_1^-
	2484.6(7)	10(2)					$E3$		13_1^+	10_1^-
8332.2(5)	769.0(4)	2(1)					$(E2/M1)$		(12_2^-)[e]	(11_3^-)
	1465.7(6)	8(3)					$(E2)$		(12_2^-)	10_4^-
8439.8(7)	2345.9(7)	18(3)	K,N	1.27(35)	1.47(47)	1.33(31)	$(E2/M1)$	$(0.4 < \delta < 2.6)$	(12_3^-)[i]	11_1^-
8485.7(4)	2391.8(7)	16(3)					$(\Delta I = 0, 1)$		$(11_4^+, 12)$	11_1^-
8581.4(9)	2932.9(9)	10(2)								11_1^-
8592.2(6)	575.6(5)	3(1)					$(E2/M1)$		(12_4^-)[k]	(11_4^-)
	1726.5(6)	5(2)					$(E2)$		(12_4^-)	10_4^-
8625.3(3)	903.5(2)	145(5)	e,g,h	1.03(6)	0.90(6)	0.97(5)	$E2/M1$	+0.16(6)	13_1^-	12_1^-
	1773.6(4)	91(5)	L	1.19(30)	1.10(23)	0.93(26)	$E2$		13_1^-	11_2^-
			h	1.42(15)	1.22(13)	1.48(13)				
8645.7(7)	630.3(7)	4(1)					$(E2/M1)$		(12_5^-)[k]	(11_4^-)
	1778.1(9)	3(1)					$(E2)$		(12_5^-)	10_4^-
	2997.4(18)	8(2)					$(E2)$		(12_5^-)	10_1^-
8920.4(3)	434.8(4)	4(2)					$(\Delta I = 0, 1)$		12_1^+[d]	$(11_4^+, 12)$
	787.8(3)	34(3)	P	0.63(9)	0.80(12)	0.68(7)	$E2/M1$	+0.05(5)	12_1^+	13_1^+
			j	0.95(11)	0.96(12)	1.03(10)				
	1463.4(5)	38(5)	j	0.97(17)	1.00(24)	1.42(43)	$(\Delta I = 1)$	$+0.05(^{11}_{10})$	12_1^+	(11_3^+)
	1526.2(6)	17(3)					$E2/M1$		12_1^+	11_2^+
	2479.1(9)	6(2)	j	1.77(61)			$E2$		12_1^+	10_2^+
	2528.6(9)	5(2)	j	1.28(50)			$E2$		12_1^+	10_1^+
9094.4(4)[q]	961.7(5)	9(2)					$E2/M1$		12_2^+[d]	13_1^+
	1957.3(6)	11(3)					$E2/M1$		12_2^+	11_1^+
	2652.6(11)	8(2)					$E2$		12_2^+	10_2^+
9325.9(9)	886.4(8)	3(1)					$(E2/M1)$		(13_2^-)[k]	(12_3^-)
	3230.9(14)	9(2)	K,N	1.35(58)			$(E2)$		(13_2^-)	11_1^-
9394.4(11)	3300.4(13)	14(3)	K,N	1.26(46)			$(\Delta I = 1, 2)$[k]		$(12, 13_3^-)$	11_1^-
9447.3(12)	3353.0(15)	7(2)					$(\Delta I = 1, 2)$[k]		$(12, 13_4^-)$	11_1^-
9459.6(3)	834.4(2)	101(6)	R	0.70(10)	0.78(12)	0.70(9)	$E2/M1$	+0.16(4)	14_1^-	13_1^-
			e,g,h	0.95(7)	0.98(8)	1.02(6)				
	1737.8(4)	64(5)	e,g,h	1.45(12)	1.14(13)	1.46(12)	$E2$		14_1^-	12_1^-
9527.9(3)	433.4(3)	31(2)	k	1.10(12)	0.93(13)	0.90(9)	$E2/M1$	$+0.10(^{6}_{7})$	13_2^+	12_2^+
	607.6(2)	104(4)	P,T	0.69(6)	0.83(8)	0.70(6)	$E2/M1$	+0.07(3)	13_2^+	12_1^+
			k	0.94(7)	0.93(8)	0.98(6)				
	1042.2(6)	5(2)					$(\Delta I = 1, 2)$		13_2^+	$(11_4^+, 12)$
9838.8(4)	1506.5(8)	3(2)					$(E1)$		13_3^+[d]	(12_2^-)
	1706.1(6)	11(3)					$\Delta I = 0$		13_3^+	13_1^+
	2444.8(8)	20(2)					$E2$		13_3^+	11_2^+
10182.5(3)	654.8(4)	69(3)	T	0.52(10)	0.60(13)	0.67(14)	$E2/M1$	+0.09(7)	14_1^+	13_2^+
			j	1.10(13)	1.21(13)	1.03(13)				
	1088.0(5)	13(4)					$E2$		14_1^+	12_2^+
	1262.4(5)	8(2)					$E2$		14_1^+	12_1^+
	2049.6(5)	122(5)	P,T	1.31(8)	1.28(8)	1.06(7)	$E2/M1$	$+1.07(^{31}_{24})$	14_1^+	13_1^+
			k	2.01(28)	1.41(18)	1.24(16)				
10293.5(11)	967.6(6)	4(1)					$(E2/M1)$[k]		(14_2^-)	(13_2^-)
10335.0(4)	807.0(5)	10(3)					$E2/M1$		14_2^+	13_2^+
	2202.1(6)	69(4)	P	1.63(32)	1.34(21)	1.05(26)	$E2/M1$	$\approx +1$	14_2^+	13_1^+

TABLE I. (*Continued.*)

E_x (keV)	E_γ (keV)	$I_{\gamma,\mathrm{rel}}$ (%)	Gate[a]	R_{DCO} 150°-97°	R_{DCO} 150°-127°	R_{DCO} 127°-97°	Mult. Ass't.	$\delta(E2/M1)$	I_i^π ($\hbar$)	I_f^π ($\hbar$)
			k	2.08(43)	1.32(28)	1.19(21)				
10602.7(4)	1143.5(4)	74(4)	S[i]	0.73(10)	1.07(16)	0.91(11)	$E2/M1$	+0.20(6)	15_1^-	14_1^-
			d,e	1.07(11)	0.99(13)	0.98(12)				
	1976.6(6)	25(3)	R	1.25(37)	0.85(26)	1.01(23)	$E2$		15_1^-	13_1^-
10863.9(8)	2238.8(9)	5(2)	e,g,h	1.07(22)	0.88(20)	0.99(18)	$E2/M1$		14_3^-	13_1^-
	3141.8(13)	4(2)					$E2$		14_3^-	12_1^-
11042.9(4)	707.7(4)	21(2)	k	0.99(20)	1.10(29)	0.97(17)	$E2/M1$	$+0.08(^{12}_{10})$	15_1^+	14_2^+
	860.6(4)	94(4)	P,T	0.65(7)	0.78(7)	0.73(6)	$E2/M1$	+0.11(6)	15_1^+	14_1^+
			k	1.01(13)	1.00(19)	1.12(13)				
	1515.0(7)	40(5)	j,k[i]	1.62(15)	1.24(12)	1.42(13)	$E2$		15_1^+	13_2^+
11087.9(16)	4992.8(24)	3(1)					$(E2)$[k]		(13_5^-)	11_1^-
11371.8(12)	1924.5(10)	2(1)					$(E2)$[k]		$(14, 15_2^-)$	$(12, 13_4^-)$
	1977.4(8)	4(1)					$(E2)$[k]		$(14, 15_2^-)$	$(12, 13_3^-)$
11379.8(7)	1541.4(8)	27(4)					$E2$		15_2^+	13_3^+
	3247.4(12)	49(5)	P,V	1.08(22)			$E2$		15_2^+	13_1^+
11465.0(7)	1626.2(8)	4(2)					$E2$		15_3^+[d]	13_3^+
	3331.1(14)	14(2)	P	1.04(28)			$E2$		15_3^+	13_1^+
11693.0(4)	650.1(3)	92(5)	T	0.62(9)	0.79(14)	0.83(14)	$E2/M1$	$+0.08(^{8}_{10})$	16_1^+	15_1^+
	1358.1(6)	16(4)					$E2$		16_1^+	14_2^+
	1510.3(5)	69(4)	j,k[i]	1.62(15)	1.24(12)	1.42(13)	$E2$		16_1^+	14_1^+
11726.0(16)	3593.4(16)	11(2)	P	1.04(41)			$(E2)$		(15_4^+)	13_1^+
11761.4(15)	673.5(6)	2(1)					$(E2/M1)$[k]		(14_4^-)	(13_5^-)
12333.7(10)	2151.2(9)	11(2)	P	0.98(33)			$(E2)$		(16_2^+)	14_1^+
12430.2(6)	1827.6(6)	12(2)	e,g,h	1.10(21)	0.94(16)	0.97(15)	$E2/M1$	+0.19(10)	16_1^-	15_1^-
	2970.4(9)	4(2)	e,g,h	1.52(67)	1.03(39)	1.24(28)	$E2$		16_1^-	14_1^-
12479.2(14)	1391.0(14)	2(1)					$(E2)$[k]		(15_3^-)	(13_5^-)
	3854.4(16)	4(1)					$(E2)$[k]		(15_3^-)	(13_1^-)
12560.5(5)	867.6(3)	120(7)	T	0.41(4)	0.79(8)	0.67(6)	$E2/M1$	$-0.09(^{6}_{7})$	17_1^+	16_1^+
	1517.6(7)	38(4)	j,k[i]	1.62(15)	1.24(12)	1.42(13)	$E2$		17_1^+	15_1^+
12617.4(26)	4484.8(26)	2(1)					$(E2)$[k]		(15_5^+)	13_1^+
13183.7(23)[r]	4558.4(23)	3(1)					$(E2)$[k]		(15_4^-)	13_1^-
13239.3(15)	760.0(7)	2(1)					$(E2/M1)$[k]		(16_2^-)	(15_3^-)
	1477.9(8)	3(1)					$(E2)$[k]		(16_2^-)	(14_4^-)
13298.4(8)	1832.8(9)	6(2)					$E2$		17_2^+	15_3^+
	1919.1(7)	41(4)	P,U	0.93(18)			$E2$		17_2^+	15_2^+
13727.0(6)	1166.6(5)	79(5)	T	0.57(6)	0.86(10)	0.73(9)	$E2/M1$	+0.02(6)	18_1^+	17_1^+
			k	0.80(8)	0.80(9)	0.98(9)				
	2033.8(8)	15(3)	T	1.05(27)	1.04(29)	1.03(25)	$E2$		18_1^+	16_1^+
			k	1.59(29)	1.42(26)	1.35(27)				
13896.4(20)	2524.6(16)	3(1)					$(E2)$[k]		$(16, 17_1^-)$	$(14, 15_2^-)$
14084.7(17)	1605.5(9)	6(1)					$(E2)$[k]		(17_2^-)	(15_3^-)
14689.8(25)	1506.1(8)	7(2)					$(E2)$[k]		(17_3^-)	(15_4^-)
14770.7(19)	4168.0(18)	3(1)					$(E2)$[k]		(17_4^-)	15_1^-
14980.1(22)	4377.4(22)	3(1)					$(E2)$[k]		(17_5^-)	15_1^-
14986.0(20)	1746.7(13)	5(2)					$(E2)$[k]		(18_1^-)	(16_2^-)
15492.8(13)	2194.3(10)	23(3)	P,U,V	1.16(28)			$(E2)$		(19_1^+)	17_2^+
15634.7(8)	1907.9(8)	9(2)					$(E2/M1)$[k]		(19_2^+)	18_1^+
	3073.9(11)	5(2)					$(E2)$[k]		(19_2^+)	17_1^+
16000.1(19)	1915.4(10)	6(1)					$(E2)$[k]		(19_1^-)	(17_2^-)
16522.6(27)	1832.8(11)	6(2)					$(E2)$[k]		(19_2^-)	(17_3^-)
17074.9(22)	2088.9(9)	4(1)					$(E2)$[k]		(20_1^-)	(18_1^-)
18190.7(18)	2697.9(12)	5(1)					$(E2)$[k]		(21_1^+)	(19_1^+)

TABLE I. (*Continued.*)

E_x (keV)	E_γ (keV)	$I_{\gamma,\mathrm{rel}}$ (%)	Gate[a]	R_{DCO} 150°-97°	R_{DCO} 150°-127°	R_{DCO} 127°-97°	Mult. Ass't.	$\delta(E2/M1)$	I_i^π ($\hbar$)	I_f^π ($\hbar$)
18263.3(23)	2263.2(13)	4(1)					$(E2)$[k]		(21_1^-)	(19_1^-)
18712.2(32)	2189.6(17)	2(1)					$(E2)$[k]		(21_2^-)	(19_2^-)
19514.8(27)	2439.9(16)	2(1)					$(E2)$[k]		(22_1^-)	(20_1^-)

[a]Gating $E2$ and dipole transitions are marked with capital and lower-case letters, respectively. A: 557 keV ($4_1^+ \to 2_1^+$); B: 823 keV ($5_1^+ \to 3_2^+$); C: 1325 keV ($5_2^+ \to 3_1^+$); D: 1640 keV ($6_1^+ \to 4_1^+$); E: 1186 keV ($6_2^+ \to 4_3^+$); F: 1587,1593 keV ($7_{1,2}^+ \to 5_{1,2}^+$); G: 1382 keV ($8_1^+ \to 6_2^+$) and 1386 keV ($11_2^+ \to 9_4^+$); H: 1763 keV ($8_2^+ \to 6_3^+$); J: 1365 keV ($8_1^- \to 6_1^-$); K: 1833 keV ($9_2^- \to 7_1^-$); L: 1416 keV ($9_2^- \to 7_2^-$) and 1418 keV ($11_2^- \to 9_3^-$); M: 1128 keV ($10_1^- \to 8_1^-$); N: 906 keV ($11_1^- \to 9_2^-$); O: 1532 keV ($11_2^+ \to 9_3^+$); P: 738 keV ($13_1^+ \to 11_2^+$); Q: 1643 keV ($9_1^- \to 7_1^-$) and 1645 keV ($12_1^- \to 10_2^-$); R: 1774 keV ($13_1^- \to 11_2^-$); S: 1738 keV ($14_1^- \to 12_1^-$); T: 1510-, 1515-, and 1518-keV $E2$ transitions in structure D3; U: 3247 keV ($15_2^+ \to 13_1^+$); V: 1919 keV ($17_2^+ \to 15_2^+$); a: 790 keV ($6_3^+ \to 5_3^+$); b: 928 keV ($7_3^+ \to 6_3^+$); c: 461 keV ($10_1^- \to 9_2^-$); d: 553 keV ($8_3^- \to 7_3^-$); e: 591 keV ($9_3^- \to 8_3^-$); f: 618 keV ($9_3^- \to 8_2^-$); g: 643 keV ($10_2^- \to 9_3^-$); h: 775 keV ($11_2^- \to 10_2^-$); j: 608 keV ($13_2^+ \to 12_1^+$); k: 650 keV ($16_1^+ \to 15_1^+$) and 655 keV ($14_1^+ \to 13_2^+$).
[b]Multipolarity assignment also based on previous work [20,21].
[c]Spin-parity assignment also based on previous work [20,21].
[d]Spin-parity or multipole assignment also based on DCO ratios of feeding transitions or a sequence of stretched quadrupole transitions between states with otherwise established spin-parity assignment.
[e]Tentative spin-parity assignment based on yrast arguments and γ-ray connections into and out of the level.
[f]Transition not shown in Fig. 2.
[g]Transitions carrying 33(9) intensity units out of the level remained unobserved.
[h]Transitions carrying 98(16) intensity units out of the level remained unobserved.
[i]Doublet structure.
[j]Transitions carrying 24(6) intensity units out of the level remained unobserved.
[k]Tentative assignment based on yrast arguments and collective structure.
[l]Transitions carrying 10(3) intensity units out of the level remained unobserved.
[m]Transitions carrying 11(8) intensity units out of the level remained unobserved.
[n]Transitions carrying 29(6) intensity units out of the level remained unobserved.
[o]Transitions carrying 81(21) intensity units out of the level remained unobserved.
[p]Transitions carrying 27(5) intensity units out of the level remained unobserved.
[q]Transitions carrying 16(6) intensity units out of the level remained unobserved.
[r]Transitions carrying 4(2) intensity units out of the level remained unobserved.

The spins and parities of the majority of observed states could be determined from γ-ray yields measured by the Ge detectors placed at different angles with respect to the beam axis. This method uses the fact that nuclei being produced in fusion-evaporation reactions have their spin vectors aligned approximately in a plane perpendicular to the beam axis. Furthermore, the angular distribution of γ rays is symmetric with respect to the beam axis. This allowed for an analysis of directional correlations from oriented states (so-called DCO ratios). Balancing γ-ray yield with angular precision, the Ge detectors of Gammasphere were grouped into three "pseudo" rings called "150°", "127°", and "97°", which correspond to an average angle for the respective sets of detectors (see, e.g., Ref. [3] and references therein). Three combinations of the angles were created and sorted into matrices, namely, (150°-97°), (150°-127°), and (127°-97°). For instance, the DCO ratio of (150°-97°) was defined as

$$R_{\mathrm{DCO}}(150^\circ\text{-}97^\circ) = \frac{I(\gamma_1 \text{ at } 150^\circ;\ \text{gated with } \gamma_2 \text{ at } 97^\circ)}{I(\gamma_1 \text{ at } 97^\circ;\ \text{gated with } \gamma_2 \text{ at } 150^\circ)}.$$

For this case, γ-ray intensities were derived from a $3p1n$-selected $\gamma\gamma$ matrix, with the γ rays detected at 150° sorted on one axis and 97° on the other axis. The DCO ratios for the angle combinations (150°-127°) and (127°-97°) were defined and processed accordingly. The intensities of the γ rays were corrected for the efficiency of a given pseudo ring. The R_{DCO} values for all three combinations of angles are listed in Table I.

The R_{DCO} values were obtained by analyzing spectra in coincidence with known stretched $E2$ and $\Delta I = 1$ transitions. Depending on the character of the coincident transitions, different values of R_{DCO} will be obtained. In case the gating transition has a stretched $E2$ character:

$R_{\mathrm{DCO}}(150^\circ\text{-}97^\circ) \approx 1.0$ for stretched $E2$ transitions;

$R_{\mathrm{DCO}}(150^\circ\text{-}97^\circ) \approx 0.9$ for $\Delta I = 0$ transitions;

$R_{\mathrm{DCO}}(150^\circ\text{-}97^\circ) \approx 0.6$ for stretched $\Delta I = 1$ transitions.

In case the gating transition has a stretched and pure $\Delta I = 1$ character:

$R_{\mathrm{DCO}}(150^\circ\text{-}97^\circ) \approx 1.6$ for $E2$ transitions;

$R_{\mathrm{DCO}}(150^\circ\text{-}97^\circ) \approx 1.5$ for $\Delta I = 0$ transitions;

$R_{\mathrm{DCO}}(150^\circ\text{-}97^\circ) \approx 1.0$ for stretched $\Delta I = 1$ transitions.

Deviations from the latter values are usually caused by quadrupole admixtures into dipole transitions, i.e., nonzero $\delta(T2/T'1)$ mixing ratios with $T, T' = E, M$ or M, E, respectively (see below). Furthermore, loss of spin alignment could occur because of intermediate γ-ray emissions between the gating and evaluated transitions, or due to unusually long lifetimes ($\tau \gtrsim 1$ ns) of states involved in the γ-ray cascade of interest.

For a given γ-ray transition, the derivation of mixing ratios relied on the three different angle combinations, i.e., three available R_{DCO} values. For some prominent cases, gating with $E2$ *and* stretched $\Delta I = 1$ transitions was possible, i.e., the mixing ratio could be determined as the weighted mean of $2 \times 3 = 6$ data points. Furthermore, the phase convention applied in the Evaluated Nuclear Structure Data Files (ENSDF) was used. The spin alignment coefficients, α, were estimated through the relation [3] $\alpha = 0.55 + 0.02E_x$ (MeV). An uncertainty of $\Delta\alpha = \pm 0.05$ was set.

Figure 1 exemplifies the method for four cases of mixed $\Delta I = 1$ transitions. For all of them, the gating transition is of stretched $E2$ character. Therefore, the theoretical curves for a given combination of detector angles are very similar, not least because the spin alignments are also comparable in size. The three panels of Fig. 1(a) focus on the parity-changing 1157-keV transition [21]. The set of three experimental DCO ratios provides consistent regimes for crossing the calculated curves as a function of mixing ratio δ, indicated by the gray-shaded areas projected onto the x axes. Here, the weighted mean is $\delta(M2/E1) = -0.11(^{5}_{7})$. Interestingly, this value implies a small but nonzero $M2$ admixture. The second example presents the overall rather low DCO values of the 1488-keV $8^-_3 \to 7^-_1$ transition, which is one out of many links between the dipole structure D2 (cf. Sec. IV B) and the more irregular low-spin shell-model part (cf. Sec. IV A) of the ^{60}Cu level scheme. For this transition, all DCO ratios (cf. Table I) are consistent with a rather distinct negative mixing ratio, $\delta(E2/M1) = -1.0(^{4}_{6})$. The example of Fig. 1(c) dwells on the rather intense 870-keV dipole transition, which is one of many such transitions defining structure D2. In this case, the DCO ratios shown in the figure, as well as additional ones based on gating on dipole transitions within D2 yield $\delta(E2/M1) = +0.15(7)$. Notably, all main dipole transitions of structure D2 exhibit similarly small but nonzero positive mixing ratios (cf. Table I and Sec. IV B). Finally, the plots in Fig. 1(d) provide the analysis of the 2050-keV, $14^+_1 \to 13^+_1$ transition, which connects dipole structure D3 (cf. Sec. IV C) with the established 13^+_1 yrast state at 8133 keV [21]. In this case, all experimental DCO ratios are unusually large, which, when combined, leads to a large positive mixing ratio of $\delta(E2/M1) = +1.07(^{31}_{24})$.

For states populated or depopulated by relatively weak γ-ray transitions without reliable angular-correlation information, spins, and parities are suggested based on either yrast arguments, i.e., that states closer to the yrast line are typically more strongly populated by means of fusion-evaporation reactions, the fact that they can be considered part of a regular dipole or quadrupole structure, or a combination of both. These are marked accordingly in Table I, as are spins and parities established in earlier work [20,21].

IV. RESULTS

From an analysis of γ rays identified in spectra with a given selection of evaporated particles and feeding the ground states of the more than 20 residual nuclei observed in the

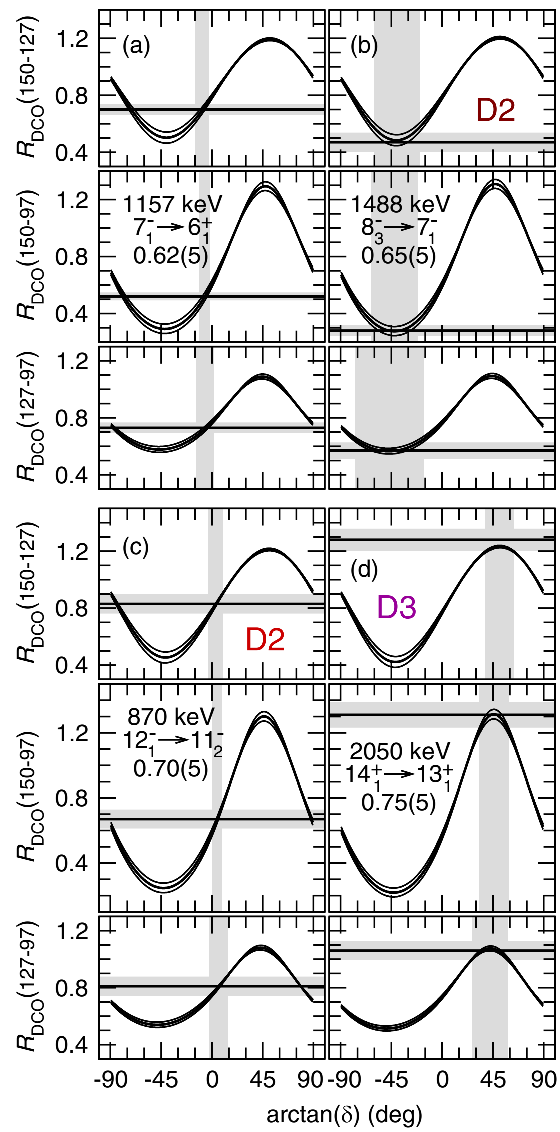

FIG. 1. Examples of the analysis of mixing ratios. The horizontal lines together with the uncertainty band marked in gray correspond to the experimental DCO values for the respective set of angle combinations (see Table I). The curves correspond to the calculated DCO ratios for different mixing ratios, $\delta(E2/M1)$, for a given alignment. The intersections of the experimental lines and theoretical curves provide the possible mixing ratios for a given transition. For each of the four transitions in panels (a)–(d), γ-ray energies, placement in the level scheme, and alignment are given. See text for details.

^{36}Ar + ^{28}Si reaction, a relative residue yield $\sigma_{rel} \approx 12\%$ is estimated for the $3p1n$ channel ^{60}Cu. The value is about a third of that for the strongest reaction channel, ^{58}Ni + $\alpha 2p$ [10], and is comparable to those of the ^{61}Cu + $3p$ [14] and ^{60}Ni + $4p$ [12] channels. Thus, ^{60}Cu is the most strongly populated reaction channel involving neutron evaporation, and the combination of data from three nearly identical Gammasphere experiments provides a dataset of high statistical significance. For instance, the $3p1n$-selected $\gamma\gamma$ matrix (cf. Sec. III) comprises more than 75 million coincidence entries, of which >90% can be associated with ^{60}Cu. In Table I, γ-ray

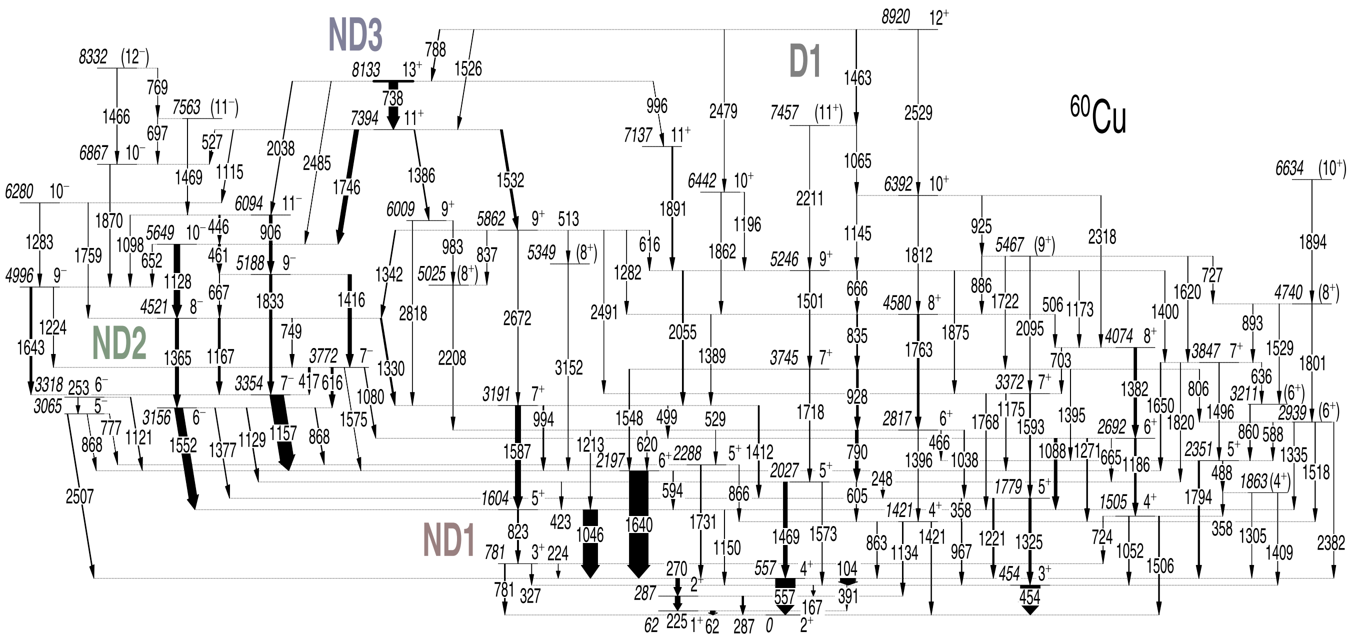

FIG. 2. Low- to medium-spin part of the level scheme of ^{60}Cu from the present study. Energy labels are in keV. The widths of the arrows correspond to the relative intensities of the γ rays. The labels "ND1" and "ND2" indicate regions of positive- and negative-parity yrast states, respectively (cf. Fig. 16). The 8133-keV 13^+ yrast level is part of structure "ND3" and is shown with a thicker line to guide the eye (cf. Figs. 6 and 8). The label "D1" (gray, ●) indicates a tentative dipole structure in the center of the figure. For the sake of clarity, four $E1$ transitions and one $E2/M1$ transition are not included in this figure: $E_\gamma = 922$ keV $9^-_1 \rightarrow 8^+_1$ ($E_x = 4996$ keV), $E_\gamma = 1114$ keV $9^-_2 \rightarrow 8^+_1$ ($E_x = 5188$ keV), $E_\gamma = 1033$ keV $10^-_3 \rightarrow 9^+_1$ ($E_x = 6280$ keV), $E_\gamma = 411$ keV $13^+_1 \rightarrow 12^-_1$ ($E_x = 8133$ keV), and $E_\gamma = 1160$ keV $(6^+_4) \rightarrow 5^+_2$ ($E_x = 2939$ keV). See also Table I.

yields are normalized to the 454-keV, $3^+_1 \rightarrow 2^+_1$ ground-state transition, which is set to 1100 intensity units. In the course of the $\gamma\gamma\gamma$ analysis, transitions were unambiguously identified and placed in the decay scheme down to a few parts in a thousand in γ-ray yield. With a proper preselection of one or more than one γ ray identifying a given structure, this part of the decay scheme can be studied in greater detail with a correspondingly defined $\gamma\gamma$ coincidence matrix.

It has been possible to construct and propose a complex level scheme that can be grouped into a low-lying part of mostly irregular sequences of levels and one possible, weak dipole structure (named D1), two regular and distinct dipole structures (D2 and D3), as well as a number of rotational-like $E2$ sequences (Q1–Q4) at high excitation energy and angular momentum. To ease the presentation of the results, both the level scheme and the corresponding discussion is split into four parts and sections.

A color code has been implemented throughout to describe and highlight objects of the irregular low-spin pattern (black, ●), dipole structures D1 (gray, ●), D2 (brick red, ●), and D3 (violet, ●), and quadrupole structures Q1 (dark green, ●), Q2 (green, ●), Q3 (medium blue, ●), and Q4 (dark blue, ●).

A. The low- to medium-spin part

The low- to medium-spin part of the proposed level scheme of ^{60}Cu is displayed in Fig. 2. States along or near the yrast line are connected by the most intense transitions, which are recognized by the thickest arrows. Level energies as well as their spin-parity assignments are consistent with or supported by a previous study [21]. That study employed a backed target, implying that all recoiling nuclei were stopped in the center of the respective Ge-detector array within roughly 1 ps. From Fig. 4 in Ref. [21] it is apparent that at least the lifetime of the 8133-keV 13^+_1 yrast state exceeds the time it took to stop the recoils; all transitions of the main γ-ray cascade depopulating that state were emitted at rest.

The γ-ray spectra from the present study displayed in Figs. 3(a) and 3(c)–3(e) focus on previously unknown parts of the decay scheme, while the γ-ray spectrum in Fig. 3(b) features the known yrast decay cascade mentioned above. That spectrum is in coincidence with both the 738-keV $13^+_1 \rightarrow 11^+_2$ and 1552-keV $6^-_1 \rightarrow 5^+_1$ transitions. The sequence 1746-1128-1365 keV connects the intermediate 7394-keV 11^+_2 and 3156-keV 6^-_1 states; weaker branches through the 461-1416-616-keV cascade, as well as the 749-keV $8^-_1 \rightarrow 7^-_2$ transition, form parallel decay paths between these states. Transitions marked at 104, 225, 270, 454, 557, 823, and 1046 keV take the γ-ray flux from the 1604-keV 5^+_1 state to the ground state, while the 1532- and 1342-keV transitions define a previously unobserved side branch of the decay of the 7394-keV 11^+_2 state. This part of Fig. 2 is further described by the spectrum in Fig. 3(a), which is in coincidence with the 738-keV $13^+_1 \rightarrow 11^+_2$ and 1532-keV $11^+_2 \rightarrow 9^+_3$ transitions. Besides the already mentioned 1342-keV transition, additional weak decay branches of the 5862-keV 9^+_3 level are defined by the 2491- and 2672-keV high-energy transitions in the inset, and those of 513 and 837 keV. Through various parallel decay

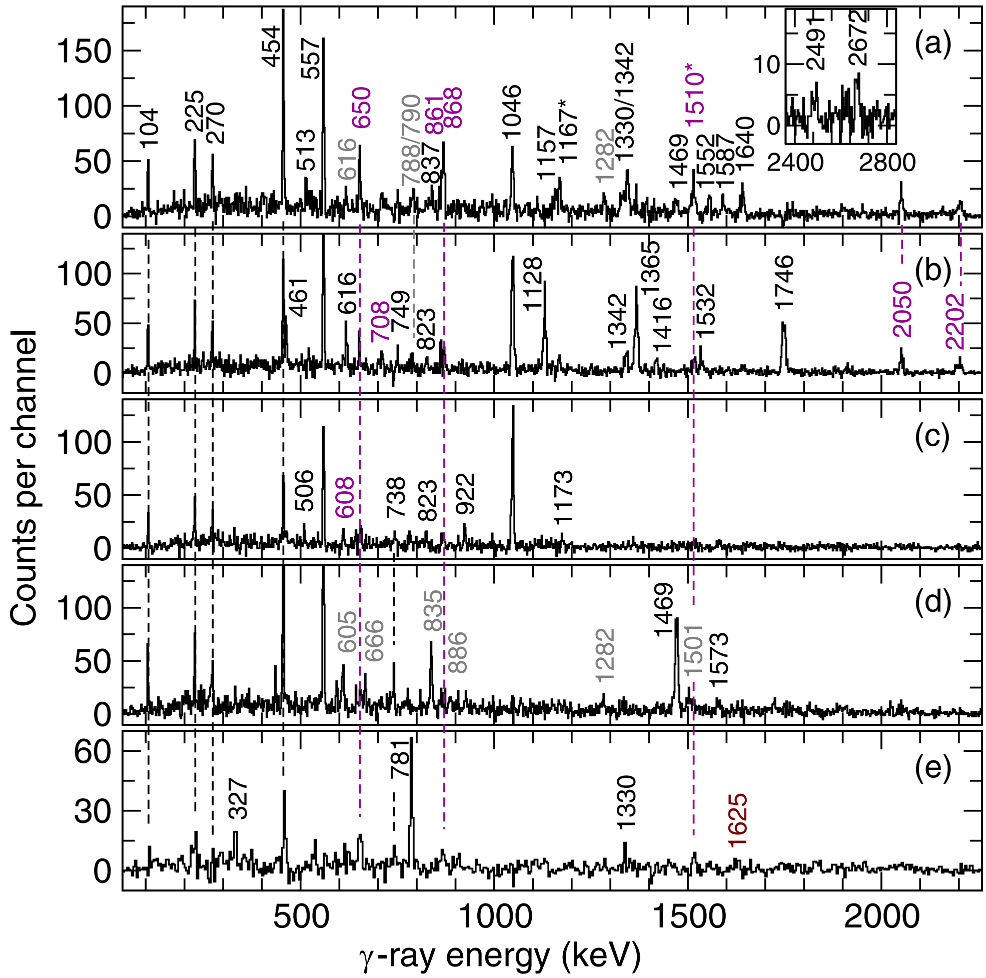

FIG. 3. Gamma-ray spectra from the $\gamma\gamma\gamma$ analysis of the low-to medium-spin part of the level scheme of ^{60}Cu (cf. Fig. 2). Energy labels are in keV. They follow the color code outlined in the text. An asterisk indicates a doublet. Dashed vertical lines are to guide the eye. The spectrum in panel (a) is in coincidence with the 738-keV $13^+_1 \to 11^+_2$ and 1532-keV $11^+_2 \to 9^+_3$ transitions. The inset shows a fraction of the high-energy range. The spectrum in panel (b) is in coincidence with the 738-keV $13^+_1 \to 11^+_2$ and 1552-keV $6^-_1 \to 5^+_1$ transitions. The spectrum in panel (c) is in coincidence with the 1088-keV $6^+_2 \to 5^+_1$ and 1382-keV $8^+_1 \to 6^+_2$ transitions. The spectrum in panel (d) is in coincidence with the 790-keV $6^+_3 \to 5^+_3$ and 928-keV $7^+_3 \to 6^+_3$ transitions associated with structure D1. The spectrum in panel (e) is in coincidence with the 823-keV $5^+_1 \to 3^+_2$ and 1587-keV $7^+_1 \to 5^+_1$ transitions. The spectra in panels (a)–(d) have a binning of 2 keV per channel, those of the inset in panel (a) and panel (e) have 4 keV per channel.

paths, most of the γ-ray flux is collected at the 557-keV 4^+_1 yrast state, followed by the already mentioned transitions at 104, 225, 270, 454, and 557 keV. Intermediate transitions at 1046, 1157, 1167, 1330, 1469, 1552 (see above), 1587, and 1640 keV relate to one of the weak decay branches between the 9^+_3 and 4^+_1 states. Transitions marked in violet in Figs. 3(a) and 3(b) belong to the dipole structure D3 (see Sec. IV C), while peaks with gray labels in Fig. 3(a) at 616, 788/790, and 1282 keV are part of or decay from the tentative dipole structure D1 shown in the center of Fig. 2.

The spectrum in Fig. 3(d) is in coincidence with the 790- and 928-keV dipole transitions associated with D1. Peaks at 605, 666, 835, and 1501 keV denote other members of D1, those at 886 and 1282 keV connect to side structures. The 1469- and 1573-keV transitions connect the 2027-keV 5^+_3 level with the yrast 4^+_1 and 3^+_1 states, which decay to the ground state with the set of γ rays observed at 104, 225, 270, 454, and 557 keV. Unmarked weaker peaks in Fig. 3(d) relate to connections into dipole structures D2 or D3 (see Secs. IV B and IV C).

The spectrum in Fig. 3(c) is in coincidence with the 1088-keV $6^+_2 \to 5^+_1$ and 1382-keV $8^+_1 \to 6^+_1$ transitions and illustrates parts of the level scheme on the right-hand side of Fig. 2. Besides the common transitions at 104, 225, 270, 454, 557, 823, and 1046 keV, which connect the 1604-keV 5^+_1 state with the ground state of ^{60}Cu, peaks at 506, 922, and 1173 keV are observed, which are found to feed the 4074-keV 8^+_1 level.

The spectrum in Fig. 3(e) is in coincidence with the 823-keV $5^+_1 \to 3^+_2$ and 1587-keV $7^+_1 \to 5^+_1$ transitions. Besides the 781-keV $3^+_2 \to 2^+_1$ ground-state transition, the decay from the 781-keV level can also proceed via transitions of 327 and 224 keV. The latter is a doublet with the more intense

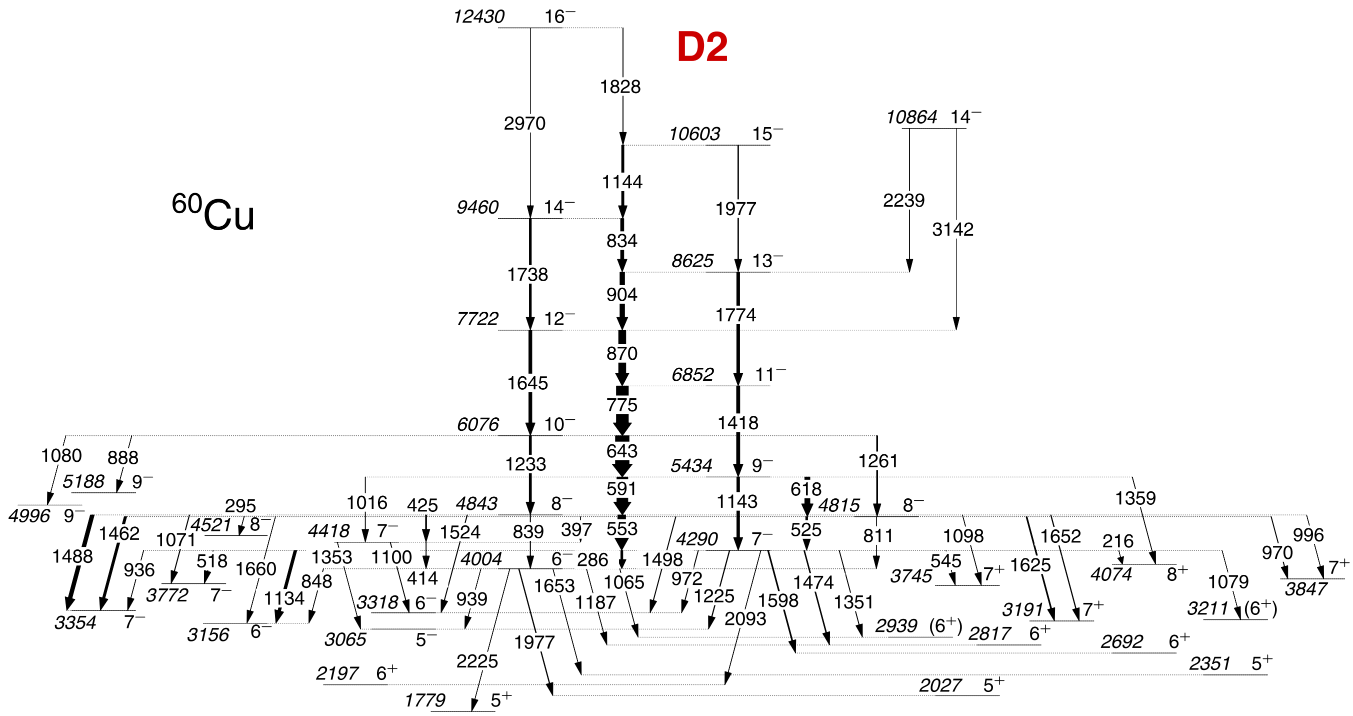

FIG. 4. Part of the level scheme of ^{60}Cu from the present study focusing on the dipole structure D2 (brick red) and its decay paths into the lower-lying structures (cf. Fig. 2). Energy labels are in keV. The widths of the arrows correspond to the relative intensities of the γ rays.

225-keV $2_2^+ \rightarrow 1_1^+$ transition. One can also observe the 1330-keV line feeding the 3191-keV 7_1^+ state, as well as indications of the 738-keV transition and members of D3, once the parallel decay branches of the related 7394-keV 11_2^+ state reconnect (see above and Sec. IV C). The weak 1625-keV line is one out of many transitions connecting D2 to the low- to medium-spin part of the level scheme.

There are indications of additional weak decay paths with <5 intensity units from the 2288-keV 5_4^+ state. These can be either a 783-keV transition into the 1505-keV state or a 1507-keV line into the 781-keV state or both. The apparent peak doublets prevent definite placements.

Definite spin and parity assignments of the vast majority of the states shown in Fig. 2 are possible based on earlier measurements [21] and the often many combinations of angular-correlation results for both populating and depopulating transitions. The few exceptions are the upper-left part and right-hand side of Fig. 2, where tentative assignments rely on yrast arguments, decay pattern, or anticipated structure.

It is worth noting that several low-lying $\Delta I = 1$ transitions reveal distinct negative mixing ratios. This concerns, e.g., the 781-, 1046-, or 1088-keV transitions. The DCO ratios for the 790- and 928-keV transitions of structure D1 indicate small positive mixing ratios $\delta(E2/M1) \approx +0.15$. Furthermore, the parity-changing 1157-keV $E1$ yrast transition exhibits a small but nonzero $M2$ admixture (see Sec. III). Finally, there are weak 2038-keV $E3/M2$ and 2485-keV $E3$ transitions depopulating the distinct 8133-keV 13_1^+ yrast state in parallel to the main 738-keV $13_1^+ \rightarrow 11_2^+$ $E2$ transition. This adds further evidence to the observations in Ref. [21] that the electromagnetic decay of the 13_1^+ state is hindered.

B. The dipole structure D2

Figure 4 focuses on a newly observed regular sequence of magnetic-dipole transitions, paralleled by weaker $E2$ transitions. This dipole structure D2 covers an excitation-energy range of approximately 4 to 12 MeV with spin-parity values of 6^- to 16^-. The presence and placement of D2 in the level scheme, including its comprehensive decay pattern, are evinced by the selected γ-ray spectra shown in Fig. 5. In fact, the well-resolved and detailed lower part of Fig. 4 reflects the high quality of the data from the combined statistics of three experiments with powerful reaction-channel-selection capabilities.

All spectra in Fig. 5 are in coincidence with one or more of the three main dipole transitions of D2 with energies of 591, 643, and 775 keV (cf. Fig. 4). The spectrum in Fig. 5(a) is, in addition, coincident with any of the 870-, 904-, or 1774-keV transitions placed on top of the 6852-keV 11_2^- state. It provides a survey of D2 as well as the structure's decay pattern and feeding transitions. To start with the latter, the 2239- and 3142-keV transitions are found to form a side structure reaching the 14_3^- level at 10 864-keV excitation energy. The DCO ratio of the 2239-keV transition is consistent with a parity-conserving $\Delta I = 1$ character. Furthermore, weak transitions of 3854 and 4558 keV mark links to quadrupole structures observed at high excitation energies. These are discussed below (Sec. IV D and Fig. 8). The terminating state of D2 at 12430 keV is justified by the presence of the following lines in Fig. 5(a): the 834-, 1144-, and 1828-keV dipole transitions and the 1738-, 1977-, and 2970-keV stretched $E2$ transitions. For all these high-lying transitions, DCO ratios can be extracted. Note that the 1144-keV $15_1^- \rightarrow 14_1^-$

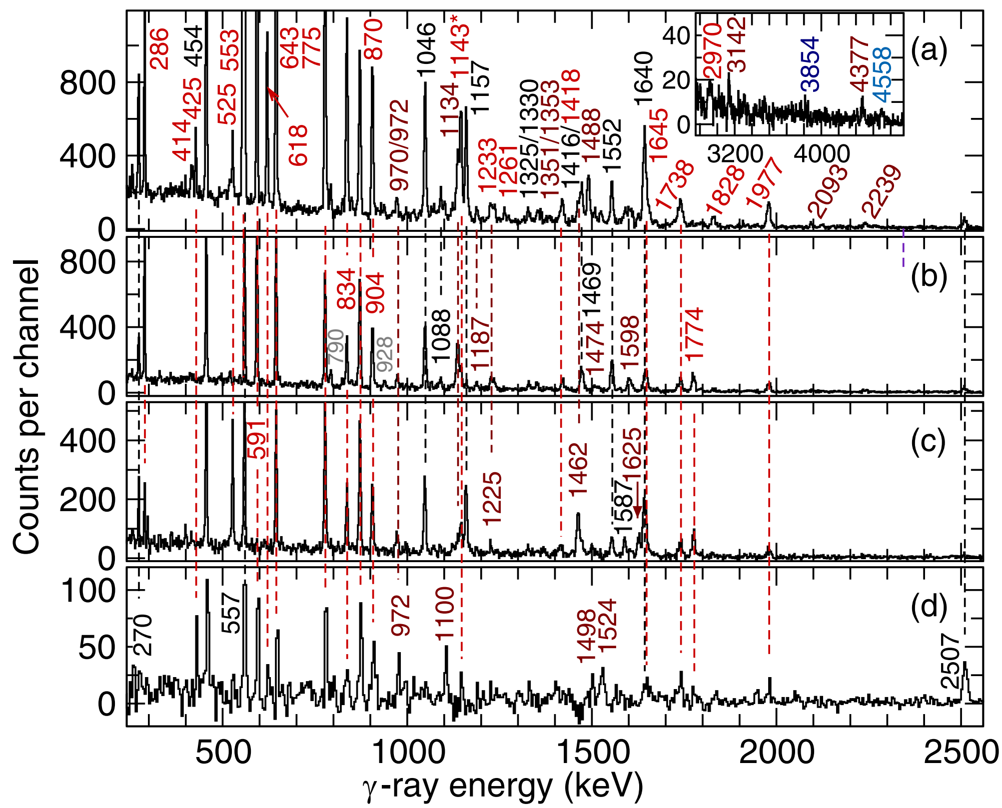

FIG. 5. Gamma-ray spectra from the $\gamma\gamma\gamma$ analysis of the level structure D2 of ^{60}Cu (cf. Fig. 4). Energy labels are in keV. They follow the color code outlined in the text. An asterisk indicates a peak doublet. Dashed vertical lines are to guide the eye. All spectra are in coincidence with any of the 591-, 643-, or 775-keV transitions defining D2. In addition, the spectrum in panel (a) is in coincidence with any of the 870-, 904-, or 1774-keV transitions (all D2), the spectrum in panel (b) with the 553-keV transition (D2), the spectrum in panel (c) with the 618-keV transition (D2), and the spectrum in panel (d) with the 253-keV $6^-_2 \rightarrow 5^-_1$ transition (cf. Fig. 2). The spectra in panels (a)–(c) have a binning of 2 keV per channel, those of panel (d) and the inset in panel (a) have 4 keV per channel.

dipole transition is a doublet with the 1143-keV $9^-_3 \rightarrow 7^-_3$ $E2$ transition.

At $E_x = 6076$ keV, the flux along D2 splits, in part, into two 8^- states (4815 and 4843 keV) and two 7^- states (4290 and 4418 keV). The state of D2 with the lowest spin and excitation energy is the 6^- level at 4004 keV. This gives rise to several side cascades within D2, parallel to the "central" 591-, 553-, 286-keV sequence. Despite the fact that the 286-keV $7^-_3 \rightarrow 6^-_3$ transition is a doublet with the 287-keV ground-state transition (cf. Fig. 2), it dominates the yield in Figs. 5(a)–5(c). Examples of the aforementioned parallel cascades are 591-425-414 keV, 618-525-286 keV, and 618-397-414 keV. Similarly, there are two parallel $E2$ transitions of 1233 and 1261 keV connecting the 10^- state in D2 with two close-lying 8^- states.

Starting with the 10^- state at 6076 keV, there are many decay paths connecting D2 with yrast or near-yrast states of both positive and negative parity. Prominent ones are, according to Fig. 5(a), the 970/972-keV and 1351/1353-keV doublets, and the 1134-, 1488-, and 2093-keV transitions. Of particular interest are the dipole transitions with the respective energies of 1134, 1462 [cf. Fig. 5(c) and discussion below], and 1488 keV. All three of them have mixing ratios distinctively different from zero [cf. Fig. 1(b)]. This settles the negative-parity assignment for D2, because the transitions in question connect D2 with the established 6^-_1 and 7^-_1 yrast states at 3156 and 3354 keV, respectively (cf. Fig. 2). Furthermore, dipole connections from D2 to positive-parity states show DCO ratios consistent with mixing ratios of zero, i.e., $E1$ character.

The spectrum in Fig. 5(b) is in coincidence with the 553-keV transition which feeds the 4290-keV 7^-_2 state in D2. In addition to the 286-keV in-band and 1134 keV decay-out transition (mentioned above), a set of additional peaks from decays into primarily positive-parity states can be seen. For instance, the 1187- and 1598-keV lines, as well as a 1474 keV peak that explains the high-energy tail of the 1469-keV line, lead into structure D1 (cf. Sec. IV A). The 790- and 928-keV transitions are members of D1. Altogether thirteen γ rays depopulating the 4290-keV state have been found, but still some of its decay flux remains unobserved (cf. footnote h in Table I).

The spectrum in Fig. 5(c) is in coincidence with the 618-keV transition, which connects the 5434-keV 9^-_3 and 4815-keV 8^-_2 states. The 1225-keV $7^-_3 \rightarrow 5^-_1$ connection can be clearly seen. Likewise, the 1587-keV transition is evident, which depopulates the 3191-keV 7^+_1 yrast state (Fig. 2), which in turn is fed by the 1625-keV transition (Fig. 4). The 1462-keV connection into the negative-parity 7^- yrast state

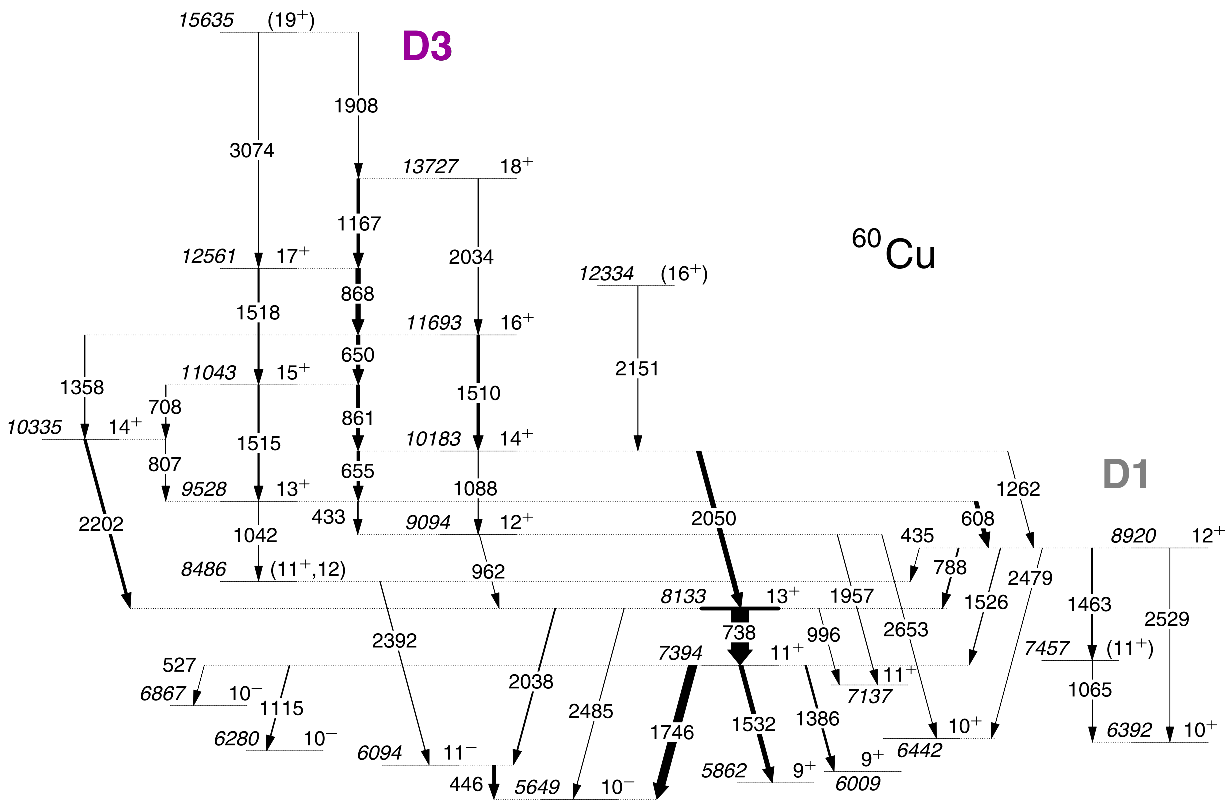

FIG. 6. Part of the level scheme of ^{60}Cu from the present study focusing on the dipole structure D3 (violet) and its decay paths into the lower-lying structures. The 8133-keV 13^+ yrast level is shown with a thicker line to guide the eye (cf. Fig. 2). Energy labels are in keV. The widths of the arrows correspond to the relative intensities of the γ rays.

is also prominent. In the case of the 4815-keV state, a total of nine decay paths are established, which account for all incoming flux.

The spectrum in Fig. 5(d) is in coincidence with the 253-keV $6_2^- \rightarrow 5_1^-$ transition located in the low-spin part of the level scheme (cf. lower left corner of Fig. 2). The spectrum clearly shows transitions at 972, 1100, 1498, and 1524 keV, which all feed the 3318-keV 6_2^- state from various states associated with D2. The spectrum also features the 2507-keV connection into the 557-keV 4^+ yrast state; its 270-, 454-, and 557-keV decays are present. The main transitions of D2 (cf. vertical dashed red lines) are present, too.

In-band dipole-transition mixing ratios $\delta(E2/M1) \approx +0.25$ are derived for the members at the bottom of D2, with a slightly decreasing trend toward $\delta(E2/M1) \approx +0.15$ for the higher-lying transitions [cf. Table I and Fig. 1(c)].

C. The dipole structure D3

Figure 6 focuses on another newly observed regular structure dominated by intense dipole transitions. Also, these are bypassed by stretched $E2$ transitions. Structure D3 covers an excitation energy range of about 9 to 16 MeV with spin-parity values from 12^+ to (19^+). The placement of D3 in the level scheme and its decay pattern, which proceeds predominantly through the 8133-keV 13^+ yrast state, is evinced by the selection of γ-ray spectra shown in Fig. 7.

The spectrum in Fig. 7(a) is in coincidence with the 2050-keV $14_1^+ \rightarrow 13_1^+$ transition, connecting the 10 183-keV state associated with D3 with the highlighted 8133-keV 13^+ yrast state. The relatively large DCO ratios of this transition indicate a $\Delta I = 1$ transition with a large positive mixing ratio (cf. Table I) and, thus, suggests 14^+ for the initial state. Besides the intense 738-keV transition, the subsequent decay paths from the corresponding 7394-keV 11_2^+ level (cf. Sec. IV A and Figs. 2 and 3), and a few contaminating lines arising from the nearby 2055-keV $9_1^+ \rightarrow 7_1^+$ transition (cf. Fig. 2), the spectrum shows the D3 dipole transitions at 650, 861, 868, 1167, and 1908 keV as well as the quadrupole transitions at 1510, 1518, 2034, and (in the inset) 3074 keV. Note that the 1908-keV transition is seen as a high-energy tail of the 1891-keV line, and the 2034-keV transition as a low-energy tail of the 2038-keV line. The latter is assigned $E3/M2$. It and the 2485-keV $E3$ transition mark weak decay branches of the 8133-keV 13^+ state, parallel to the main 738-keV path. The DCO ratios of the D3 in-band transitions determine the spins and parities of the structure. The only exception is the topmost level at 15635 keV, for which the assignment is tentative, i.e., based on the observed connections to both the 17^+ and 18^+ members of D3 as well as yrast arguments (cf. Sec. III).

Similar to the γ-ray spectra in Figs. 3(a) and 3(b), the remaining three spectra in Figs. 7(b)–7(d) are preselected by the requirement of a coincidence with the 738-keV $13_1^+ \rightarrow 11_2^+$ transition. For the spectrum in Fig. 7(b), another coincidence

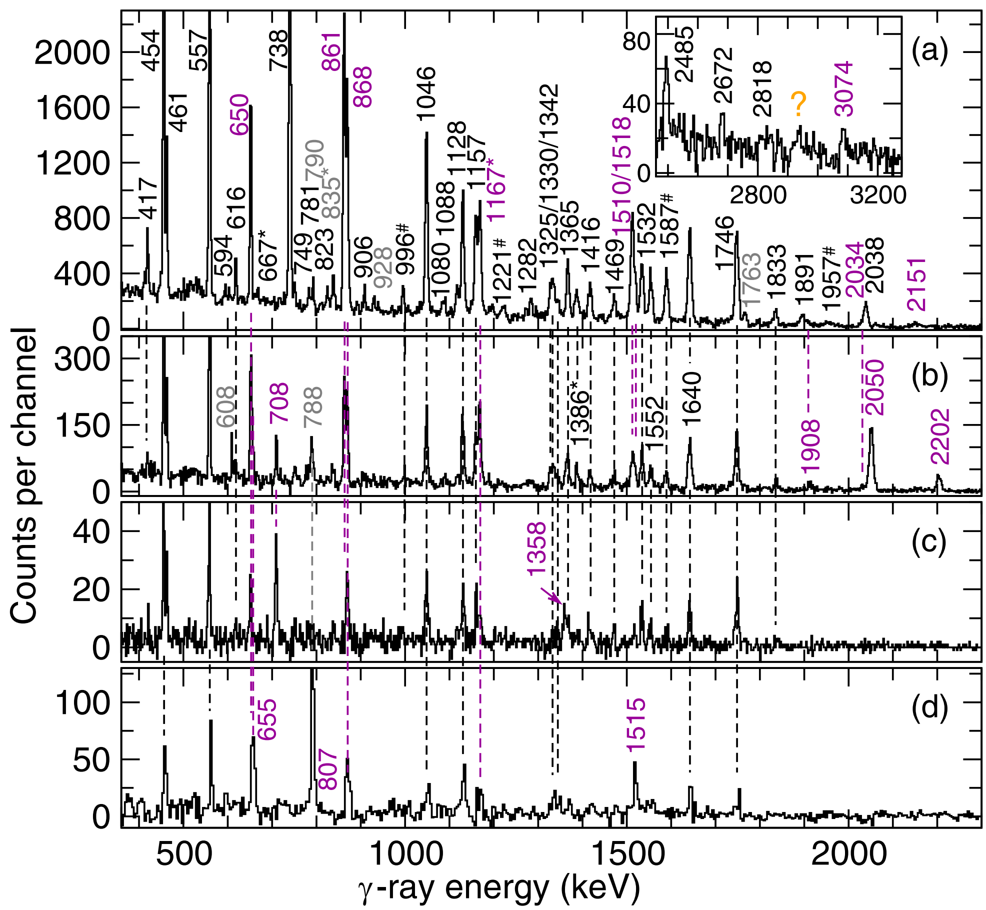

FIG. 7. Gamma-ray spectra from the $\gamma\gamma$ and $\gamma\gamma\gamma$ analysis of structure D3 of ^{60}Cu (cf. Fig. 6). Energy labels are in keV. They follow the color code outlined in the text. An asterisk indicates a peak doublet. Dashed vertical lines are to guide the eye. The spectrum in panel (a) is in coincidence with the 2050-keV $14_1^+ \rightarrow 13_1^+$ transition. A label with a hash (#) indicates increased statistics arising from coincidences with the 2055-keV $9_1^+ \rightarrow 7_1^+$ transition (cf. Fig. 2). The inset shows a part of the spectrum at higher energies: The peak at 3074 keV relates to the terminating $E2$ transition of D3 while the other three labeled γ rays reside in decay paths of the 8133-keV 13_1^+ state (cf. Fig. 2). The question mark indicates an unplaced transition. The spectra in panels (b)–(d) are in coincidence with the 738-keV $13_1^+ \rightarrow 11_2^+$ transition and an additional transition or set of transitions. These are, for panel (b), any of the 861-, 650-, or 868-keV transitions (all D3), for panel (c), the 2202-keV transition (D3), and, for panel (d), the 608-keV transition (D1). The spectra in panels (a)–(c) have a binning of 2 keV per channel, those in panel (d) and the inset of panel (a) have 4 keV per channel.

with any of the "D3-typical" 650-, 861-, or 868-keV dipole transitions is required. In addition to the already mentioned transitions associated with D3, the 708-2202-keV side branch becomes visible, giving rise to a second 14^+ state shown on the left-hand side of Fig. 6. In addition, the 608-655-788-keV path can be deduced, which includes the 8920-keV 12^+ state at the top of the D1 structure. Similar to the 2050-keV transition discussed earlier, also the 2202-keV transition reveals a distinct mixing ratio $\delta(E2/M1) \approx +1$.

The spectrum in Fig. 7(c) is in coincidence with the 2202-keV $14_2^+ \rightarrow 13_1^+$ transition. It thus highlights the 708- and 1358-keV transitions feeding this 14_2^+ state. Besides, it features the 650- and 868-keV transitions of the respective 650/655- and 861/868-keV doublets. The spectrum in Fig. 7(d) is in coincidence with the 608-keV transition connecting D1 with D3. The 788-keV connection between the 8920-keV (D1) and 8133-keV states is apparent, as are peaks representing the 655-, 807- (weak), and 1515-keV transitions populating the 9528-keV state of D3. In the case of D3, the mixing ratios of most of the in-band dipole transitions are moderately positive, but smaller than those measured for the dipole transitions within D2.

D. The high-spin quadrupole structures

At about 15 MeV excitation energy, collective band structures dominated by stretched quadrupole transitions become yrast. They are shown in Fig. 8, together with linking transitions to the previously discussed parts of the level scheme. The left-hand side of Fig. 8 presents, in addition, some weak dipole-type structures and their 2- to 3-MeV connections to the 9^-, 10^-, and 11^- yrast states.

Representative γ-ray spectra for the structures Q1 to Q4 are presented in Fig. 9. The spectrum in Fig. 9(a) is in coincidence with the 1919-keV $17_2^+ \rightarrow 15_2^+$ transition in Q2. The 3247-keV link to the 8133-keV 13_1^+ yrast state is prominent.

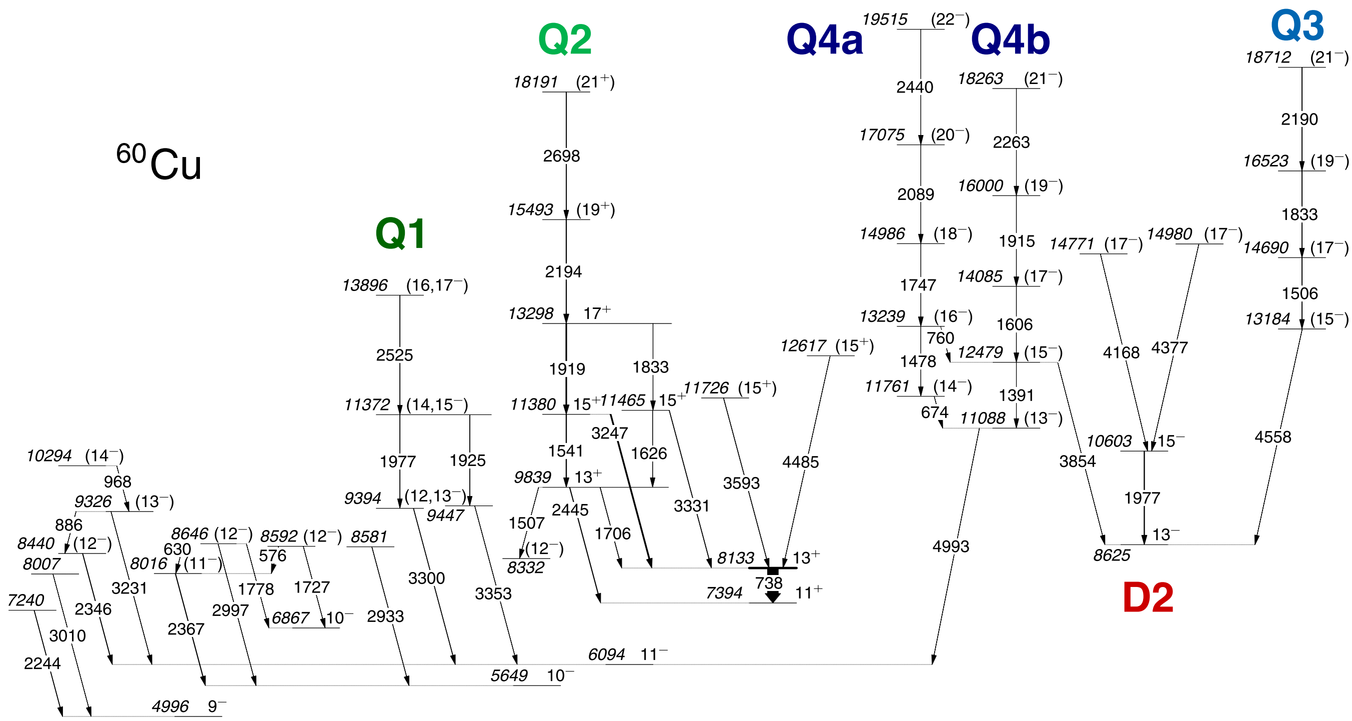

FIG. 8. Part of the level scheme of ^{60}Cu from the present study focusing on the quadrupole structures at high excitation energies and their decay paths into the lower-lying structures (cf. Figs. 2 and 4). Energy labels are in keV. The widths of the arrows correspond to the relative intensities of the γ rays. The spin-parity label (12, 13$^-$) at the bottom of band Q1 applies to both states at $E_x \approx 9.4$ MeV. The 8133-keV 13$^+$ yrast level is shown with a thicker line to guide the eye.

One can also clearly identify the higher-lying members of Q2 with 2194 and 2698 keV, the 1541–2445-keV decay branch of Q2, and some of the prominent low-spin transitions in ^{60}Cu. The 1606- and 2263-keV lines belong to sequence Q4b and occur in Fig. 9(a) because of the 1915-keV $19^-_1 \rightarrow 17^-_2$ transition there. The high-energy γ-ray spectra in Figs. 9(b) and 9(c) are in coincidence with the 738-keV $13^+_1 \rightarrow 11^+_2$ transition. Figure 9(b) is dominated by the 3247-keV Q2 linking transition. Here, one can also observe the 3331-keV linking transition and the 2698-keV transition at the top of Q2. Both Figs. 9(a) and 9(b) exhibit high-energy decays (2672, 2818, and 3152 keV) of the (8^+_5), 9^+_3, and 9^+_4 states at 5349, 5862, and 6009 keV (cf. Sec. IV A), the topmost transition of D3 with 3074 keV (cf. Sec. IV C), as well as transitions of 3593 and 4485 keV. The yields of the latter two are too small to unambiguously identify transitions feeding their respective initial levels at 11 726 and 12 617 keV.

The high-energy γ-ray spectra in Figs. 9(d) and 9(e) are in coincidence with the 446-keV yrast transition, which connects the 6094-keV 11^-_1 and 5649-keV 10^-_1 states. These are included at the bottom of Fig. 8 for completeness. Figure 8(d) allows us to observe the 2346-keV line from the 8440-keV state (left-hand side of Fig. 8) and the 2392-keV transition which connects into D3 (cf. Fig. 6). The 2525-keV peak corresponds to the topmost transition of Q1, which is reached by the 3300- and 3353-keV transitions visible on the right-hand side of the spectrum. In this energy regime, the 3247-keV link from Q2 (see above) is also visible, despite the relatively weak connection between the 6094- and 8133-keV states. The peak at 3231 keV refers to a transition that is parallel to the previously mentioned 2346-keV line. In Fig. 8(e), a weak peak at 4993 keV is observed, which is found to represent a link from band Q4 (see below).

The spectrum in Fig. 9(f) is in coincidence with the 4558-keV transition linking Q3 with the dipole structure D2 [cf. Sec. IV B and Fig. 5(a)]. The three members of Q3 with 1506, 1833, and 2190 keV can be seen, in conjunction with the main dipole and quadrupole transitions below the 8625-keV 13$^-$ state in D2. The spectrum in Fig. 9(g) is in coincidence with the 4993-keV transition connecting Q4 with the 6094-keV 11^-_1 state [cf. Fig. 8(e)]. In addition to the most intense transitions of the low-spin negative-parity and ground-state yrast sequences, peaks representing both Q4 quadrupole cascades are observed: 1391, 1606, 1915, and 2263 keV, and 1478 and 1747 keV, respectively. Furthermore, dipole connections between Q4a and Q4b appear to be present at 674 and 760 keV.

For the 3300-keV Q1 linking transition, a DCO ratio is obtained, but its uncertainty is large. Therefore, the spin assignments to members of Q1 remain tentative. In this case, it is difficult to use yrast arguments to constrain the values further. In contrast, the DCO ratios of the 3247- and 3331-keV Q2 linking transitions are consistent with stretched $E2$ character, which defines spin and parity of the lower states of band Q2. Based on yrast arguments and anticipated quadrupole collectivity, tentative spin-parity assignments are suggested for the higher-lying members of Q2. With the same arguments, tentative spins and parities are proposed for the band members of both Q3 and Q4.

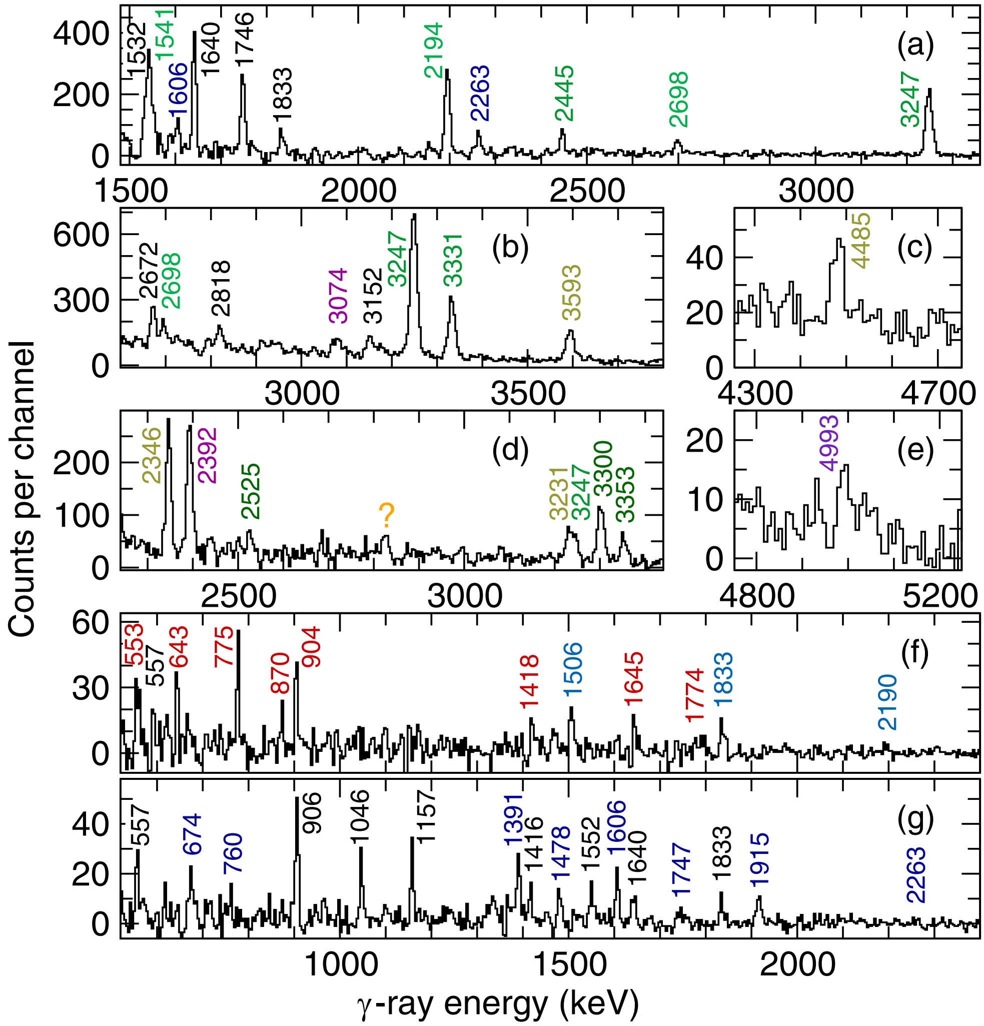

FIG. 9. Gamma-ray spectra from the $\gamma\gamma$ analysis of the quadrupole structures at high excitation energies in ^{60}Cu (cf. Fig. 8). Energy labels are in keV. They follow the color code outlined in the text. The spectrum in panel (a) is in coincidence with the 1919-keV $17_2^+ \rightarrow 15_2^+$ transition (Q2). Transitions from structure Q4b are also present due to a coincidence with the 1915-keV $19_1^- \rightarrow 17_2^-$ transition in that sequence. The spectra in panels (b) and (c) are in coincidence with the 738-keV $13_1^+ \rightarrow 11_2^+$ yrast transition. The spectra in panels (d) and (e) are in coincidence with the 446-keV $11_1^- \rightarrow 10_1^-$ yrast transition. The question mark in panel (d) indicates a transition that could not be placed in the level scheme. The spectrum in panel (f) is in coincidence with the 4558-keV transition linking Q3 into the dipole structure D2. The spectrum in panel (g) is in coincidence with the 4993-keV transition linking Q4 to the 11_1^- yrast state at 6094 keV [cf. panels (d) and (e)]. The binning of the spectra in panels (c) and (e) is 8 keV per channel, and of all other spectra 4 keV per channel.

The choices for (tentative) spin assignments are investigated further with Fig. 10. Relative yields as a function of excitation energy, E_x, for the dipole and quadrupole cascades as well as all other observed γ rays are shown. The latter include the transitions connecting the various collective bands with the lower-lying states. The suggested initial and final spin values for D2, D3, as well as Q1–Q4 are included in the figure. At the highest excitation energies, $E_x \approx$ 18–19 MeV, and spins $I \gtrsim 20$, Q2, Q3, and Q4 essentially share the yrast line. Among the quadrupole bands, the yrast line gradually shifts toward Q2 at about spin $I = 17$ at $E_x \approx$ 13–14 MeV. However, on an absolute scale, D3 determines the yrast line at about these values of spin and excitation energy. At $E_x \approx 10$ MeV and $I \approx$ 13–14, i.e., where the curves of D2 and D3 cross in Fig. 10, D2 becomes yrast, but this is quickly challenged by the yrast states of the noncollective part of the decay scheme.

For Q1, the data points in Fig. 10 are labeled with the lower spin option, i.e., $I = 12, 14, 16$ for the states belonging to the band. In fact, for the other, higher spin option $I = 13, 15, 17$, a larger overall yield would be expected due to yrast arguments, as outlined at the end of Sec. III. From this point of view, $I = 12, 14, 16$ is the slightly favored choice.

V. DISCUSSION

The overall scope of the high-spin level scheme of ^{60}Cu is similar to other comprehensive decay schemes derived for nuclei in the vicinity of doubly magic ^{56}Ni: at low excitation energy and spin, a rather irregular pattern is observed, which calls for an interpretation in the framework of the spherical shell model. These calculations and predictions are the subject of Sec. V A, including a brief case study of the mirror nucleus

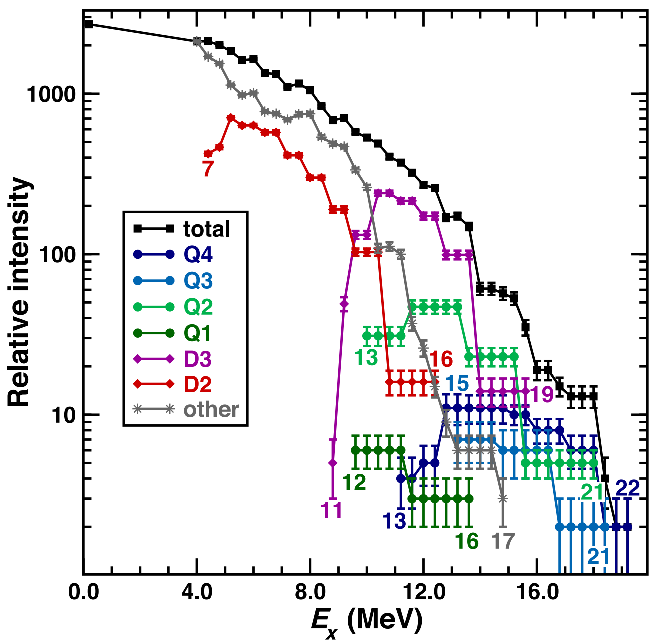

FIG. 10. Relative yields as a function of excitation energy, E_x, for the various dipole and quadrupole cascades as well as all other observed γ rays (dark gray). The color code outlined in the text is applied for Q1–Q4 and D2, D3. The total relative yield is indicated by the black line connecting the filled squares. The numbers correspond to the lowest and highest spin value attributed to a given cascade. For Q1, the option $I = 12, 14, 16$ has been chosen for this figure, rather than the alternative $I = 13, 15, 17$ (see text and Table I).

^{60}Ga. The collective structures are compared with predictions of cranked Nilsson-Strutinsky calculations in Sec. V B.

A. Shell-model calculations

1. Model spaces and parameters

For all shell-model calculations, the computer code ANTOINE [36,37] was used. All shell-model results refer to fully diagonalized calculations. With $Z = 29$ and $N = 31$, the low-spin level scheme of ^{60}Cu is expected to first exploit particles in the upper-fp shell comprising the $f_{5/2}$, $p_{3/2}$, and $p_{1/2}$ orbitals. Additional angular momentum can be generated by either creating holes in the high-j $f_{7/2}$ orbital, which dominates the low-spin nuclear structure between ^{40}Ca and ^{56}Ni, or by moving particles into the high-j, positive-parity $g_{9/2}$ intruder orbital. For shell-model practitioners, the first option is to explore the fp model space for low-lying positive-parity states in ^{60}Cu (cf. central and right part of Fig. 2 up to about $E_x = 5$ MeV), and the $f_{5/2}pg_{9/2}$ space for medium-spin negative-parity states (cf. left-hand side of Fig. 2) and the higher-lying positive-parity states in Fig. 2. A shell-model interaction involving both holes in $f_{7/2}$ and particles in $g_{9/2}$ is, to our knowledge, not available. Nevertheless, these particle-hole excitations quickly evolve into collective structures (see, e.g., Ref. [3]) and, thus, are covered by the calculations described and assessed in Sec. V B.

For the fp space, shell-model calculations are based on the commonly used GXPF1A [38] and KB3G [39,40] interactions. In the notation of Refs. [19,41], the KB3G56 interaction rather than the original KB3G interaction is used for this study. The difference is a reduced gap size at particle numbers $N = Z = 28$ (300 keV), and isospin-breaking terms were incorporated according to the descriptions in, e.g., Refs. [41,42], which build on the concepts outlined in Ref. [43]. Furthermore, an empirical isotensor isospin-nonconserving interaction was taken into account [44,45].

For mass $A = 60$ nuclei, it is challenging to conduct unrestricted calculations in the full fp model space. For the yrast line, a truncation scheme allowing for an excitation of up to six nucleons from the $f_{7/2}$ shell into the upper fp shell is implemented, commonly denoted as $t = 6$. For the observed multitude of states with the same spin and parity, calculations had to be restricted to $t = 4$.

Unrestricted calculations in the $f_{5/2}pg_{9/2}$ space use the JUN45 interaction [46], which has recently been extended to also include isospin-breaking terms along the same lines mentioned earlier (see Supplemental Material to Ref. [7] for details).

Electromagnetic decay properties are derived using bare g factors for $M1$ transitions for the two fp space interactions, while the g factors are modified by a quenching factor of 0.7 for g_s for use with the JUN45 interaction [46]. Furthermore, two sets of $E2$ effective charges are used: set A, $\varepsilon_p = 1.15e$ and $\varepsilon_n = 0.80e$ for protons and neutrons, respectively [47], as well as set B, $\varepsilon_p = 1.33e$ and $\varepsilon_n = 0.45e$ for protons and neutrons, respectively, according to a recent comprehensive survey and evaluation across the *sd* and fp shells [48]. Because of limitations of the model space and the available version of the shell-model code, strengths of parity-changing transitions are set to $B(E1) = 10^{-5}$ W.u., $B(M2) = 0.01$ W.u., and $B(E3) = 1$ W.u., respectively. These choices provide good agreement with, e.g., observed branching ratios (see discussion below). Experimental γ-ray energies are used to compute branching and mixing ratios of the transitions, as well as lifetimes of the nuclear states.

2. Results for ^{60}Cu

A comparison between experimental and predicted yrast energies for the low- to medium-spin states (cf. Fig. 2) is presented in Fig. 11. On the left-hand side, the evolution of predictions using truncation schemes of $t = 4$, $t = 5$, and $t = 6$, exemplified for the GXPF1A calculations in the fp space, indicates that convergence at $t = 6$ is sufficient. This is in line with many earlier shell-model studies in the mass region. Except for the slightly overpredicted split between the 1^+ and 2^+ levels and an underpredicted 12^+ state, the energy levels near the yrast line calculated with the GXPF1A interaction are in excellent agreement with the observed ones. This is underlined by a mean-level deviation (MLD) of only 94 keV for a binding-energy shift (BES) of -150 keV for the twelve states shown on the left-hand side of Fig. 11. For the same set of states, the values are MLD = 314 keV and BES = 10 keV for the calculation with the KB3G56 interaction. Here, the order of the spin $I \leqslant 4$ states is not correctly reproduced, the energies of the $I = 5$–8 levels are consistently underpredicted, and the $I = 9$–12 levels, in turn, are too high in energy. Note

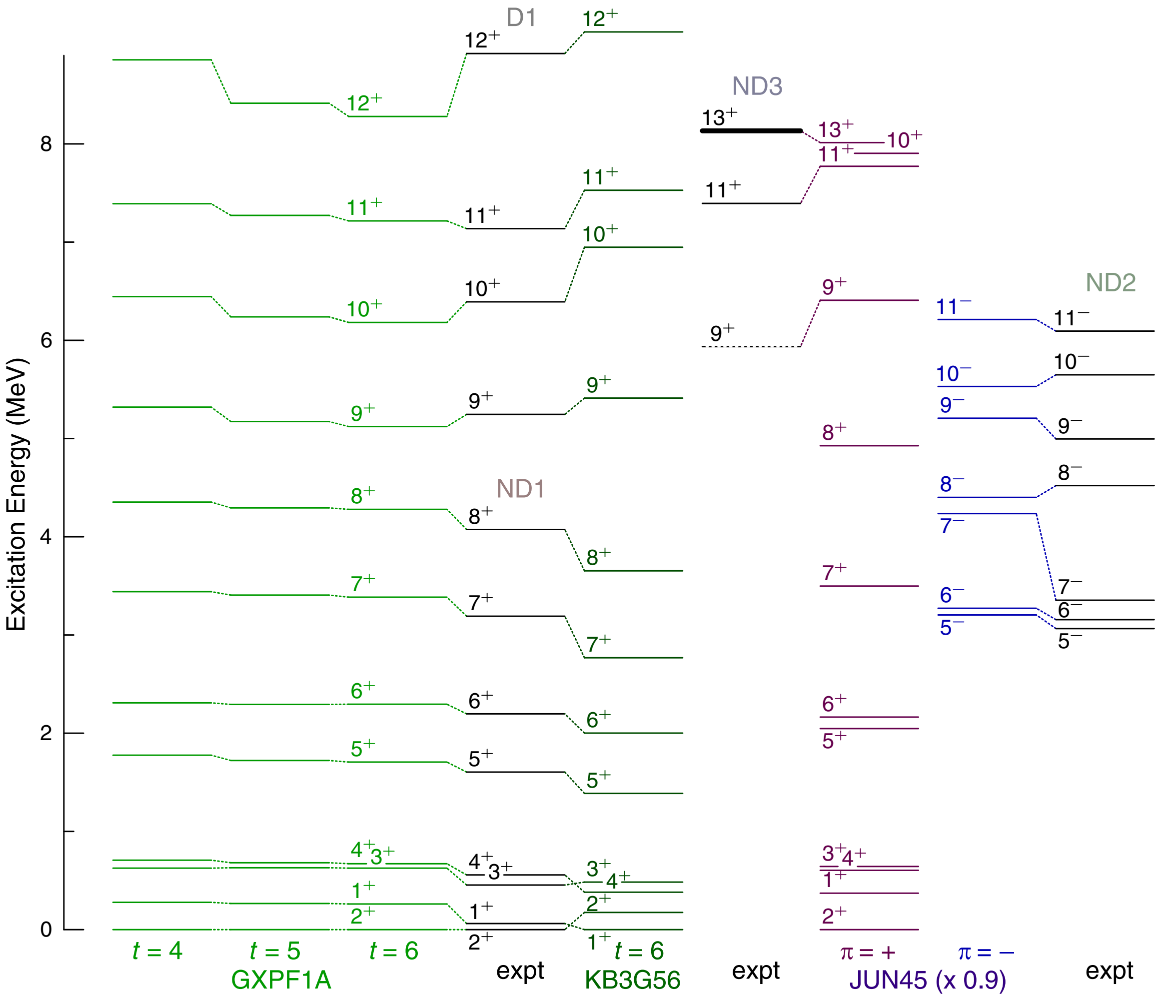

FIG. 11. Experimental (expt) and predicted yrast levels concerning the low-spin part of ^{60}Cu (see Fig. 2). The type of shell-model interaction, or truncation scheme, is placed underneath each set of states. The energies predicted with the JUN45 interaction are scaled by a factor of 0.9 to roughly align its calculated 13^+ level with the observed one at 8133 keV. This column of experimental odd-spin states includes a 9^+ level (dotted line) that is placed at the mean energy of the observed 9^+_3 and 9^+_4 states. The labels "ND1", "ND2", "ND3", and "D1" are indicative for parts of structures compared with cranked Nilsson-Strutinsky calculations in Sec. V B. See text for details.

that in the context of the cranked-Nilsson–Strutinsy (CNS) calculations (cf. Sec. V B), the present states are labeled ND1 ($I \leqslant 8$) and D1 ($8 < I \leqslant 12$).

None of the fp shell-model calculations is predicting a low-lying 13^+ state (labeled ND3). In fact, the 13^+ yrast state observed at 8133-keV excitation is best described by a combination of fully aligned $[\pi(g_{9/2}) \times \nu(g_{9/2})]_9 \times \nu(f_{5/2})^2_4$ and $[\pi(g_{9/2}) \times \nu(g_{9/2})]_9 \times [\nu(f_{5/2})\nu(p_{3/2}]_4$ configurations. Both rely on a strongly attractive $T = 0$, $J = 9$ two-body matrix element. Specifically, the wave function predicted by the JUN45 interaction suggests a 32% partition of the former and a 67% partition of the latter, as opposed to the third possibility, namely, another fully aligned configuration $[\pi(f_{5/2}) \times \nu(f_{5/2})]_5 \times \nu(g_{9/2})^2_8$, which is predicted to dominate the yrare 13^+ state (97%). The cranked Nilsson-Strutinsky calculations of Sec. V B predict this "favored-termination" state as well.

With summed partitions of 95% and 98%, the yrast 9^+ and 11^+ states predicted by the JUN45 interaction also rely on this fully aligned $T = 0, J = 9$ proton-neutron pair in the $g_{9/2}$ orbital, accompanied by various combinations of couplings of the remaining two neutrons in the upper fp shell. The predicted 11^+ state corresponds to the 7394-keV 11^+_2 level, which has two relatively intense $E2$ branches feeding the 9^+_3 and 9^+_4 states at 5862 and 6009 keV (see Fig. 2). Therefore, it is reasonable to associate one or both of these observed non-yrast 9^+ states with predicted states involving $T = 0$, $J = 9$ proton-neutron pairs. Recall that $f_{7/2}$-hole configurations can also play a role, which, however, lie outside the JUN45 model space.

The calculated energies of the 1^+–4^+ multiplet for JUN45 are in similar agreement with experiment as those obtained for the two fp interactions. The gap to the yrast 5^+ state, however, is larger for JUN45, while the predicted 6^+ energy is comparable with the other calculations and in line with experiment. The 7^+ and 8^+ energies for JUN45 are once again too high. These deviations can be traced to particle-hole excitations across the shell gaps at particle number 28.

For instance, JUN45 prefers (99% partition) the fully aligned $[\pi(f_{5/2}) \times \nu(f_{5/2})^2_4 \times \nu(p_{3/2})]_8$ configuration, which is predicted to contribute only 18% to the wave function of the yrast 8^+ state in case of GXPF1A. Similarly, closed-core partitions sum up to only 20% and 27% for the yrast 7^+ and 5^+ states, compared with ≈40% for the other low-lying states. It is important to recall that ^{56}Ni is a ‘soft’ doubly magic core, the ground state of which has been predicted to comprise only 40-50% closed-core configurations (see, e.g., Ref. [49] and references therein). Clearly, calculations with JUN45 cannot account for the aforementioned particle-hole correlations. This is also a justification for scaling the predicted energies by 0.9; there are only four valence nucleons at hand for ^{60}Cu.

A comparison of the excitation energies of the 5^- to 11^- yrast states with scaled results of JUN45 predictions is shown on the right-hand side of Fig. 11. First, all these predicted states have leading configurations and occupation numbers that are dominated by partitions with a single neutron in the $g_{9/2}$ orbital. Second, with the exception of the 7^- state, experimental and theoretical energies align very well, given the boundary conditions mentioned earlier. The wave function of this particular 7^- state involves 51% of the fully aligned, seniority $v = 2$ $[\pi(f_{5/2}) \times \nu(g_{9/2})]_7$ configuration. Hence, the above deviation seems primarily related to that two-body matrix element. In fact, a quick test with that two-body matrix element (TBME) set to be more attractive by 1 MeV shows a reduction of the energy difference between the predicted 6^-_1 and 7^-_1 states from 1.1 to 0.6 MeV. It is worth mentioning that the authors of Ref. [46] are concerned that “the present f_5pg_9 model space cannot be a good basis for the ‘unified model’” and that further work needs to be done, including the provision and consideration of additional experimental constraints.

With the exception of the 62-keV 1^+_1 level, which has a measured half-life of 2.0(1) ns [20], no excited-state lifetimes are known in ^{60}Cu. Thus, assessments of electromagnetic decay properties have to rely on branching ratios b and mixing ratios $\delta(E2/M1)$. Tables II–IV provide comparisons between selected experimental values and various theoretical predictions. In addition, Tables II and III also provide lifetime predictions. Note that, for a few non-yrast states, which are predicted to be close in excitation energy, the association with experimental levels is reordered based on an improved description of their decay and feeding patterns. This refers to reduced values of mean branching deviations (MBDs), which can be used to assess the level of agreement between calculated and observed branching ratios [50].

For the ten positive-parity yrast states ($I = 3$–12), MBD = 0.089(11) and 0.092(12) for the columns labeled GXPF1A ε_{eff}-A and -B, respectively, i.e., there is no significant difference in the predictions using different effective charges. Furthermore, the description of these states is only slightly worse for the KB3G56 interaction with MBD = 0.105(13). For the relevant subset of low-lying positive-parity states and including predictions for the negative-parity yrast states, MBD = 0.090(9) for JUN45 predictions, which is comparable in size, too. Notably, all values are significantly worse than descriptions of yrast states in slightly lighter nuclei, the structure of which is dominated by holes in the $f_{7/2}$ orbital rather than particles in the upper fp shell (see, e.g., Table III in Ref. [42] or Table III in Ref. [51]). Including non-yrast states (cf. Table II), MBD values for low-lying states in ^{60}Cu remain essentially the same for GXPF1A predictions [MBD = 0.083(6)] but worsen significantly for the calculation based on the KB3G interaction [MBD = 0.17(1)]. Thus, the GXPF1A interaction appears to be a reasonable but far from optimal choice to address shell-model states in $N \approx Z$, $A \gtrsim 60$ nuclei. Note that this conclusion is very much in line with the discussion of excited states in ^{63}Ga (see Tables III and IV in Ref. [19]). In view of Ref. [46] quoted earlier, JUN45 predictions for non-yrast states of ^{60}Cu are to some extent premature, not the least given the few valence particles available outside the, in this case, closed ^{56}Ni core.

The above conclusions will be illustrated with a few examples. Starting with the well-established low-lying 1^+ to 4^+ states, $E_x \lesssim 1$ MeV, the lifetime predictions of the 1^+_1 state range from $\tau = 0.2$ ns (KB3G56) to $\tau = 34$ ns (GXPF1A), with the experimental value lying in between [20]. Similarly, there is a spread in predictions of about one to two orders of magnitude for the lifetimes of the 2^+_2, 3^+_1, and 4^+_1 levels. Clearly, lifetime measurements would provide an additional tool to help constrain the underlying shell-model interaction. Nevertheless, already the largely varying predicted branching ratios for, e.g., the 2^+_2 and 4^+_1 states yield relevant information: the GXPF1A predictions are in line with experiment for the 2^+_2 level, but completely miss the 104-keV branch from the 4^+_1 level. The KB3G56 predictions, on the other hand, fail to describe the decay paths of the 2^+_2 level, while they are close to experiment for the 4^+_1 level. Such unusually large variations clearly indicate that the two-body matrix elements among the orbitals in the upper-fp shell are far from established. Interestingly, for these few low-lying levels, JUN45 provides the overall best agreement between experimental and predicted branching ratios.

The situation is somewhat better for the 1604-keV 5^+_1 and 2197-keV 6^+_1 yrast states, for which all predictions are comparable and in good agreement with experiment. However, the agreement among predictions and experiment worsens again for non-yrast and the higher-lying yrast states. For some of these, even the main observed branches are occasionally missed: in case of KB3G56, the 2055-keV $9^+_1 \to 7^+_1$, the 925-keV $10^+_1 \to 9^+_2$, or the 1811-keV $10^+_1 \to 8^+_2$ transitions, or in the case of GXPF1A, the 1463-keV $12^+_1 \to (11^+_3)$ transition. Still, the observed decay pattern of the very same 7457-keV (11^+_3) level is nicely described by the calculation with the GXPF1A interaction. Note that the predicted lifetimes are $\tau \lesssim 1$ ps for all states with $E_x \gtrsim 2.5$ MeV and $I \gtrsim 6\hbar$ (described within the fp model space).

As stated in the discussion of Fig. 11, the observed 7394-keV 11^+_2 and 8133-keV 13^+_1 states (Fig. 2) are connected with configurations that involve two particles in the $g_{9/2}$ orbital, i.e., they fall outside the fp model space of GXPF1A and KB3G56. In fact, the lifetime prediction using the JUN45 interaction for these states (provided at the end of Table III) suggests $\tau \approx 0.1$–0.4 ns for the fully aligned, seniority $v = 4$ 13^+_1 state. Here, a final note on the branching ratios seems in order. First, the predictions strongly depend on the effective charges used. Second, the values are well in line with the

TABLE II. Selection of experimental (Table I and Ref. [20]) and predicted branching ratios of low-spin positive-parity states in ^{60}Cu (cf. Fig. 2). Predictions of two sets "A" and "B" of effective charges are explored for the GXPF1A interaction (cf. text for details). In the first row of a given state, predicted excited-state lifetimes τ (ps) are provided (in italic). In the JUN45 column, states without any reasonable match are labeled "*n.m.*" (see also corresponding footnotes). Energies of unobserved γ-ray transitions are listed in italic characters and the branching ratio is labeled "n.o."

E_x (keV)	E_γ (keV)	I_i^π ($\hbar$)	I_f^π ($\hbar$)	$b_{\rm expt}$ (%)	GXPF1A $\varepsilon_{\rm eff}$-A	GXPF1A $\varepsilon_{\rm eff}$-B	KB3G56 $\varepsilon_{\rm eff}$-B	JUN45 $\varepsilon_{\rm eff}$-B
62		1_1^+			*34000*	*34000*	*220*	*350*
287		2_2^+			*9.0*	*9.0*	*470*	*6.7*
	225		1_1^+	75.0(19)	71.7	71.7	0.2	48.8
	287		2_1^+	25.0(19)	28.3	28.3	99.8	51.2
365		1_2^+			*6.0*	*6.0*	*49*	*1.9*
	303		1_1^+	n.o.	10.4	10.4	6.5	1.9
	365		2_1^+	100	89.4	89.5	92.2	96.6
454		3_1^+			*3.6*	*3.6*	*16*	*1.7*
	167		2_2^+	2.3(3)	1.2	1.2	18.2	0.8
	391		1_1^+	0.3(1)	0.1	0.1	1.6	0.0
	454		2_1^+	97.4(4)	98.6	98.7	80.2	99.2
557		4_1^+			*550*	*770*	*62*	*580*
	104		3_1^+	37.3(17)	0.1	0.1	63.3	25.4
	270		2_2^+	10.5(7)	12.5	12.9	0.0	3.1
	557		2_1^+	52.1(18)	87.4	87.0	36.7	71.5
781		3_2^+			*0.90*	*0.91*	*1.1*	*1.9*
	224		4_1^+	14.8(41)	0.1	0.1	5.5	43.3
	327		3_1^+	22.2(36)	2.6	2.6	7.5	1.9
	494		2_2^+	n.o.	4.4	4.4	86	2.5
	781		2_1^+	63.0(56)	92.4	92.5	0.5	50.4
1421		4_2^+			*0.97*	*1.2*	*0.28*	*0.42*
	863		4_1^+	18.1(34)	4.6	5.5	55.3	43.4
	967		3_1^+	27.5(40)	27.1	30.2	34.5	48.8
	1134		2_2^+	31.9(45)	19.4	17.6	1.0	1.2
	1421		2_1^+	22.5(40)	48.9	46.7	0.0	0.9
1505		4_3^+			*8.1*	*9.4*	*1.0*	*2.8*
	724		3_2^+	12.5(24)	3.1	3.2	1.2	32.3
	948		4_1^+	n.o.	18.1	19.0	32.6	3.4
	1052		3_1^+	36.5(38)	36.9	37.6	61.8	62.6
	1218		2_2^+	n.o.	6.0	4.8	1.7	0.0
	1506		2_1^+	51.0(43)	35.3	34.6	2.7	1.7
1604		5_1^+			*2.4*	*3.1*	*2.1*	*1.1*
	823		3_2^+	7.5(7)	14.7	14.2	1.0	0.2
	1046		4_1^+	90.0(11)	48.1	48.8	70.3	93.4
	1150		3_1^+	2.5(5)	36.7	36.3	27.9	4.9
1779		5_2^+			*2.3*	*2.5*	*2.0*	*0.83*
	274		4_3^+	n.o.	0.8	0.8	17.5	5.2
	358		4_2^+	10.8(15)	3.6	3.9	28.9	0.8
	877		3_3^+	n.o.	12.2	11.3	5.7	1.0
	1221		4_1^+	35.1(20)	51.3	56.3	32.8	92.4
	1325		3_1^+	54.1(24)	31.0	26.6	3.1	0.1
2027		5_3^+			*0.53*	*0.56*	*0.52*	*1.5*
	248		5_2^+	2.3(5)	0.1	0.1	0.0	0.8
	423		5_1^+	0.8(4)	2.9	3.1	1.0	0.8
	605		4_2^+	8.9(11)	18.5	19.4	6.0	0.5
	1246		3_2^+	n.o.	2.9	2.2	4.4	27.7
	1469		4_1^+	79.5(28)	58.1	60.7	71.3	64.1
	1573		3_1^+	8.5(14)	16.3	13.4	15.9	0.5

TABLE II. (*Continued.*)

E_x (keV)	E_γ (keV)	I_i^π ($\hbar$)	I_f^π ($\hbar$)	b_{expt} (%)	GXPF1A ε_{eff}-A	GXPF1A ε_{eff}-B	KB3G56 ε_{eff}-B	JUN45 ε_{eff}-B
2197		6_1^+			*0.52*	*0.73*	*0.86*	*1.4*
	594		5_1^+	3.1(4)	1.1	1.6	6.8	12.3
	1640		4_1^+	96.9(4)	97.4	96.7	92.7	74.2
2692[a]		6_2^+			*0.73*	*0.81*	*0.64*	*0.45*
	665		5_3^+	2.0(7)	1.9	1.9	0.0	0.3
	913		5_2^+	n.o.	21.5	22.3	3.9	36.6
	1088		5_1^+	48.2(21)	35.1	38.4	55.4	49.3
	1186		4_3^+	31.9(18)	0.4	0.4	7.0	0.0
	1271		4_2^+	17.9(14)	10.0	8.4	26.9	4.2
	2135		4_1^+	n.o.	23.9	21.6	4.8	0.9
2817[a,b]		6_3^+			*0.40*	*0.42*	*1.7*	*1.5*
	466		5_5^+	3.3(10)	6.8	7.1	4.5	0.0
	529		5_4^+	1.6(9)	10.7	11.2	11.0	0.0
	620		6_1^+	4.1(10)	0.3	0.3	7.6	1.5
	790		5_3^+	59.8(46)	23.3	24.4	32.6	18.9
	1038		5_2^+	13.8(20)	0.9	0.9	1.3	18.5
	1213		5_1^+	8.5(17)	40.2	40.0	25.4	11.1
	1312		4_3^+	n.o.	7.3	7.2	0.1	46.3
	1396		4_2^+	8.9(17)	10.2	8.7	0.9	0.1
3191		7_1^+			*0.35*	*0.45*	*0.88*	*n.m.*[c]
	499		6_2^+	4.9(9)	0.0	0.0	3.9	
	994		6_1^+	13.0(13)	3.3	4.0	24.9	
	1412		5_2^+	15.4(13)	1.9	2.0	0.4	
	1587		5_1^+	66.7(23)	91.8	90.2	62.2	
3372[a]		7_2^+			*0.24*	*0.26*	*0.39*	*n.m.*[c]
	680		6_2^+	n.o.	7.0	7.5	23.7	
	1175		6_1^+	23.5(32)	69.1	74.0	15.3	
	1593		5_2^+	48.7(41)	20.5	16.1	48.8	
	1768		5_1^+	27.7(33)	1.8	0.9	0.2	
3745[a]		7_3^+			*0.29*	*0.32*	*0.35*	*0.09*
	806		6_4^+	7.1(14)	0.1	0.1	7.5	
	928		6_3^+	52.0(40)	36.9	40.4	43.3	67.4
	1053		6_2^+	n.o.	11.4	12.3	21.2	1.5
	1395		5_5^+	5.6(13)	9.5	9.1	0.0	
	1457		5_4^+	n.o.	23.7	20.9	12.9	
	1548		6_1^+	18.7(27)	5.2	5.7	2.9	14.7
	1718		5_3^+	16.7(22)	0.2	0.0	0.4	0.0
	1966		5_2^+	n.o.	9.1	6.6	0.6	5.5
4074		8_1^+			*0.66*	*0.81*	*0.64*	*n.m.*
	703		7_2^+	15.1(20)	20.5	25.3	2.2	
	883		7_1^+	n.o.	4.4	5.1	49.7	
	1257		6_3^+	n.o.	25.0	25.8	0.2	
	1382		6_2^+	84.9(20)	31.4	27.0	44.1	
	1877		6_1^+	n.o.	14.9	12.8	0.2	
4580		8_2^+			*0.14*	*0.16*	*0.43*	*n.m.*
	506		8_1^+	5.4(13)	26.2	28.7	4.9	
	835		7_3^+	28.3(29)	18.8	20.4	1.4	4.7
	1389		7_1^+	9.8(25)	1.4	1.4	0.1	
	1763		6_3^+	56.5(41)	15.1	16.2	0.3	94.9
	1888		6_2^+	n.o.	35.6	30.6	0.1	0.4
4740		8_3^+			*0.21*	*0.24*	*2.4*	*n.m.*
	893		7_4^+	36(7)	4	5	36	
	995		7_3^+	n.o.	11	13	11	
	1529		6_5^+	32(7)	27	26	4	

TABLE II. (*Continued.*)

E_x (keV)	E_γ (keV)	I_i^π ($\hbar$)	I_f^π ($\hbar$)	$b_{\rm expt}$ (%)	GXPF1A $\varepsilon_{\rm eff}$-A	GXPF1A $\varepsilon_{\rm eff}$-B	KB3G56 $\varepsilon_{\rm eff}$-B	JUN45 $\varepsilon_{\rm eff}$-B
	1549		7_1^+	n.o.	11	12	8	
	1801		6_4^+	32(7)	19	18	0	
	2543		6_1^+	n.o.	12	11	27	
5246		9_1^+			*0.17*	*0.19*	*0.32*	*n.m.*
	666		8_2^+	16.7(21)	28.9	31.8	51.2	
	1173		8_1^+	8.6(20)	6.4	6.7	17.7	
	1400		7_4^+	9.7(16)	0.1	0.2	29.8	
	1501		7_3^+	17.7(25)	22.2	20.5	0.5	
	1875		7_2^+	14.0(23)	25.7	23.0	0.2	
	2055		7_1^+	33.3(36)	16.2	17.3	0.1	
5467[a,b]		9_2^+			*0.38*	*0.46*	*1.1*	*n.m.*
	727		8_3^+	3(2)	2	2	3	
	886		8_2^+	27(6)	24	28	76	
	1393		8_1^+	n.o.	13	15	9	
	1620		7_4^+	28(6)	44	40	2	
	1722		7_3^+	22(4)	0	0	0	
	2095		7_2^+	20(4)	17	14	4	
6392[b]		10_1^+			*0.13*	*0.14*	*0.18*	*n.m.*
	925		9_2^+	27(7)	28	30	1	
	1145		9_1^+	26(7)	32	33	18	
	1652		8_3^+	n.o.	10	9	24	
	1812		8_2^+	34(7)	19	18	0	
	2318		8_1^+	13(6)	8	8	0	
6442[b]		10_2^+			*0.09*	*0.10*	*0.06*	*n.m.*
	1196		9_1^+	54(8)	57	61	75	
	1862		8_2^+	46(8)	17	15	21	
	2368		8_1^+	n.o.	17	15	1	
6634		10_3^+			*0.13*	*0.15*	*0.65*	*n.m.*
	1894		8_3^+	100	46	43	40	
7137		11_1^+			*0.17*	*0.21*	*0.22*	*n.m.*
	695		10_2^+	n.o.	12	14	37	
	1670		9_2^+	n.o.	34	33	1	
	1891		9_1^+	100	48	45	59	
7457[d]		11_3^+			*0.06*	*0.07*	*0.08*	*n.m.*
	1065		10_1^+	54(18)	41	45	64	
	2211		9_1^+	46(18)	30	27	1	
8920[d]		12_1^+			*0.09*	*0.10*	*0.03*	*n.m.*
	1293		11_4^+	n.o.	17	17	5	
	1463		11_3^+	78(9)	5	5	49	
	1783		11_1^+	n.o.	2	2	16	
	2286		10_3^+	n.o.	27	26	1	
	2479		10_2^+	12(5)	11	11	13	
	2529		10_1^+	10(5)	39	38	16	

[a]For the calculation with the GXPF1A interaction, the predicted 6_2^+ and 6_3^+, 7_2^+ and 7_3^+, and 9_2^+ and 9_3^+ states are interchanged. See text for details.
[b]For the calculation with the KB3G56 interaction, the predicted 6_3^+ and 6_4^+, 9_2^+ and 9_3^+, and 10_1^+ and 10_2^+ states are interchanged. See text for details.
[c]The decay pattern of the calculated 7_1^+ yrast state matches favorably the experimental 7_3^+ state.
[d]The calculated 11_2^+ state is used and the experimental 7394-keV 11_2^+ and 8133-keV 13_1^+ states are ignored. See Table III and text for details.

observation that the lifetime of that state must exceed several picoseconds [21]. Third, with the set values for $B(M2)$ and $B(E3)$ strengths, the observed decay pattern of the 8133-keV state is very well described. To achieve a similar level of agreement between theory and experiment, including the measured $\delta(M2/E1)$ of the 1746-keV $11_2^+ \rightarrow 10_1^-$ transition, it is necessary to double the set $B(E1)$ strength (branching ratio) to 2×10^{-5} W.u., and to quadruple the $B(M2)$ strength (mixing ratio) to 0.04 W.u.

The measured and predicted branching and mixing ratios of transitions deexciting the yrast and a few closely lying yrare negative-parity states, as well as derived lifetimes of these

TABLE III. Selection of experimental (cf. Table I) and predicted branching ratios of medium-spin negative-parity states, as well as the 7394-keV 11^+_2 and 8133-keV 13^+_1 levels in ^{60}Cu (cf. Fig. 2). Predictions of two sets "A" and "B" of effective charges are explored for the JUN45 interaction (cf. text for details). In the first row of a given state, predicted excited-state lifetimes τ (ps) are provided (in italic). Energies of unobserved (n.o.) γ-ray transitions are listed in italic characters. The two rightmost columns provide measured and predicted mixing ratios.

E_x	E_γ			b_{expt}	b_{theo}			δ_{theo}
(keV)	(keV)	I^π_i ($\hbar$)	I^π_f ($\hbar$)	(%)	ε_{eff}-A	ε_{eff}-B	δ_{expt}	ε_{eff}-B
3065		5^-_1			*2.2*	*2.2*		
3156[a]		6^-_1			*6.4*	*6.4*		
3318[a]		6^-_2			*3.1*	*3.1*		
3354[b]		7^-_1			*9.1*	*9.1*		
	198		6^-_1	n.o.	3	3		
	662		6^+_2	n.o.	4	4		
	1157		6^+_1	100	89	89	$-0.11(^{5}_{7})$	-0.10
3772[c]		7^-_2			*0.73*	*0.73*		
	417		7^-_1	42(2)	63	63	$\|\delta\| > 1$	0.00
	616		6^-_1	41(2)	15	15	$-0.09(^{7}_{9})$	-0.01
	1080		6^+_2	13(2)	15	15	$-0.16(^{8}_{9})$	-0.16
	1575		6^+_1	4(1)	5	5		
4521		8^-_1			*0.06*	*0.06*		
	749		7^-_2	7(1)	1	1	$+0.3(2)$	-0.01
	1167		7^-_1	29(2)	97	98	$-0.17(^{7}_{11})$	$+0.02$
	1330		7^+_1	20(2)	0	0	$-0.01(10)$	-0.02
	1365		6^-_1	45(2)	0	0		
4996		9^-_1			*4.1*	*6.2*		
	475		8^-_1	n.o.	14	21		
	922		8^+_1	12(2)	5	8		
	1224		7^-_2	9(2)	45	38		
	1643		7^-_1	79(4)	35	32		
5188		9^-_2			*0.53*	*0.81*		
	667		8^-_1	5(1)	3	4		
	1114		8^+_1	3(1)	1	2		
	1416		7^-_2	53(2)	4	5		
	1833		7^-_1	39(2)	92	89		
5649		10^-_1			*1.4*	*1.5*		
	461		9^-_2	27(2)	80	86	$+0.10(^{5}_{6})$	0.00
	652		9^-_1	4(1)	0	0	$-0.06(^{8}_{11})$	$+0.16$
	1128		8^-_1	69(2)	20	14		
6094		11^-_1			*12*	*16*		
	446		10^-_1	33(3)	44	55	$-0.06(^{7}_{8})$	$+0.03$
	906		9^-_2	61(3)	55	44		
	1098		9^-_1	6(1)	1	1		
7394[d]		11^+_2			*2.1*	*3.3*		
	527		10^-_4	1(1)	1	1		
	1115		10^-_3	6(1)	5	7	$+0.01(12)$	0.00
	1386		9^+_4	12(1)	0	0		
	1532		9^+_3	28(2)	60	36		
	1746		10^-_1	54(3)	35	56	$-0.05(^{5}_{6})$	-0.04
8133		13^+_1			*130*	*350*		
	738		11^+_2	92(1)	97	93		
	2038		11^-_1	6(1)	2	5		
	2485		10^-_1	2(1)	1	3		

[a]The predicted 6^-_1 and 6^-_2 states are interchanged. See text for details.
[b]Using $B(M2) = 1.5$ W.u. and $B(E1) = 4 \times 10^{-5}$ W.u. for the 1157-keV transition.
[c]Using $B(M2) = 10$ W.u. and $B(E1) = 1 \times 10^{-4}$ W.u. for the 1080-keV transition.
[d]Using $B(M2) = 0.04$ W.u. and $B(E1) = 2 \times 10^{-5}$ W.u. for the 1746-keV transition.

TABLE IV. Selection of experimental (Table I) and predicted $\delta(E2/M1)$ mixing ratios of transitions connecting low-spin positive-parity states in ^{60}Cu (cf. Fig. 2).

E_x		E_γ	δ_{expt}	GXPF1A		KB3G56	JUN45
(keV)	I_i^π ($\hbar$)	(keV)	(%)	ε_{eff}-A	ε_{eff}-B	ε_{eff}-B	ε_{eff}-B
287	2_2^+	225	$+0.16(^5_6)$	+0.01	+0.01	−0.28	+0.01
454	3_1^+	454	$+0.03(^4_5)$	−0.13	−0.11	−0.08	−0.04
781	3_2^+	781	≈ -0.8	+0.12	+0.10	−0.38	−0.05
1505	4_3^+	1052	≈ -1.0	−0.81	−0.68	+0.08	−0.15
1604	5_1^+	1046	$-0.8(^3_5)$	+330	+290	−0.26	−0.09
1779	5_2^+	1221	$+0.11(^{11}_{13})$	−0.02	−0.06	−2.4	+0.08
2027	5_3^+	1469	$-0.14(^{10}_{17})$	−0.12	−0.10	−0.08	−0.25
2692	6_2^+	1088	−0.9(2)	−0.21	−0.19	−0.35	−0.11
2817	6_3^+	790	$+0.14(^6_7)$	+0.20	+0.19	−0.10	−0.12
3191	7_1^+	994	$-0.9(^4_6)$	+0.82	+0.75	+0.20	[a]
3745	7_3^+	928	$+0.22(^7_8)$	+0.33	+0.31	+0.15	[a]

[a]Unclear matching of observed and predicted states. See Table II.

states, are provided in Table III. First of all, the calculated values are comparable for the two sets of effective charges, i.e., none of the observables turns out to be particularly sensitive to those parameters for this set of negative-parity states in ^{60}Cu. To achieve agreement with the decay pattern of the 7_1^- and 7_2^- states, exchanging the predicted 6_1^- and 6_2^- levels turns out to be the favorable option in terms of MBD considerations. Furthermore, to reproduce the observed dominating 1157-keV $7_1^- \to 6_1^+$ branch and its measured nonzero $\delta(M2/E1)$ mixing ratio, considerably larger $B(E1) = 4 \times 10^{-5}$ W.u. and $B(M2) = 1.5$ W.u. strengths compared with the standard values are required. Even more drastic adjustments are needed to accommodate a sizable 1080-keV $7_2^- \to 6_2^+$ transition in the theoretical description. In fact, the predicted occupation numbers for the engaged states point at a large overlap between partitions involving $\nu(g_{9/2})$ and $\nu(f_{5/2})$ contributions in the initial and final states.

The predicted decay pattern of the yrast 8_1^-, 9_1^-, and 10_1^- states is dominated by strong $M1$ matrix elements, in tension with experiment, which calls for additional $E2$ decay strengths. The JUN45 calculation predicts such an $E2$ transition only for the 6094-keV 11_1^- state. Inspecting the decay pattern of the two closely lying yrast and yrare 9^- states reveals comparable MBD values when exchanging their assignments to the experimental counterparts. An additional two-state mixing approach could result in a nice theoretical description of both of them. The yrast 9_1^- state is predicted to be primarily composed of $[\pi(g_{9/2}) \times \nu(f_{5/2})]_7 \times \nu(p_{3/2})^2_2$ (22%) and $[\nu(g_{9/2}) \times \nu(f_{5/2})]_7 \times [\nu(p_{3/2}) \times \pi(p_{3/2})]$ (70%) partitions, i.e., mixed proton or neutron $g_{9/2}$ excitations. At variance, the yrare 9_2^- level is predicted to comprise mostly $[\pi(f_{5/2}) \times \nu(g_{9/2})]_7 \times \nu(fp)^2_2$ (≈80%) partitions but hardly any with proton $g_{9/2}$ occupancy.

Table IV compares measured and calculated $\delta(E2/M1)$ mixing ratios for a number of rather intense, stretched $\Delta I = 1$ transitions connecting low-lying positive-parity states (cf. Fig. 2). In general, the level of agreement between experiment and theory is similar to the description of the branching ratios (cf. Table II): On the one hand, there are cases of excellent agreement for predictions of all interactions explored (e.g., the 1469-keV $5_3^+ \to 4_1^+$ or 928-keV $7_3^+ \to 6_3^+$ transitions), a very good match with the prediction of at least one interaction [e.g., the 781-keV $3_2^+ \to 2_1^+$ (KB3G56), 790-keV $6_3^+ \to 5_3^+$ and 1052-keV $4_3^+ \to 4_1^+$ (both GXPF1A), or 1221-keV $5_2^+ \to 4_1^+$ (JUN45) transitions]. On the other hand, there is hardly any match because of either a wrong phase of one of the transition matrix elements (e.g., the 454-keV ground-state transition or the 994-keV $7_1^+ \to 6_1^+$ yrast transition) or an apparent large sensitivity on the exact amount of a tiny $B(M1)$ strength (see the 1046-keV $5_1^+ \to 4_1^+$ yrast transition). Ultimately, all these aspects can be related to uncertainties of the underlying upper-fp shell two-body matrix elements, a modification of which may lead to small changes in energy but possibly significant alterations of the electromagnetic decay pattern.

3. *The yrast line of* ^{60}Ga

The $T = 1$, $T_z = -1$ isotope ^{60}Ga is the neutron-deficient mirror nucleus of $T_z = +1$ ^{60}Cu, and ^{60}Ga is situated at the proton dripline. Based on decay experiments [20,52–54] and more recent mass measurements [55–57], Ref. [58] suggests a weakly bound 2^+ ground state of ^{60}Ga with $S_p = 88(15)$ keV and $T_{1/2} = 69.4(2)$ ms. Furthermore, a γ ray at 837 keV observed in the β^+/EC decay of ^{60}Ge has been tentatively associated with a $1^+ \to 2^+$ ground-state transition in ^{60}Ga [54].

The very low proton-separation energy implies that essentially all excited states of ^{60}Ga are subject to proton emission, i.e., decay energies, angular momenta, and spectroscopic factors have to be weighed against electromagnetic decay probabilities to assess whether the quasibound excited states of ^{60}Ga preferably decay by γ-ray emission into lower-lying states of ^{60}Ga, or by proton emission into states of ^{59}Zn [59].

The shell-model prediction of excited states along the yrast line of ^{60}Ga is based on the observed states in ^{60}Cu (cf. Table I) and calculated mirror energy differences (MED) between corresponding mirror states in ^{60}Ga and ^{60}Cu, respectively, using the isospin-breaking terms introduced earlier (cf. Sec. V A 1 and the Supplemental Material of Ref. [7]). Fig-

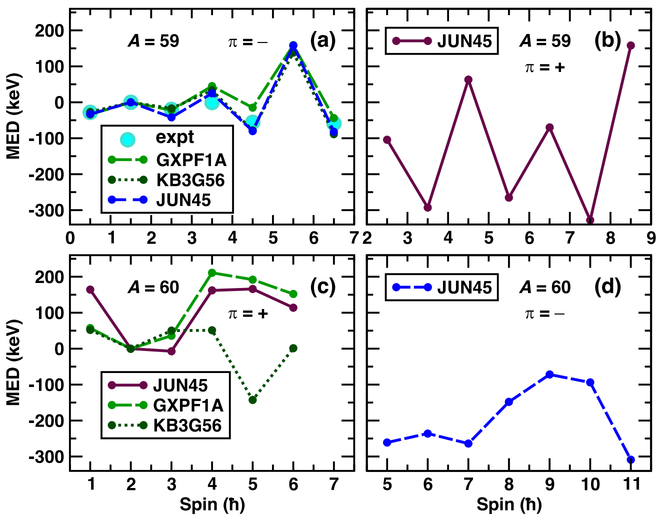

FIG. 12. Mirror-energy differences (MED) for the mass $A = 59$ pair ^{59}Zn - ^{59}Cu [panels (a) and (b)] and the mass $A = 60$ pair ^{60}Ga - ^{60}Cu [panels (c) and (d)]. Experimental data (only available for $A = 59$, $\pi = -$) as well as predictions using different shell-model interactions are shown for negative- and positive-parity states. Note that, for $A = 59$, $\pi = +$, as well as $A = 60$, $\pi = -$ states, configurations must engage at least one particle in the $g_{9/2}$ intruder orbital. See text for details.

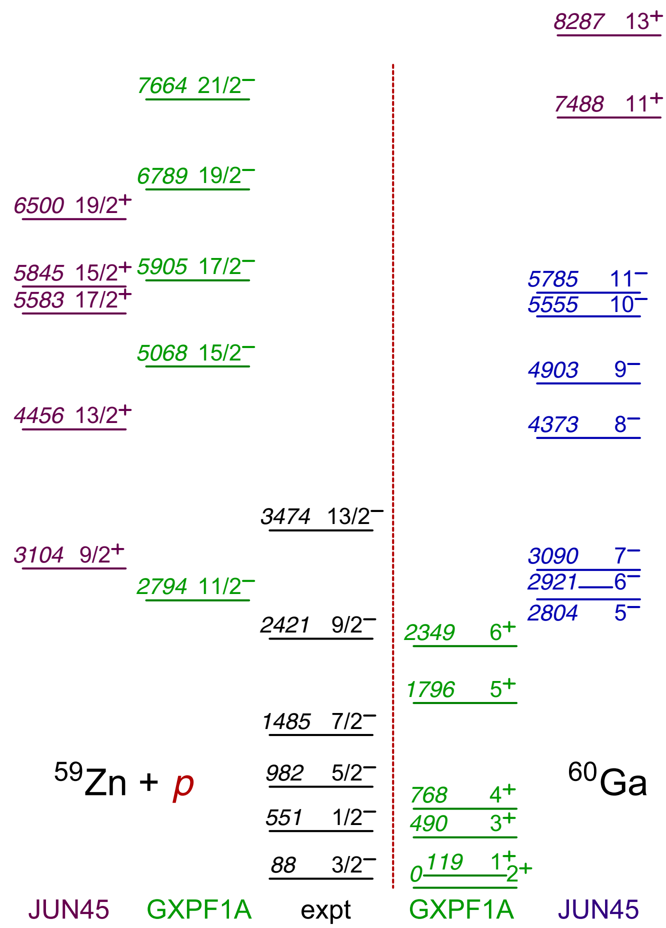

FIG. 13. Predicted level scheme of ^{60}Ga (right) and observed [59] and calculated levels of ^{59}Zn (left). Energies are normalized to the ground state of ^{60}Ga. Based on Ref. [58], $S_p(^{60}\text{Ga}) = 88$ keV is set. Shell-model interactions used are given underneath each column of states. The predicted level energies are based on experimentally known states in the mirror nuclei ^{60}Cu (cf. Table I) and ^{59}Cu [3] and added calculated mirror energy differences (cf. Fig. 12). See text for details.

ure 12, which complements Fig. 4 in Ref. [7], shows predicted MED for the mass $A = 59$, $T_z = \pm 1/2$, ^{59}Zn - ^{59}Cu mirror pair, and the mass $A = 60$, $T_z = \pm 1$, ^{60}Ga - ^{60}Cu mirror pair. Figure 13 shows the few experimentally known states in ^{59}Zn [59] together with predictions for the positive- and negative-parity yrast lines of ^{59}Zn and ^{60}Ga based on known states in the mirror nuclei in conjunction with calculated MED. Note that the states of the combined $A = 60$ system ^{59}Zn $+p$ are drawn relative to the ground state of ^{60}Ga to allow for an assessment of direct proton emission from excited states in ^{60}Ga into states of ^{59}Zn (see below).

Figure 12(a) includes the handful of known experimental $A = 59$ MED values. The agreement with the predictions of all three shell-model interactions (GXPF1A, KB3G56, JUN45) is remarkably good and comparable for these few experimentally known negative-parity states. This is in line with results for the $T_z \pm 1/2$, $A = 57$ and $A = 61$ mirror pairs discussed in Ref. [7]. For the $A = 59$ positive-parity states, predictions are displayed in Fig. 12(b). These states can only be handled by the JUN45 interaction in the $f_{5/2}pg_{9/2}$ space. The alternating pattern of rather large MED values can be traced primarily to rather variant neutron vs proton $g_{9/2}$ excitations for signature $\alpha = +1/2$ and $\alpha = -1/2$ states, respectively.

The picture becomes more complicated for the predicted low-lying positive-parity states of the $A = 60$ mirror pair. Their MED are displayed in Fig. 12(c). While for all three interactions MED ≈ 0 keV for the 2^+ and 3^+ states, JUN45 predicts a somewhat larger MED for the 1^+ state. More drastically, the predictions of KB3G56 deviate significantly from those of the other two interactions for the 4^+, 5^+, and 6^+ states. First, this observation can be linked to the very different predictions for branching ratios of these states (cf. Table II and Sec. V A 2). Second, a closer look at predicted occupation numbers reveals that the MED variations primarily arise from different proton and neutron occupations of particles in the $p_{3/2}$ ($j = \ell + 1/2$) and $f_{5/2}$ ($j = \ell - 1/2$) orbitals, which can lead to largely different contributions of the $V_{\ell s}$ term to the predicted MED values. Measuring excited states in ^{60}Ga would obviously help constrain interaction matrix elements in the upper fp shell.

The predicted MED for negative-parity states in the $A = 60$ mirror pair are shown in Fig. 12(d). They are negative and similarly large as for the positive-parity states in the mass $A = 61$, $T_z \pm 1/2$ pair ^{61}Ga - ^{61}Zn [7]. The main driver is the $V_{\ell s}$ contribution because of a switch from $\nu(g_{9/2})$ partitions in states of ^{60}Cu and ^{61}Zn to $\pi(g_{9/2})$ partitions in states of ^{60,61}Ga. In support of this interpretation, calculated occupation numbers are close to 1.0 for the respective particle in the $g_{9/2}$ orbital for the 5^-, 6^-, 7^-, 8^-, 10^-, and 11^- states.

The reduction in absolute size of MED for the 8^- and 10^- states relates primarily to changes in occupation numbers of particles in the $p_{3/2}$ and $f_{5/2}$ orbitals. The situation is more complex in the case of the two close-lying 9^- states, in experiment for ^{60}Cu and in theory for both $A = 60$ isotopes under investigation. Wave-function partitions and occupation numbers show that the calculated yrast 9^-_1 state in ^{60}Cu should, in principle, be associated with the calculated yrare 9^-_2 state in ^{60}Ga and vice versa. In that case, $\mathrm{MED}(9^-_1) = E_x(9^-_1, \mathrm{Ga}) - E_x(9^-_2, \mathrm{Cu}) = -335$ keV, rather than $\mathrm{MED}(9^-_1) = E_x(9^-_1, \mathrm{Ga}) - E_x(9^-_1, \mathrm{Cu}) = -72$ keV used for Figs. 12 and 13. In this reversed scheme for ^{60}Ga, which is based on the observed yrast and yrare 9^- states in ^{60}Cu, the predicted energies for ^{60}Ga would be $E_x(9^-_1) = 4661$ keV and $E_x(9^-_2) = 5116$ keV.

Another note concerns the reported 837-keV γ ray from the β^+-decay study of ^{60}Ge, which has been associated with an excited 1^+ state in ^{60}Ga [54]. For the JUN45 interaction, summing the very large $\mathrm{MED}(1^+_2) = +474$ keV to the known $E_x(1^+_2) = 365$ keV of ^{60}Cu [20] leads to a predicted $E_x(1^+_2) =$ 839 keV for the yrare 1^+_2 state in ^{60}Ga, which is in perfect agreement with the measured γ-ray energy. However, it is difficult to identify one specific source that explains the exceptionally large predicted MED for the yrare 1^+_2 states. First, the wave functions of the involved states are reasonably symmetric in occupation numbers, and even though wave-function partitions hardly exceed 10%, it is apparent that the yrast 1^+_1 states in both $A = 60$ isotopes are part of the $\pi(p_{3/2}) \times \nu(p_{3/2})$ multiplet, while the yrare 1^+_2 states have more a $\pi(p_{1/2}) \times \nu(p_{1/2})$ character. The predicted branching ratio of a 837-keV γ-ray into the 2^+ ground state of ^{60}Ga is 94%. The derived lifetime of $\tau(1^+_2) \approx 50$ fs is very short, because of a large $B(M1, 1^+_2 \to 2^+_1) = 1.8\mu_N^2$ strength. The large electromagnetic decay strength also outweighs potential $\ell = 1$ proton emission into the ground state of ^{59}Zn (see below).

Tunneling estimates based on the semiclassical Wenzel-Kramers-Brillouin (WKB) approach indicate proton-emission times of around 1 ps for $Q_p \approx 0.7$, 1.0, and 1.2 MeV for protons of $\ell = 1$, $\ell = 3$, and $\ell = 4$, respectively, between the states of ^{60}Ga and ^{59}Zn. Because the experimental $A = 59$ MED are well described [see Fig. 12(a)] and low-lying positive-parity states assessed with $t = 6$ GXPF1A calculations are found to describe the states in ^{60}Cu best (cf. Sec. V A 2), spectroscopic factors between low-lying positive-parity states in ^{60}Ga and low-lying negative-parity states in ^{59}Zn are investigated with that shell-model interaction.

The yrast 3^+ state in ^{60}Ga is predicted at $E_x \approx 0.5$ MeV (cf. Fig. 13). This implies $Q_p \approx 0.4$ MeV and consequently that this state decays by electromagnetic radiation into lower lying 1^+ and 2^+ states, similar to its mirror nucleus ^{60}Cu. With $Q_p \approx 0.7$ MeV and a calculated spectroscopic factor $C^2S \approx$ 0.6, the yrast 4^+ state in ^{60}Ga might be subject to $\ell = 3$, $f_{5/2}$ proton emission into the $3/2^-$ ground state of ^{59}Zn, in competition with electromagnetic decay to lower-lying states in ^{60}Ga. Admittedly, for $Q_p = 0.7$ MeV $T_{1/2,p(\ell=3)} \approx 200$ ps. However, the electromagnetic decay from the 4^+_1 state is also hindered ($T_{1/2,\gamma} \approx 100$ ps), which can also be inferred from the predicted lifetime of its 557-keV 4^+_1 mirror state in ^{60}Cu (cf. Table II).

The energetic and spectroscopic situation is at first sight comparable for the yrast 5^+ state in ^{60}Ga with $Q_p \approx 0.8$ MeV and $C^2S \approx 0.4$ for $f_{5/2}$ proton emission into the $5/2^-$ state of ^{59}Zn. Here, however, larger electromagnetic decay probabilities favor γ-ray emission—unless in turn $Q_p \approx 1.7$ MeV and, thus, $T_{1/2,p(\ell=3)} \approx 1$ fs compensates for $C^2S \approx 10^{-3}$ $f_{7/2}$ overlap with the $3/2^-$ ground state of ^{59}Zn. The same applies to the yrast 6^+ state in ^{60}Ga: Whether proton or γ-ray emission dominates will heavily depend on exact energies and overlap of the relevant parts of the wave functions of the states involved.

Potential proton emission from the negative-parity yrast states shown in Fig. 13 need to be addressed by calculations based on the JUN45 interaction. Spectroscopic factors between states in reach by $\pi(g_{9/2})$ emission are always large ($C^2S > 0.5$) and $Q_p > 2$ MeV for all these possible decay branches. Thus, $\ell = 4$, $g_{9/2}$ proton emission is expected to outplay electromagnetic decay by orders of magnitude for all these states [5,7,8,10,13].

For the predicted 11^+ and 13^+ states of ^{60}Ga, $\ell = 4$, $g_{9/2}$ proton emission is even more in favor. Although the calculated spectroscopic factors are reduced by about a factor of 2 compared with those predicted for the negative-parity yrast states, Q_p values are larger and γ-ray emission is hindered (cf. Table III). In addition, also $Q_p \approx 1.6$ MeV, $\ell = 3$ $f_{5/2}$ decay branches become possible, allowing for an $11^+ \to 17/2^-$ proton transition.

B. Cranked Nilsson-Strutinsky calculations

The rotational bands in ^{60}Cu have been analyzed in the configuration-constrained Cranked Nilsson-Strutinsky (CNS) formalism [60–62]. The configurations are described from the filling of the orbitals (the eigenstates) in a deformed rotating modified oscillator potential. It is important to consider configurations that vary smoothly as functions of deformation and rotational frequency. This is achieved by constructing diabatic orbitals, where so-called virtual crossings between orbitals are replaced by real crossings. A special feature is that the diagonalization of the Hamiltonian is carried out in the basis states of the rotating Harmonic-Oscillator potential, where the principal quantum number $\mathcal{N}_{\mathrm{rot}} = \mathcal{N}$ is treated as pure. This is a minor approximation, which makes it straightforward to put unique labels on the orbitals and thus on the different configurations.

The CNS formalism has been very successful in the description of medium- and high-spin states in different regions of nuclei; for example, in the present $A \approx 60$ region (see, e.g., Refs. [10,17,63]), the $A \approx 110$ region [61,64,65], and the $A \approx 160$ region [66–69]. Indeed, in that region, the model has been used in the full spin range. Furthermore, recent applications [69–71] suggest that the model could be useful for the understanding of the full spin range also in other regions of the chart of nuclei.

The single-particle parameters κ and μ determine the strengths of the $\ell \cdot s$ and the ℓ^2 terms and thus the position of the j shells in the modified oscillator potential. In the $A \approx 60$ region, so-called "standard parameters" [60] have generally been used. However, in Ref. [63] an attempt was made to

TABLE V. Proton (vertical), neutron (horizontal), and combined configurations which are selected in the yrast region up to spin $I = 24$ for ^{60}Cu. For the proton and neutron configurations, the maximum spin, $I_{\max}$, for the different signatures is specified. The shorthand configuration labels and the $I_{\max}$ values are specified for the combined configurations. Furthermore, it is specified which observed band is assigned to the different configurations. For new parameters, the energy of these configurations is drawn relative to the rotating liquid drop energy in Fig. 14.

		Neutrons					
		$(fp)^3$ 4.5$\hbar$, 5.5$\hbar$	$(fp)^2 g^1_{9/2}$ 8.5$\hbar$	$f^{-1}_{7/2}(fp)^3 g^1_{9/2}$ 11.5$\hbar$–13.5$\hbar$	$f^{-1}_{7/2}(fp)^2 g^2_{9/2}$ 14.5$\hbar$, 15.5$\hbar$	$f^{-2}_{7/2}(fp)^3 g^2_{9/2}$ 18.5$\hbar$, 19.5$\hbar$	$f^{-2}_{7/2}(fp)^2 g^3_{9/2}$ 20.5$\hbar$
Protons	$(fp)^1$ 1.5$\hbar$, 2.5$\hbar$	[10;30] 6$\hbar$–8$\hbar$ ND1	[10;21] 10$\hbar$, 11$\hbar$ ND2				
	$g^1_{9/2}$ 4.5$\hbar$		[01;21] 13$\hbar$ ND3				
	$f^{-1}_{7/2}(fp)^2$ 6.5$\hbar$, 7.5$\hbar$	[(1)20;30] 11$\hbar$-13$\hbar$ D1	[(1)20;21] 15$\hbar$, 16$\hbar$ D2	[(1)20;(1)31] 18$\hbar$–21$\hbar$ Q1			
	$f^{-1}_{7/2}(fp)^1 g^1_{9/2}$ 8.5$\hbar$–10.5$\hbar$		[(1)11;21] 17$\hbar$–19$\hbar$ D3				
	$f^{-2}_{7/2}(fp)^2 g^1_{9/2}$ 14.5$\hbar$		[(2)21;21] 23$\hbar$ Q2	[(2)21;(1)31] 26$\hbar$–28$\hbar$	[(2)21;(1)22] 29$\hbar$, 30$\hbar$ Q4	[(2)21;(2)32] 33$\hbar$, 34$\hbar$ Q3	[(2)21;(2)23] 35$\hbar$
	$f^{-2}_{7/2}(fp)^1 g^2_{9/2}$ 15.5$\hbar$, 16.5$\hbar$				[(2)12;(1)22] 30$\hbar$–32$\hbar$		

find improved parameters specifically designed for this mass region. These parameters are referred to as "new parameters." A specific feature of these new parameters is that the neutron $g_{9/2}$ shell comes at a lower energy than the proton $g_{9/2}$ shell. This is contrary to the general experience from heavier nuclei (see, e.g., Ref. [72]), which would imply that the Coulomb potential should push the proton high-j intruder shell, i.e., in $A \approx 60$ the $g_{9/2}$ shell for $\mathcal{N} = 4$, below the corresponding neutron shell.

Different from the shell-model calculations discussed in Sec. V A, CNS calculations can handle all orbitals relevant for $A \approx 60$ nuclei; namely, those in the full $\mathcal{N} = 3$ fp shells plus the $\mathcal{N} = 4$ $g_{9/2}$ intruder orbitals. Note that these shells are not the pure j shells but instead the orbitals in a deformed rotating potential whose wave functions are dominated by specific j shells. The low-spin states of ^{60}Cu are built with all valence particles in the upper fp orbitals (cf. Sec. V A 2). At higher spin and excitation energy, states are formed by successive excitations from the $f_{7/2}$ orbitals and into the $g_{9/2}$ orbitals. The CNS configurations for protons and neutrons are each labeled as $(q_1)q_2q_3$, where q_1 is the number of $f_{7/2}$ holes. Note that q_1 will not be specified when equal to zero. Furthermore, q_2 and q_3 denote the number of particles in the upper fp and $g_{9/2}$ orbitals, respectively. For an odd number of particles in a group, the signature can be specified by a subscript $+$ ($\alpha = +1/2$) or a $-$ ($\alpha = -1/2$) sign. The full configuration is given within square brackets with proton and neutron configurations separated by a semicolon. It is also instructive to define the quantity $I_{\max}$, which is the highest spin that can be formed in a configuration if the j shells were pure.

In the present application to ^{60}Cu, calculations were performed with standard parameters as well as new parameters. First, the yrast configurations for the four different combinations of parity and signature were searched in the spin range $I = 0$–24. With minor differences, the same configurations were selected from the two parameter sets. Two configurations which appeared to be of no interest were, however, excluded: One with two neutrons of upper fp character with signature $\alpha = +1/2$ instead of $\alpha = -1/2$, and another with four neutrons of upper fp character and no $g_{9/2}$ neutron. Instead, the $[(1)20;(1)31]$ configuration was added because it turned out to be the only configuration which can explain the experimental Q1 band with a reasonable accuracy. The selected configurations were complemented by their $f_{7/2}$ and upper fp signature partners. For the orbitals at the bottom of the $g_{9/2}$ shell, on the other hand, only the signature $\alpha = +1/2$ was included. It is well known, and also calculated here, that this signature is strongly favored in energy. The resulting configurations are listed in Table V. For the calculation with new parameters, they are drawn relative to the rotating liquid drop energy in Fig. 14.

Comparing the agreement between calculations and experiment for standard parameters and new parameters, it was concluded that the best agreement is obtained for the calculations using the new parameters. Hence, the calculated configurations using new parameters are compared with the observed bands in Figs. 15 and 16 for the higher-spin and lower-spin bands, respectively. For the higher-spin bands in Fig. 15, it is in general obvious which band should be assigned to which configuration. This is seen from the shape of the E-E_{rld} curves, and in some cases also from the maximum spin observed. In fact, these bands are typically observed at exactly their expected $I_{\max}$ values. For example, the rather high energies for γ rays connecting the highest spin states of the D2a and D3b bands are well reproduced in the calculations. Notably, the effect is caused by the high energy cost to promote a proton from the low-lying $f_{7/2}$, $m = -7/2$ state at oblate shape. For the lower-spin bands presented in Fig. 16, given the complexity of the decay scheme, compromises had to be made to select experimental states based on both yrast

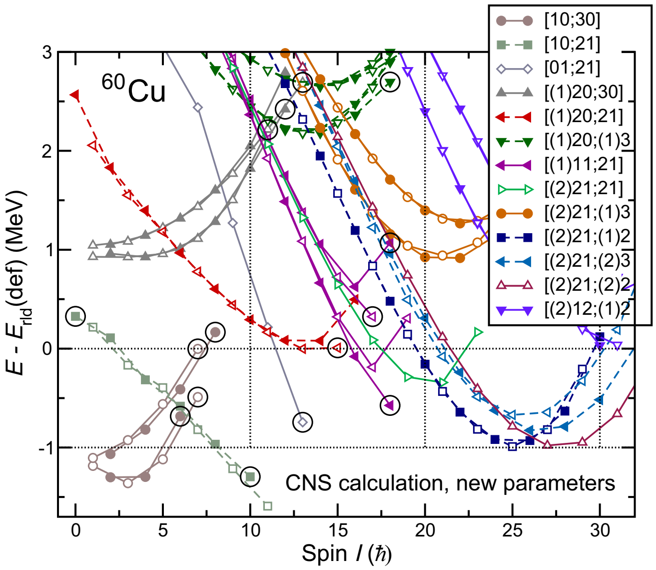

FIG. 14. The energy of the yrast configurations, which are specified in Table V, is plotted relative to the deformation-dependent rotating liquid drop reference, $E_{\mathrm{rld}}(\mathrm{def})$. The same color and symbol are used for configurations differing by signature but having the same distribution of particles over the j shells. Positive-parity states are connected by full lines and negative-parity states by dashed lines. Closed symbols are used for the signature $\alpha = +1/2$ and open symbols for $\alpha = -1/2$. Terminating states calculated as oblate at $\gamma = 60^{\circ}$ are encircled. Horizontal and vertical dotted lines (black) shall guide the eye.

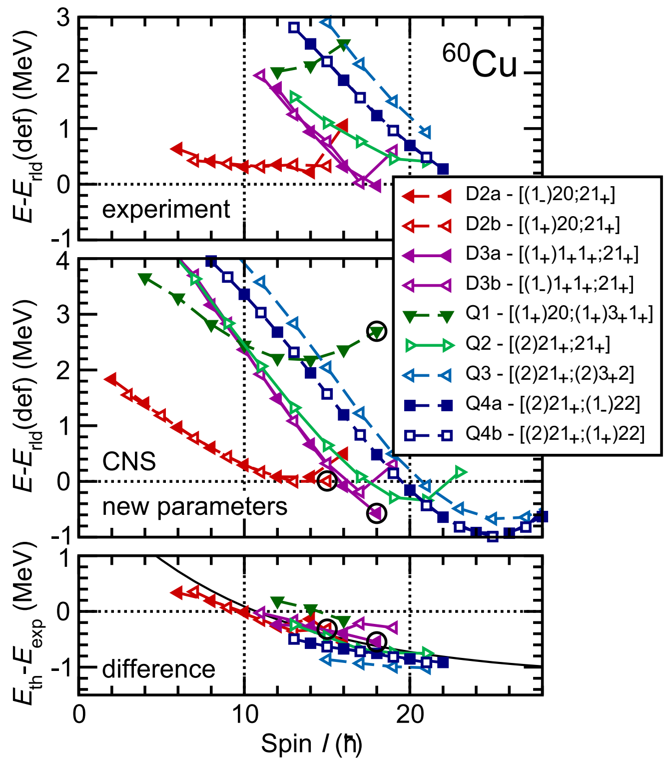

FIG. 15. The observed well-developed high-spin bands are drawn in the upper panel relative to the rotating liquid drop reference, with the calculated bands assigned to them drawn relative to the same reference in the middle panel. Experiment and calculations are compared in the lower panel, where the continuous line shows which spin dependence of the differences might be expected considering that pairing is not included in the calculations. New $A \approx 60$ CNS parameters were used [63]. For symbols and line explanations, see the caption of Fig. 14. The color code matches the one introduced in Sec. III.

character and regularity of structures (cf. indicative labels in Fig. 11). Here, states at 62, 0, 781, 1421, 1604, 2692, 3191, and 4074 keV are set to form the positive-parity structure ND1 in the spin range $I = 1$–8, while states at 2027, 2817, 3745, 4580, 5246, 6392, 7457, and 8920 are selected for structure D1 covering $I = 5$–12. Furthermore, states at 3156, 3772, 4521, 5188, 5649, and 6094 keV form the negative-parity structure ND2 ($I = 6$–11). For ND3, see Fig. 11.

It is experimentally uncertain if the lowest spin state of the Q1 band has $I_0 = 12$ or $I_0 = 13$. Considering only the observed states, the first guess would be $I_0 = 13$, because for $I_0 = 12$, the band will lie at a rather high excitation energy, and it might appear somewhat surprising that it is observed in the first place. However, comparing with calculations, there is no configuration which can naturally be assigned to the Q1 band with $I_0 = 13$. As seen in Fig. 15, the Q1 band is well described by the lowest calculated $[(1_+)20;(1_+)3_+1_+]$ configuration in the case of $I_0 = 12$. To further test the possibility that the bandhead spin of Q1 might be $I_0 = 13$, all proton and all neutron configurations in Table V were combined to see if there were any other reasonable assignments possible assuming $I_0 = 13$. Note that when considering the different signatures, there are 12 proton and 12 neutron configurations, i.e., 144 combined configurations possible. The result is that the best agreement is obtained for the lowest band of the other signature of the same $[(1)20;(1)31]$ configuration. However, noting that the differences in the lower panel of Fig. 15 follow the same trends for all bands assuming $I_0 = 12$, the trend for the Q1 band would deviate by about 1 MeV assuming $I_0 = 13$. The conclusion is that $I_0 = 12$ is by far the best theoretical proposal for the Q1 band. In fact, this assignment supports the experimental line of arguments in connection with the feeding pattern shown in Fig. 10.

In the lower panels of Figs. 15 and 16, the difference between experiment and calculations is compared with an exponential function, $f(I) = -1.2 + 3.5\exp(I/10)$ MeV, showing a suggested spin dependence of the difference, considering that pairing is neglected in the CNS calculations. It is gratifying that the values in Fig. 15 are well collected around this curve with discrepancies of only $\pm(0.3$–$0.4)$ MeV. The values for the lower spin bands in Fig. 16 are more scattered, with discrepancies of the order ± 1.0 MeV. However, when comparing experiment with calculations in Fig. 16, the shape of the different curves is well reproduced even for these low-spin states. This indicates that the cost within the bands to build higher spin states (the transition energies) is reproduced in the calculations.

In the calculations with standard parameters, the same conclusion is reached concerning the assignments for the different bands. However, for the high-spin bands, the differences

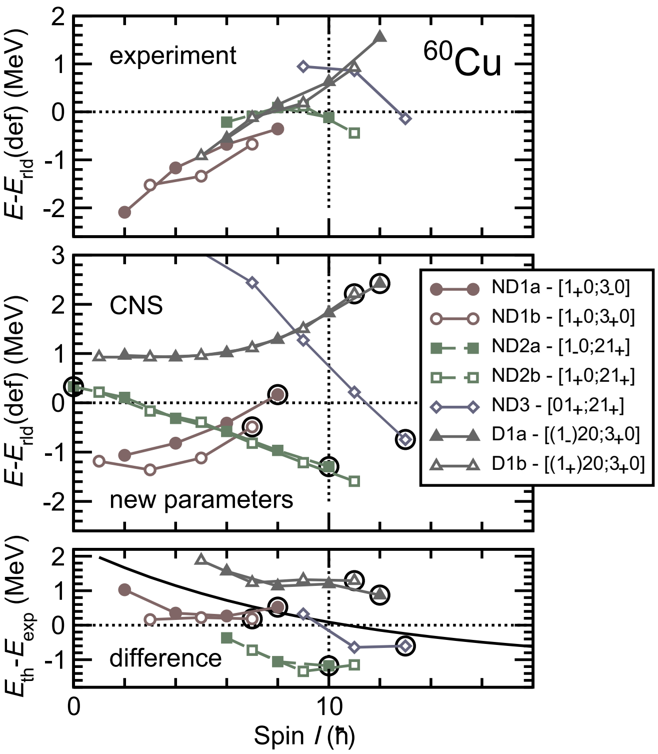

FIG. 16. Same as Fig. 15 but for the experimentally more irregular low-spin structures.

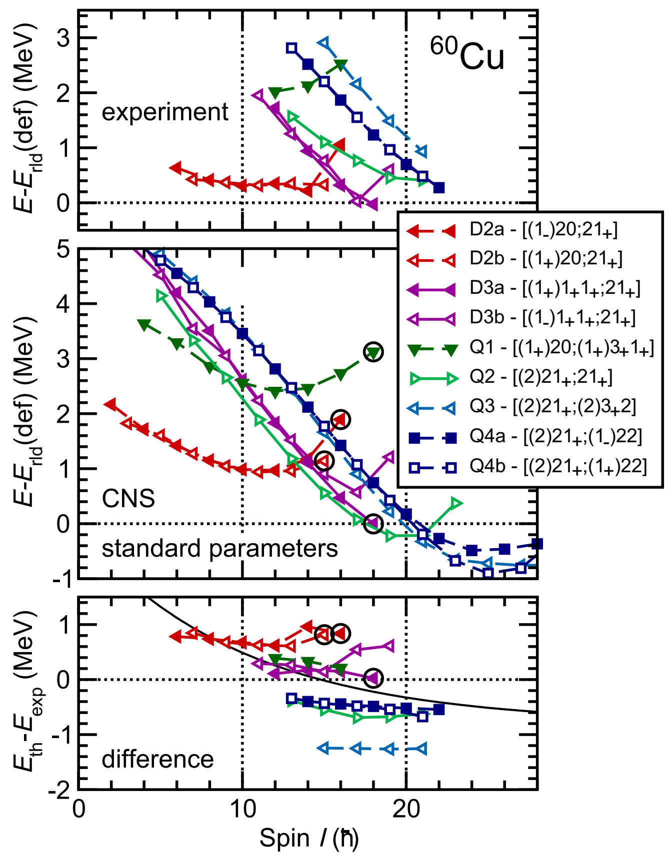

FIG. 17. Same as Fig. 15 but with calculations using standard parameters. The smooth curve suggesting the spin dependence of the average pairing energy is lifted by 0.4 MeV compared with the curve in Figs. 15 and 16.

between experiment and theory are clearly more scattered. This is illustrated in Fig. 17. The lower spin bands are described with a similar accuracy, independent of which parameters are chosen.

At very high spin, $I \gtrsim 22$, for the calculated [(2)21; (2)32] and [(2)21; (1)22] configurations, the E-$E_{\rm rld}$ curves in Fig. 17 show some irregular pattern for signature $\alpha = -1/2$. Considering the signature degeneracy in the observed Q4 band, it has to be assigned to a configuration with one hole in the $f_{7/2}$ orbitals for either protons or neutrons, i.e., a hole in the high-Ω [404]7/2 Nilsson orbital. This is known to lead to signature degeneracy for prolate and near-prolate shape. Therefore, the Q4 band is assigned to the [(2)21; (1)22] configuration with one neutron hole in the highest $f_{7/2}$ orbital. In the calculations with new parameters, Fig. 15, this signature degeneracy is seen for all spin values plotted in the figure, while it is not the case in the calculations with standard parameters in Fig. 17. The configuration assigned to the Q3 and Q4 bands differ by one neutron, which either occupies the highest $f_{7/2}$ orbital or the second lowest fp orbitals. Thus, the uneven feature of the curves with standard parameters points to a difficulty in distinguishing between these two orbitals. This is discussed in greater detail in Ref. [17].

In Refs. [3,17] it was shown that the general features of the rotational bands are mainly affected by the total number of $f_{7/2}$ holes and $g_{9/2}$ particles. Thus, it is relevant to classify the configurations assigned to the observed bands in ^{60}Cu according to these numbers. This is presented in Fig. 18. One can note that the ND2 structure, and even more the ND3 structure, have strongly down-sloping $E - E_{\rm rld}$ curves considering

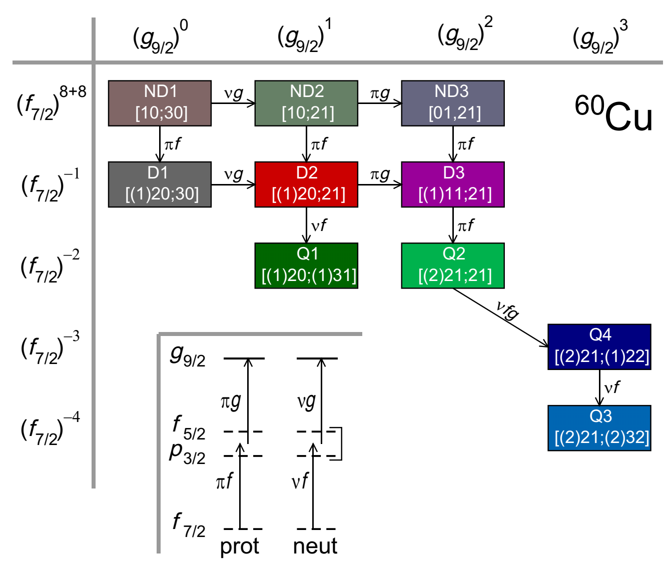

FIG. 18. The observed rotational bands in ^{60}Cu are classified according to the total number of $f_{7/2}$ holes (vertical direction) and $g_{9/2}$ particles (horizontal). Arrows indicate how the excitations defined in the inset lead to more and more excited configurations with a higher spin content.

that they have no $f_{7/2}$ holes but one or two $g_{9/2}$ particles, respectively. The curve for the D3a band is also down-sloping in its full spin range with only one $f_{7/2}$ hole and two $g_{9/2}$ particles. Other bands like D1, D2, Q1, and Q2, however, have relatively more $f_{7/2}$ holes leading to upsloping E-$E_{\rm rld}$ curves when approaching termination.

VI. SUMMARY

A comprehensive and significantly extended high-spin level scheme of ^{60}Cu has been derived with data stemming from three similar experiments, which all have exploited the Gammasphere γ-ray spectrometer coupled to ancillary detectors for measuring evaporated light particles. Reaction-channel selectivity as well as high statistics are the cornerstones of the experimental work. This allowed the derivation of a level scheme of ^{60}Cu comprising more than 300 γ-ray transitions connecting more than 100 excited states reaching spin $I = 22\hbar$ near 20 MeV excitation energy. Like neighboring nuclei, the structure evolves from irregular energy sequences via regular dipole bands into increasingly collective rotational bands featuring cascades of stretched $E2$ transitions.

These rotational bands have been interpreted with CNS calculations using standard single-particle parameters as well as a revised set of new parameters, which were specifically fitted to the $A = 60$ region [63]. The same configuration assignments result from either of the predictions, but the high-spin rotational bands are better described using the new parameters. Indeed, this description is exceptionally good, giving extra credibility to the work of Ref. [63].

The low-lying part of the level scheme of ^{60}Cu has been investigated with shell-model calculations using several model spaces and interactions commonly considered in the $A = 60$ region. The yrast and near yrast states are reasonably well explained, and the interpretation is in line with the classification of structures as suggested by the CNS model. In particular, the terminating 13^+ state of ND3, associated with the [01; 21] CNS configuration, finds its shell-model counterpart in a combination of fully aligned $[\pi(g_{9/2}) \times \nu(g_{9/2})]_9 \times \nu(fp)^2_4$ partitions, which are strongly favored energetically both in experiment and theoretical models. However, observed and predicted branching ratios do show occasional significant deviations between experiment and a given calculation, but also between calculations relying on different shell-model interactions. Additional observations of spectroscopic properties and lifetime measurements for "key" excited states may help to refine some shell-model parameters, including the two-body matrix elements of combinations of particles in the upper fp shell.

A case study of excited states in ^{60}Ga has been presented based on the decay scheme of its $T = 1$ mirror nucleus ^{60}Cu in combination with calculated mirror energy differences. Two major conclusions can be drawn from this exercise: First, all quasibound states beyond 2.5 MeV excitation energy in ^{60}Ga are likely to (almost) exclusively decay by $g_{9/2}$ proton emission into known or predicted states of negative or positive parity in the residual nucleus ^{59}Zn. For the 4^+, 5^+, and 6^+ yrast states, one can expect competition with electromagnetic decay. Only the 1^+ and 3^+ yrast and possibly the yrare 1^+_2 and 2^+_2 states appear robust against proton emission. Any experimental attempt to study low- to medium-spin states in ^{60}Ga must be sensitive to in-beam proton-γ coincidence relationships [7].

ACKNOWLEDGMENTS

The authors thank the staff members and accelerator crews at LBNL and ANL for the excellent support, and a number of former colleagues for assistance during the experiments. This research used resources of ANL's ATLAS facility, which is a DOE Office of Science User Facility. This research was funded in part by the Swedish Research Council (Vetenskapsrådet, VR 2022–3828), and supported by the U.S. Department of Energy, Office of Science, Office of Nuclear Physics under Contracts No. DE-AC02–06CH11357 (ANL) as well as No. DE-FG02–87ER-40316, No. DE-FG02–88ER-40406, and No. DE-SC0014442 (WU).

DATA AVAILABILITY

The data that support the findings of this article are not publicly available upon publication because it is not technically feasible and/or the cost of preparing, depositing, and hosting the data would be prohibitive within the terms of this research project. The data are available from the authors upon reasonable request.

[1] C. E. Svensson, C. Baktash, J. A. Cameron, M. Devlin, J. Eberth, S. Flibotte, D. S. Haslip, D. R. LaFosse, I. Y. Lee, A. O. Macchiavelli, R. W. MacLeod, J. M. Nieminen, S. D. Paul, L. L. Riedinger, D. Rudolph, D. G. Sarantites, H. G. Thomas, J. C. Waddington, W. Weintraub, J. N. Wilson, *et al.*, Observation and quadrupole-moment measurement of the first superdeformed band in the $A \sim 60$ mass region, Phys. Rev. Lett. **79**, 1233 (1997).

[2] C. E. Svensson, C. Baktash, G. C. Ball, J. A. Cameron, M. Devlin, J. Eberth, A. Galindo-Uribarri, S. Flibotte, D. S. Haslip, V. P. Janzen, D. R. LaFosse, I. Y. Lee, A. O. Macchiavelli, R. W. MacLeod, J. M. Nieminen, S. D. Paul, D. C. Radford, L. L. Riedinger, D. Rudolph, D. G. Sarantites, *et al.*, Smooth termination of rotational bands in ^{62}Zn: Evidence for a loss of collectivity, Phys. Rev. Lett. **80**, 2558 (1998).

[3] C. Andreoiu, D. Rudolph, I. Ragnarsson, C. Fahlander, R. A. E. Austin, M. P. Carpenter, R. M. Clark, J. Ekman, R. V. F. Janssens, T. L. Khoo, F. G. Kondev, T. Lauritsen, T. Rodinger, D. G. Sarantites, D. Seweryniak, T. Steinhardt, C. E. Svensson, O. Thelen, and J. C. Waddington, Evolution of shapes in ^{59}Cu, Eur. Phys. J. A **14**, 317 (2002).

[4] D. Rudolph, C. Baktash, M. J. Brinkman, E. Caurier, D. J. Dean, M. Devlin, J. Dobaczewski, P.-H. Heenen, H.-Q. Jin, D. R. LaFosse, W. Nazarewicz, F. Nowacki, A. Poves, L. L.

Riedinger, D. G. Sarantites, W. Satula, and C. H. Yu, Rotational bands in the doubly magic nucleus ^{56}Ni, Phys. Rev. Lett. **82**, 3763 (1999).

[5] D. Rudolph, C. Baktash, J. Dobaczewski, W. Nazarewicz, W. Satua, M. J. Brinkman, M. Devlin, H.-Q. Jin, D. R. LaFosse, L. L. Riedinger, D. G. Sarantites, and C.-H. Yu, Prompt proton decay of a well-deformed rotational band in ^{58}Cu, Phys. Rev. Lett. **80**, 3018 (1998).

[6] C. E. Svensson, D. Rudolph, C. Baktash, M. A. Bentley, J. A. Cameron, M. P. Carpenter, M. Devlin, J. Eberth, S. Flibotte, A. Galindo-Uribarri, G. Hackman, D. S. Haslip, R. V. F. Janssens, D. R. LaFosse, T. J. Lampman, T. Lauritsen, I. Y. Lee, F. Lerma, C. J. Lister, A. O. Macchiavelli, *et al.*, Decay out of the doubly magic superdeformed band in the $N = Z$ nucleus ^{60}Zn, Phys. Rev. Lett. **82**, 3400 (1999).

[7] Y. Hrabar, P. Golubev, D. Rudolph, L. G. Sarmiento, C. Müller-Gatermann, W. Reviol, D. Seweryniak, J. Wu, H. M. Albers, J. T. Anderson, M. A. Bentley, B. G. Carlsson, M. P. Carpenter, C. J. Chiara, P. A. Copp, D. M. Cox, J. Ekman, C. Fahlander, U. Forsberg, T. Huang, *et al.*, Identification of prompt proton emission in $N = Z - 1$ ^{61}Ga: Isospin symmetry at the limit of nuclear binding, Phys. Rev. Lett. **135**, 222503 (2025).

[8] E. K. Johansson, D. Rudolph, L.-L. Andersson, D. A. Torres, I. Ragnarsson, C. Andreoiu, C. Baktash, M. P. Carpenter, R. J. Charity, C. J. Chiara, J. Ekman, C. Fahlander, C. Hoel, O. L. Pechenaya, W. Reviol, R. du Rietz, D. G. Sarantites, D. Seweryniak, L. G. Sobotka, C. H. Yu, *et al.*, Prompt proton decay and deformed bands in ^{56}Ni, Phys. Rev. C **77**, 064316 (2008).

[9] D. Rudolph, I. Ragnarsson, W. Reviol, C. Andreoiu, M. A. Bentley, M. P. Carpenter, R. J. Charity, R. M. Clark, M. Cromaz, J. Ekman, C. Fahlander, P. Fallon, E. Ideguchi, A. O. Macchiavelli, M. N. Mineva, D. G. Sarantites, D. Seweryniak, and S. J. Williams, Rotational bands in the semi-magic nucleus $^{57}_{28}$Ni$_{29}$, J. Phys. G **37**, 075105 (2010).

[10] E. K. Johansson, D. Rudolph, I. Ragnarsson, L.-L. Andersson, D. A. Torres, C. Andreoiu, C. Baktash, M. P. Carpenter, R. J. Charity, C. J. Chiara, J. Ekman, C. Fahlander, O. L. Pechenaya, W. Reviol, R. du Rietz, D. G. Sarantites, D. Seweryniak, L. G. Sobotka, C. H. Yu, and S. Zhu, Thorough γ-ray and particle decay investigations of ^{58}Ni, Phys. Rev. C **80**, 014321 (2009).

[11] C.-H. Yu, C. Baktash, J. A. Cameron, M. Devlin, J. Eberth, A. Galindo-Uribarri, D. S. Haslip, D. R. LaFosse, T. J. Lampman, I.-Y. Lee, F. Lerma, A. O. Macchiavelli, S. D. Paul, D. C. Radford, I. Ragnarsson, D. Rudolph, D. G. Sarantites, C. E. Svensson, J. C. Waddington, J. C. Wells, *et al.*, Rotational bands with terminating properties in ^{59}Ni, Phys. Rev. C **65**, 061302(R) (2002).

[12] D. A. Torres, F. Cristancho, L.-L. Andersson, E. K. Johansson, D. Rudolph, C. Fahlander, J. Ekman, R. du Rietz, C. Andreoiu, M. P. Carpenter, D. Seweryniak, S. Zhu, R. J. Charity, C. J. Chiara, C. Hoel, O. L. Pechenaya, W. Reviol, D. G. Sarantites, L. G. Sobotka, C. Baktash, *et al.*, Deformations and magnetic rotations in the ^{60}Ni nucleus, Phys. Rev. C **78**, 054318 (2008).

[13] D. Rudolph, D. G. Sarantites, C. Andreoiu, C. Fahlander, D. P. Balamuth, R. J. Charity, M. Devlin, J. Eberth, A. Galindo-Uribarri, P. A. Hausladen, D. Seweryniak, L. G. Sobotka, and Th. Steinhardt, High-resolution in-beam particle spectroscopy–New results on prompt proton emission from ^{58}Cu, Eur. Phys. J. A **14**, 137 (2002).

[14] L.-L. Andersson, D. Rudolph, E. K. Johansson, D. A. Torres, B. G. Carlsson, I. Ragnarsson, C. Andreoiu, C. Baktash, M. P. Carpenter, R. J. Charity, C. J. Chiara, J. Ekman, C. Fahlander, C. Hoel, O. L. Pechenaya, W. Reviol, R. du Rietz, D. G. Sarantites, D. Seweryniak, L. G. Sobotka, *et al.*, Extensive γ-ray spectroscopy of normally and superdeformed structures in $^{61}_{29}$Cu$_{32}$, Eur. Phys. J. A **36**, 251 (2008).

[15] L.-L. Andersson, I. Ragnarsson, D. Rudolph, E. K. Johansson, D. A. Torres, C. Andreoiu, M. P. Carpenter, R. J. Charity, C. J. Chiara, J. Ekman, C. Fahlander, C. Hoel, O. L. Pechenaya, W. Reviol, R. du Rietz, D. G. Sarantites, D. Seweryniak, L. G. Sobotka, and S. Zhu, Comprehensive γ-ray spectroscopy of rotational bands in the $N = Z + 1$ nucleus ^{61}Zn, Phys. Rev. C **79**, 024312 (2009).

[16] J. Gellanki, I. Ragnarsson, D. Rudolph, C. E. Svensson, L.-L. Andersson, C. Andreoiu, C. Baktash, M. P. Carpenter, R. J. Charity, C. J. Chiara, J. Eberth, J. Ekman, C. Fahlander, D. S. Haslip, E. K. Johansson, D. R. LaFosse, S. D. Paul, O. L. Pechenaya, W. Reviol, R. du Rietz, *et al.*, Characterization of superdeformed bands in ^{62}Zn, Phys. Rev. C **80**, 051304(R) (2009).

[17] J. Gellanki, D. Rudolph, I. Ragnarsson, L.-L. Andersson, C. Andreoiu, M. P. Carpenter, J. Ekman, C. Fahlander, E. K. Johansson, W. Reviol, D. G. Sarantites, D. Seweryniak, C. E. Svensson, and J. C. Waddington, Extensive γ-ray spectroscopy of band structures in $^{62}_{30}$Zn$_{32}$, Phys. Rev. C **86**, 034304 (2012).

[18] D. Rudolph, I. Ragnarsson, S. Åberg, C. Andreoiu, M. P. Carpenter, R. M. Clark, J. Ekman, C. Fahlander, R. V. F. Janssens, F. G. Kondev, T. Lauritsen, D. G. Sarantites, D. Seweryniak, and C. E. Svensson, Onset of high-spin rotational bands in the $N = Z$ nucleus ^{62}Ga, Phys. Rev. C **102**, 014313 (2020).

[19] D. Rudolph, I. Ragnarsson, R. M. Clark, C. Andreoiu, M. P. Carpenter, J. Ekman, C. Fahlander, F. G. Kondev, T. Lauritsen, D. G. Sarantites, D. Seweryniak, and C. E. Svensson, Low-, medium-, and high-spin states in the $N = Z + 1$ nucleus ^{63}Ga, Phys. Rev. C **103**, 034306 (2021).

[20] E. Browne and J. K. Tuli, Nuclear data sheets for $A = 60$, Nucl. Data Sheets **114**, 1849 (2013).

[21] O. Izotova, D. Rudolph, J. Ekman, C. Fahlander, A. Algora, C. Andreoiu, R. Cardona, C. Chandler, G. de Angelis, E. Farnea, A. Gadea, J. Garcés Narro, J. Nyberg, M. Palacz, Zs. Podolyák, T. Steinhardt, and O. Thelen, Survey of $E1$ transitions in the mass $A \sim 60$ region, Phys. Rev. C **69**, 037303 (2004).

[22] S. Pigliapoco, M. L. Cortés, F. Recchia, P. Doornenbal, S. M. Lenzi, M. A. Bentley, F. Browne, L. S. Ferreira, A. Jungclaus, T. Koiwai, E. Maglione, D. Rudolph, R. Taniuchi, J. A. Tostevin, V. Vaquero, K. Wimmer, L. Zago, P. Aguilera, T. Arici, S. Carollo, *et al.*, Isospin symmetry holds beyond the proton drip line: First observation of excited states in ^{55}Cu, Phys. Lett. B. **878**, 140564 (2026)

[23] A. Fernández, A. Jungclaus, P. Doornenbal, M. A. Bentley, S. M. Lenzi, D. Rudolph, F. Browne, M. L. Cortés, T. Koiwai, R. Taniuchi, V. Vaquero, K. Wimmer, T. Arici, N. Imai, N. Kitamura, B. Longfellow, R. Lozeva, B. Mauss, D. R. Napoli, M. Niikura, *et al.*, Mirror energy differences above the $0f_{7/2}$ shell: First γ -ray spectroscopy of the $T_z = -2$ nucleus ^{56}Zn, Phys. Lett. B **823**, 136784 (2021).

[24] K. Wimmer, P. Ruotsalainen, S. M. Lenzi, A. Poves, T. Hüyük, F. Browne, P. Doornenbal, T. Koiwai, T. Arici, K. Auranen, M. A. Bentley, M. L. Cortés, C. Delafosse, T. Eronen, Z. Ge,

T. Grahn, P. T. Greenlees, A. Illana, N. Imai, H. Joukainen, *et al.*, Isospin symmetry in the $T = 1, A = 62$ triplet, Phys. Lett. B **847**, 138249 (2023).

[25] A. Obertelli, T. Baugher, D. Bazin, S. Boissinot, J.-P. Delaroche, A. Dijon, F. Flavigny, A. Gade, M. Girod, T. Glasmacher, G. F. Grinyer, W. Korten, J. Ljungvall, S. McDaniel, A. Ratkiewicz, B. Sulignano, P. Van Isacker, and D. Weisshaar, First spectroscopy of ^{66}Se and ^{65}As: Investigating shape coexistence beyond the $N = Z$ line, Phys. Lett. B **701**, 417 (2011).

[26] L.-L. Andersson, A trilogy of mass $A = 61$: Superdeformed structures, exotic decay, and isospin symmetry, Ph.D. thesis, Lund University, 2008, https://portal.research.lu.se/sv/publications/a-trilogy-of-mass-a61-superdeformed-structures-exotic-decay-and-i.

[27] E. Johansson, Nuclear structure and exotic decays; doubly-magic ^{56}Ni and semi-magic ^{58}Ni, Ph.D. thesis, Lund University, 2009, https://portal.research.lu.se/sv/publications/nuclear-structure-and-exotic-decays-doubly-magic-56ni-and-semi-ma.

[28] I.-Y. Lee, The Gammasphere, Nucl. Phys. A **520**, c641 (1990).

[29] The fifteen-detector arrangement comprised five units with hexagonal shape and ten bullet-like ones; see, P. A. Hausladen, *et al.*, Bull. Am Phys. Soc. (1997); D. Rudolph *et al.*, High-spin shell-model states near ^{56}Ni, Eur. Phys. J. A **4**, 115 (1999) (specifically Sec. 2).

[30] D. G. Sarantites, W. Reviol, C. J. Chiara, R. J. Charity, L. G. Sobotka, M. Devlin, M. Furlotti, O. L. Pechenaya, J. Elson, P. Hausladen, S. Fischer, D. Balamuth, and R. M. Clark, "Neutron Shell": A high efficiency array of neutron detectors for γ-ray spectroscopic studies with Gammasphere, Nucl. Instrum. Methods Phys. Res., Sect. A **530**, 473 (2004).

[31] D. G. Sarantites, P.-F. Hua, M. Devlin, L. G. Sobotka, J. Elson, J. T. Hood, D. R. LaFosse, J. E. Sarantites, and M. R. Maier, "The Microball": Design, instrumentation and response characteristics of a 4π-multidetector exit channel-selection device for spectroscopic and reaction mechanism studies with Gammasphere, Nucl. Instrum. Methods Phys. Res., Sect. A **381**, 418 (1996).

[32] C. E. Svensson, J. A. Cameron, S. Flibotte, G. Gervais, D. S. Haslip, J. M. Nieminen, J. C. Waddington, J. N. Wilson, G. C. Ball, A. Galindo-Uribarri, V. P. Janzen, D. C. Radford, D. Ward, M. Cromaz, and T. E. Drake, Channel selection for high spin γ-ray spectroscopy studies via total energy measurements in fusion-evaporation reactions, Nucl. Instrum. Methods Phys. Res., Sect. A **396**, 228 (1997).

[33] P. Böhm, Y. Hrabar, D. Rudolph, P. Golubev, L. G. Sarmiento, H. M. Albers, J. T. Anderson, M. A. Bentley, M. P. Carpenter, C. J. Chiara, P. A. Copp, U. Forsberg, T. Huang, H. Jayatissa, T. Lauritsen, C. Müller-Gatermann, X. Pereira-Lopez, W. Reviol, D. Seweryniak, S. Stolze, *et al.*, Search for weak side branches in the electromagnetic decay paths of the 6526-keV 10^+ isomer in ^{54}Fe, Atoms **11**, 116 (2023).

[34] D. C. Radford, ESCL8R and LEVIT8R: Software for interactive graphical analysis of HPGe coincidence data sets, Nucl. Instrum. Methods Phys. Res., Sect. A **361**, 297 (1995).

[35] J. Theuerkauf, S. Esser, S. Krink, M. Luig, N. Nicolay, O. Stuch, and H. Wolters, program TV, University of Cologne (unpublished).

[36] E. Caurier, *Shell Model Code ANTOINE, IRES* (Strasbourg, 1989–2002).

[37] E. Caurier and F. Nowacki, Present status of shell model techniques, Acta Phys. Pol. B **30**, 705 (1999).

[38] M. Honma, T. Otsuka, B. A. Brown, and T. Mizusaki, Effective interaction for pf-shell nuclei, Phys. Rev. C **65**, 061301(R) (2002).

[39] A. Poves, J. Sánchez-Solano, E. Caurier, and F. Nowacki, Shell model study of the isobaric chains $A = 50$, $A = 51$ and $A = 52$, Nucl. Phys. A **694**, 157 (2001).

[40] E. Caurier, G. Martinez-Pinedo, F. Nowacki, A. Poves, and A. P. Zuker, The shell model as a unified view of nuclear structure, Rev. Mod. Phys. **77**, 427 (2005).

[41] D. Rudolph, B. Blank, J. Giovinazzo, T. Roger, H. Alvarez-Pol, A. Arokia Raj, P. Ascher, M. Caamaño-Fresco, L. Caceres, D. M. Cox, B. Fernández-Domínguez, J. Lois-Fuentes, M. Gerbaux, S. Grévy, G. F. Grinyer, O. Kamalou, B. Mauss, A. Mentana, J. Pancin, J. Pibernat, *et al.*, Mirror symmetry at mass $A = 54$: $E4$ effective charges near doubly magic ^{56}Ni, Phys. Lett. B **830**, 137144 (2022).

[42] D. Rudolph, C. Andreoiu, M. A. Bentley, M. P. Carpenter, R. J. Charity, R. M. Clark, J. Ekman, C. Fahlander, P. Fallon, W. Reviol, D. G. Sarantites, and D. Seweryniak, Experimental and shell-model study of excited states in $^{55}_{26}$Fe$_{29}$ and related notes on $^{55}_{29}$Cu$_{26}$, Phys. Rev. C **104**, 044314 (2021).

[43] J. Ekman, C. Fahlander, and D. Rudolph, Mirror symmetry in the upper fp shell, Mod. Phys. Lett. A **20**, 2977 (2005).

[44] A. P. Zuker, S. M. Lenzi, G. Martínez-Pinedo, and A. Poves, Isobaric multiplet yrast energies and isospin nonconserving forces, Phys. Rev. Lett. **89**, 142502 (2002).

[45] S. M. Lenzi, M. A. Bentley, R. Lau, and C. Aa Diget, Isospin-symmetry breaking corrections for the description of triplet energy differences, Phys. Rev. C **98**, 054322 (2018).

[46] M. Honma, T. Otsuka, T. Mizusaki, and M. Hjorth-Jensen, New effective interaction for f_5pg_9-shell nuclei, Phys. Rev. C **80**, 064323 (2009).

[47] R. du Rietz, J. Ekman, D. Rudolph, C. Fahlander, A. Dewald, O. Möller, B. Saha, M. Axiotis, M. A. Bentley, C. Chandler, G. de Angelis, F. Della Vedova, A. Gadea, G. Hammond, S. M. Lenzi, N. Mărginean, D. R. Napoli, M. Nespolo, C. Rusu, *et al.*, Effective charges in the fp shell, Phys. Rev. Lett. **93**, 222501 (2004).

[48] T. H. Ogunbeku, J. M. Allmond, T. J. Gray, W.-J. Ong, B. A. Brown, A. Gargano, R. Grzywacz, J. D. Holt, A. O. Macchiavelli, T. Miyagi, S. Neupane, B. C. Rasco, H. Schatz, B. M. Sherrill, O. B. Tarasov, H. Arora, A. D. Ayangeakaa, H. C. Berg, J. M. Berkman, D. L. Bleuel, *et al.*, Universal effective charges in the sd and fp shells, Phys. Rev. Lett. **135**, 072501 (2025).

[49] T. Otsuka, M. Honma, and T. Mizusaki, Structure of the $N = Z = 28$ closed shell studied by Monte Carlo shell model calculation, Phys. Rev. Lett. **81**, 1588 (1998).

[50] D. Rudolph, K. P. Lieb, and H. Grawe, Multiparticle-hole states of high spin in $N < 50$, $A \approx 90$ nuclei: 4. Systematics of level energies and electromagnetic properties, Nucl. Phys. A **597**, 298 (1996).

[51] D. Rudolph, I. Ragnarsson, C. Andreoiu, M. A. Bentley, M. P. Carpenter, R. J. Charity, R. M. Clark, J. Ekman, C. Fahlander, P. Fallon, W. Reviol, D. G. Sarantites, and D. Seweryniak, Single-particle and collective excitations in the $N = 28$ isotones ^{54}Fe and ^{53}Mn, Phys. Rev. C **102**, 014316 (2020).

[52] L. Kucuk, S. E. A. Orrigo, A. Montaner-Pizá, B. Rubio, Y. Fujita, W. Gelletly, B. Blank, Y. Oktem, T. Adachi, A. Algora,

P. Ascher, R. B. Cakirli, G. de France, H. Fujita, E. Ganioğlu, J. Giovinazzo, S. Grévy, F. M. Marqués, F. Molina, F. de Oliveira Santos, *et al.*, Half-life determination of $Tz = -1$ and $Tz = -\frac{1}{2}$ proton-rich nuclei and the β decay of ^{58}Zn, Eur. Phys. J. A **53**, 134 (2017).

[53] J. Giovinazzo, T. Goigoux, B. Blank, P. Ascher, M. Gerbaux, S. Grévy, T. Kurtukian-Nieto, C. Magron, P. Doornenbal, N. Fukuda, N. Inabe, G. G. Kiss, T. Kubo, S. Kubono, S. Nishimura, H. Sakurai, Y. Shimizu, C. Sidong, P.-A. Söderström, T. Sumikama, *et al.*, Acta Phys. Pol., B **51**, 577 (2020).

[54] S. E. A. Orrigo, B. Rubio, W. Gelletly, P. Aguilera, A. Algora, A. I. Morales, J. Agramunt, D. S. Ahn, P. Ascher, B. Blank, C. Borcea, A. Boso, R. B. Cakirli, J. Chiba, G. de Angelis, G. de France, F. Diel, P. Doornenbal, Y. Fujita, N. Fukuda, *et al.*, β decay of the very neutron-deficient ^{60}Ge and ^{62}Ge nuclei, Phys. Rev. C **103**, 014324 (2021).

[55] Meng Wang, W. J. Huang, F. G. Kondev, G. Audi, and S. Naimi, The AME 2020 atomic mass evaluation (II). Tables, graphs and references, Chin. Phys. C **45**, 030003 (2021).

[56] S. F. Paul, J. Bergmann, J. D. Cardona, K. A. Dietrich, E. Dunling, Z. Hockenbery, C. Hornung, C. Izzo, A. Jacobs, A. Javaji, B. Kootte, Y. Lan, E. Leistenschneider, E. M. Lykiardopoulou, I. Mukul, T. Murböck, W. S. Porter, R. Silwal, M. B. Smith, J. Ringuette, *et al.*, Mass measurements of $^{60\text{–}63}$Ga reduce x-ray burst model uncertainties and extend the evaluated $T = 1$ isobaric multiplet mass equation, Phys. Rev. C **104**, 065803 (2021).

[57] M. Wang, Y. H. Zhang, X. Zhou, X. H. Zhou, H. S. Xu, M. L. Liu, J. G. Li, Y. F. Niu, W. J. Huang, Q. Yuan, S. Zhang, F. R. Xu, Yu.A. Litvinov, K. Blaum, Z. Meisel, R. F. Casten, R. B. Cakirli, R. J. Chen, H. Y. Deng, C. Y. Fu, *et al.*, Mass measurement of upper fp-shell $N = Z - 2$ and $N = Z - 1$ nuclei and the importance of three-nucleon force along the $N = Z$ line, Phys. Rev. Lett. **130**, 192501 (2023).

[58] L. J. Sun, J. Dopfer, A. Adams, C. Wrede, A. Banerjee, B. A. Brown, J. Chen, E. A. M. Jensen, R. Mahajan, T. Rauscher, C. Sumithrarachchi, L. E. Weghorn, D. Weisshaar, and T. Wheeler, Extension of the particle x-ray coincidence technique: The lifetimes and branching ratios apparatus, Phys. Rev. C **111**, 055806 (2025).

[59] C. Andreoiu, M. Axiotis, G. de Angelis, J. Ekman, C. Fahlander, E. Farnea, A. Gadea, T. Kröll, S. M. Lenzi, N. Mărginean, T. Martinez, M. N. Mineva, C. Rossi Alvarez, D. Rudolph, and C. A. Ur, First identification of excited states in ^{59}Zn, Eur. Phys. J. A **15**, 459 (2002).

[60] T. Bengtsson and I. Ragnarsson, Rotational bands and particle-hole excitations at very high spin, Nucl. Phys. A **436**, 14 (1985).

[61] A. V. Afanasjev, D. B. Fossan, G. J. Lane, and I. Ragnarsson, Termination of rotational bands: Disappearance of quantum many-body collectivity, Phys. Rep. **322**, 1 (1999).

[62] B. G. Carlsson and I. Ragnarsson, Calculating the nuclear mass in the very high angular momentum regime, Phys. Rev. C **74**, 011302(R) (2006).

[63] J. Gellanki, B. G. Carlsson, I. Ragnarsson, and D. Rudolph, Comparative study of rotational bands in the $A \approx 60$ mass region: Modification of Nilsson parameters, Phys. Rev. C **89**, 024301 (2014).

[64] I. Ragnarsson, V. P. Janzen, D. B. Fossan, N. C. Schmeing, and R. Wadsworth, Smooth termination of collective rotational bands, Phys. Rev. Lett. **74**, 3935 (1995).

[65] K. Starosta, C. J. Chiara, D. B. Fossan, T. Koike, D. R. LaFosse, G. J. Lane, J. M. Sears, J. F. Smith, A. J. Boston, P. J. Nolan, E. S. Paul, A. T. Semple, M. Devlin, D. G. Sarantites, I. Y. Lee, A. O. Macchiavelli, and I. Ragnarsson, Smooth band termination at high spin in ^{113}I, Phys. Rev. C **64**, 014304 (2001).

[66] W. C. Ma, R. V. F. Janssens, T. L. Khoo, I. Ragnarsson, M. A. Riley, M. P. Carpenter, J. R. Terry, J. P. Zhang, I. Ahmad, P. Bhattacharyya, P. J. Daly, S. M. Fischer, J. H. Hamilton, T. Lauritsen, D. T. Nisius, A. V. Ramayya, R. K. Vadapalli, P. G. Varmette, J. W. Watson, C. T. Zhang, *et al.*, Competition between terminating and collective structures above spin $40\hbar$ in ^{154}Dy, Phys. Rev. C **65**, 034312 (2002).

[67] A. O. Evans, E. S. Paul, J. Simpson, M. A. Riley, D. E. Appelbe, D. B. Campbell, P. T. W. Choy, R. M. Clark, M. Cromaz, P. Fallon, A. Görgen, D. T. Joss, I. Y. Lee, A. O. Macchiavelli, P. J. Nolan, A. Pipidis, D. Ward, and I. Ragnarsson, High-spin structure in ^{157}Er up to and above band termination, Phys. Rev. C **73**, 064303 (2006).

[68] J. Simpson, M. A. Riley, A. Pipidis, E. S. Paul, X. Wang, P. J. Nolan, J. F. Sharpey-Schafer, A. Aguilar, D. E. Appelbe, A. D. Ayangeakaa, A. J. Boston, H. C. Boston, D. B. Campbell, M. P. Carpenter, C. J. Chiara, P. T. W. Choy, R. M. Clark, M. Cromaz, A. O. Evans, P. Fallon, *et al.*, Evolution of structure and shapes in ^{158}Er to ultrahigh spin, Phys. Rev. C **107**, 054305 (2023).

[69] I. Ragnarsson, A. Kardan, B. G. Carlsson, E. S. Paul, C. M. Petrache, M. A. Riley, J. F. Sharpey-Schafer, and J. Simpson, Band terminations and maximum spin values with up to 18 aligned particles (and holes) in the $Z, N = 50$ to 82 shells, Phys. Rev. C **110**, 034313 (2024).

[70] H.-L. Ma, B. G. Carlsson, I. Ragnarsson, and H. Ryde, Interpretation of the high spin states in ^{161}Lu: A paired and unpaired study, Phys. Rev. C **90**, 014316 (2014).

[71] A. Kardan, I. Ragnarsson, B. G. Carlsson, and H.-L. Ma, Interpretation of normal-deformed bands in ^{167}Lu, Phys. Rev. C **101**, 014323 (2020).

[72] S. G. Nilsson, C. F. Tsang, A. Sobiczewski, Z. Szymański, S. Wycech, C. Gustafsson, I.-L. Lamm, P. Möller, and B. Nilsson, On the nuclear structure and stability of heavy and superheavy elements, Nucl. Phys. A **131**, 1 (1969).